Aalto University
School of Engineering

Eetu Kivelä

The use of FSI models for the prediction of wind-induced vibration of modern cruise ship deck outfitting structures

Thesis submitted for examination for the degree of Master of Science in Technology

Espoo 03.06.2019
Supervisor: Professor Spyros Hirdaris
Advisors: M.Sc. (Tech.) Alexandra Tissari
M.Sc. (Tech.) Oliver Parmasto

Aalto-yliopisto
Insinööritieteiden korkeakoulu

Aalto-yliopisto, PL 11000, 00076 AALTO
www.aalto.fi

Diplomityön tiivistelmä

Tekijä Eetu Kivelä

Työn nimi FSI-mallien soveltaminen modernien risteilylaivojen kansivarusteluraken teiden tuuliherätteisen värähtelyn ennustamisessa

Maisteriohjelma Master's Programme in Mechanical Engineering **Koodi** ENG25

Työn valvoja Professori Spyros Hirdaris

Työn ohjaajat M.Sc. (Tech.) Alexandra Tissari, M.Sc. (Tech.) Oliver Parmasto

Päivämäärä 03.06.2019 **Sivumäärä** 73+1 **Kieli** englanti

Tiivistelmä

Viimeisimmät suuntaukset risteilymarkkinoilla pyrkivät tuomaan laivoille elämyksiä, jotka ovat aiemmin olleet mahdollisia vain maissa. Tämä on johtanut ennennäkemättömien rakenteiden, kuten vesipuistojen ja huvipuistolaitteiden integroimiseen modernien risteilyalusten yläkansille. Kyseiset rakenteet ovat ideaalisesti mahdollisimman kevyitä sekä koostuvat pitkistä ja suhteellisen ohuista palkeista, minkä tarkoituksena on vähentää ylimääräistä painoa laivan yläkansilla. Riskien minimoimiseksi on äärimmäisen tärkeää ymmärtää, miten jatkuva tuulikuormitus ja siitä johtuva pyörreherätteinen värähtely vaikuttavat rakenteiden dynaamiseen vasteeseen.

Tässä diplomityössä selvitetään, kuinka yhteen ja kahteen suuntaan kytketyt neste-rakenne -vuorovaikutusanalyysit eroavat laivan kansivarusteluraken teiden tuuliherätteisen värähtelyn ennustamisessa. Tätä varten suuri huvipuistorakenne on idealisoitu alumiinisena palkkikaarena, joka altistuu vakionopeuksiselle vastatuulelle. Rakenne analysoidaan aikariippuvaisilla yhteen ja kahteen suuntaan kytketyillä neste-rakenne -vuorovaikutussimulaatioilla. Virtausmallinnus perustuu Reynolds-keskiarvoistettuihin Navier-Stokes -yhtälöihin ja rakennemalli lineaariselastiseen 3D-elementtimenetelmään. Simulaatiot lasketaan käyttäen numeerista virtauslaskentaohjelmaa STAR-CCM+. Tuloksia arvioidaan ja verrataan kvasistaattisen ja kvasidynaamisen palkkielementtimallien kanssa. Palkkielementtimallit ratkaistaan käyttäen kaupallista NX Nastran -ratkaisijaa.

Diplomityön tulosten perusteella pyörteiden irtoaminen säilyy alkuperäisellä taajuudella laskettaessa yhteen suuntaan kytketyllä analyysilla. Kahteen suuntaan kytketty analyysi osoittaa, että pyörteiden irtoaminen lukkiutuu kaarirakenteen ominaistaajuudelle. Tämän johdosta rakenteen dynaaminen kuormitus kasvaa merkittävästi ja palkkikaari värähtelee resonanssissa. Yhteen suuntaan kytketty laskenta tai arvioidut yksinkertaisemmat menetelmät eivät kykene mallintamaan näitä ilmiöitä.

Avainsanat Neste-rakenne -vuorovaikutus, Pyörreherätteinen värähtely, FEA, CFD

Aalto University
School of Engineering

Aalto University, P.O. BOX 11000, 00076 AALTO
www.aalto.fi

Abstract of master's thesis

Author Eetu Kivelä

Title of thesis The use of FSI models for the prediction of wind-induced vibration of modern cruise ship deck outfitting structures

Master programme Master's Programme in Mechanical Engineering **Code** ENG25

Thesis supervisor Professor Spyros Hirdaris

Thesis advisors M.Sc. (Tech.) Alexandra Tissari, M.Sc. (Tech.) Oliver Parmasto

Date 03.06.2019 **Number of pages** 73+1 **Language** English

Abstract

Recent market trends in the cruise industry aim to provide traditionally land-based attractions on cruise liners. This leads to the integration of special architectural features, such as water parks and amusement rides, in way of the cruise ships' upper decks. Deck amusements are ideally lightweight structures that comprise of slender beams which aims to reduce the added weight on top decks. To ensure safety it is critical to understand the influence of wind loading introduced by Vortex-Induced Vibration (VIV) on the dynamic structural response.

This thesis aims to determine the differences between one- and two-way coupled Fluid-Structure Interaction (FSI) analyses in the context of ship deck outfitting structures subjected to VIV. Accordingly, a large deck amusement structure is idealized as an aluminum portal frame, subject to a constant head wind. Transient one- and two-way coupled FSI simulations, based on Reynolds-Averaged Navier-Stokes (RANS) fluid dynamics model and linear elastic 3D FEA, are conducted using the commercial CFD software STAR-CCM+. Results are assessed and compared against quasi-static and quasi-dynamic beam element idealizations solved by NX Nastran.

The investigation carried out reveals that vortex shedding remains at the original shedding frequency in the one-way coupled solution. However, the two-way coupled simulation demonstrates a clear lock-in of the vortex shedding to the portal frame's natural frequency. Consequently, the dynamic loading experienced by the portal frame is significantly increased and the structure experiences resonant vibration when full two-way FSI coupling is considered. Neither the one-way coupled nor the quasi-dynamic analysis are able to capture these effects.

Keywords Fluid-Structure Interaction, Vortex-Induced Vibration, FEA, CFD

Acknowledgements

I would like to thank my supervisor Professor Spyros Hirdaris for his guidance throughout the thesis process. His support starting with the initial steps of the topic definition is greatly appreciated. Additionally, I would like to thank Ph.D. P.A. Lakshmynarayanana for his comments and insight on the numerical methods.

I wish to thank my advisors M.Sc.(Tech) Alexandra Tissari and M.Sc.(Tech) Oliver Parmasto for their involvement in the thesis process. I value their professional opinion greatly.

I would like to express my gratitude to Foreship Ltd. for the financial support of this thesis. Completing the thesis would neither have been possible without the computational tools provided by the company. I also wish to thank my colleagues at Foreship Ltd. for their support. Special thanks to Tristan Connault for his linguistic assistance.

I should also extend my gratitude to LRK for introducing me to the wonderful world of Naval Architecture. The shipbuilding community in Aalto University is truly unique and they have provided me with countless fun and unforgettable experiences.

Finally, I want to thank my family for their continued support throughout my studies, especially my fiancée Miia for her love and encouragement.

Espoo, 03.06.2019

Eetu Kivelä

Table of Contents

Symbols

$\mathbf{B}$		strain-displacement matrix
$\mathbf{C}$	[kg/s]	damping matrix
$\mathbf{D}$		material property matrix
D	[m]	diameter
E	[GPa]	Young's modulus
F_i	[N]	force component
H	[m]	height of member
$\mathbf{K}$	[N/m]	stiffness matrix
L	[m]	length of member
$\mathbf{M}$	[kg]	mass matrix
Ma		Mach number
$\mathbf{M_f}$	[kg]	added mass
$\mathbf{N}$		shape function matrix
Re		Reynolds number
S_i	[m^2]	control volume surface area
St		Strouhal number
U	[m/s]	fluid free stream velocity
V_r		reduced velocity
b	[m]	width of member
$\mathbf{b}$	[N/m^3]	structural body force vector
c	[m/s]	speed of sound in a fluid
$\mathbf{f}$	[N]	external force vector
f_i	[Hz]	i^{th} eigenfrequency
f_s	[Hz]	vortex shedding frequency
$\mathbf{g}$	[m/s^2]	volume force vector, equal to gravitational acceleration 9.81 m/s^2
k	[m^2/s^2]	turbulent kinetic energy
m	[kg]	mass
m*		mass ratio
m_l	[kg/m]	mass per unit length
$\mathbf{n_i}$		surface normal
p	[Pa]	pressure
q_i		modal degree of freedom
r		residual
t	[s]	time
$\ddot{\mathbf{u}}$	[m/s^2]	acceleration vector
$\dot{\mathbf{u}}$	[m/s]	velocity vector
u	[m]	displacement
$\mathbf{u}$	[m]	displacement vector
$\mathbf{u_n}$	[m]	nodal displacement vector
v	[m/s]	fluid velocity
v^*	[m/s]	fluid reference velocity
$\mathbf{v_i}$	[m/s]	fluid velocity vector component
x_i	[m]	spatial coordinate
y	[m]	cell center wall normal distance
y^+		non-dimensional cell center wall distance

Δ		difference symbol
Γ	[m^2]	solid surface
Ω	[m^3]	finite control volume
α		mass-proportional Rayleigh damping coefficient
β		stiffness-proportional Rayleigh damping coefficient
δ		virtual differential
$\boldsymbol{\varepsilon}$		strain matrix
ε	[m^2/s^3]	turbulence dissipation rate
ζ_i		modal damping ratio
μ	[Pa·s]	fluid dynamic viscosity
μ_s		structural damping
ν	[m^2/s]	fluid kinematic viscosity
ν_p		Poisson ratio
ν_T	[m^2/s]	turbulent kinematic viscosity
ρ	[kg/m^3]	fluid density
ρ_s	[kg/m^3]	solid material density
$\boldsymbol{\sigma}$	[MPa]	stress tensor
σ_{vM}	[MPa]	von Mises stress
ω	[1/s]	specific turbulence dissipation rate
ω_i	[rad/s]	i^{th} natural frequency

Abbreviations

CF	Cross-Flow
CFD	Computational Fluid Dynamics
DNV GL	Classification Society
DOF	Degree Of Freedom
FEA	Finite Element Analysis
FEM	Finite Element Method
FSI	Fluid-Structure Interaction
FVM	Finite Volume Method
IL	In-Line
LES	Large Eddy Simulation
MUMPS	Multifrontal Massively Parallel Solver
N-S	Navier-Stokes equations
PSD	Power Spectral Density
RANS	Reynolds-Averaged Navier-Stokes equations
rms	root mean square
SIMPLE	Semi-Implicit Method for Pressure-Linked Equations
SST	Shear Stress Transport
VIV	Vortex-Induced Vibration

1 Introduction

Recent trends in the cruise market aim to provide typically land-based attractions on modern cruise liners. This leads to the integration of mega structures formerly seen only on land-based attractions, such as water parks and amusement rides, in way of the cruise ships' upper decks. These structures are carefully considered architectural features and the main attraction of the cruise ship.

Deck amusements are lightweight structures typically constructed of slender beams to reduce the added weight on the top deck level. This results in beam structures with a relatively low stiffness and possibly reduced fatigue life. The constant exposure to wind increases the dynamic response of these deck outfitting structures. This is due to the vortex-induced vibration (VIV) which is caused by the oscillating vortex shedding in the wake of the structure [1].

Due to the complexity and costly investment of the dedicated deck attractions, the risks involved in design are high. Conventional design approaches utilizing purely empirical formulas are not generally suitable for complex structures or may not even exist for the most novel solutions. Thus, exploring the potential of implementing the state of the art numerical methods, though time consuming and expensive, may be considered useful in the preliminary design stage.

The phenomenon where a fluid and a solid interact together is called fluid-structure interaction (FSI). Modern methods for analyzing FSI include the combination of state of the art numerical discretization techniques, such as, finite element analysis (FEA) and computational fluid dynamics (CFD). The current state of the art method used in naval architectural design is one-way coupled analysis where the loads are first obtained utilizing CFD. These are then applied on the structure separately using dynamic structural FEA. With the development of commercial analysis software and increase of computational processing capacity it has become possible to utilize two-way coupled analysis. In this approach, the two separate domains, i.e., fluid and solid, are solved simultaneously. It is believed that this numerical approach may be able to capture the influence of the dynamic response more accurately.

At first instance this thesis aims to gain thorough theoretical knowledge on dynamic response caused by VIV. This is achieved through a literary review. The knowledge is then applied to a case study where a large deck amusement structure is idealized as an aluminum portal frame. FSI is modelled by both one- and two-way coupled models. These are analyzed and compared against conservative modelling approaches utilizing quasi-static and quasi-dynamic modelling principles [2]. The main numerical methods applied in this thesis are linear elastic three-dimensional finite element method (FEM) and CFD based on Reynolds-averaged Navier-Stokes equations (RANS) utilizing finite volume method (FVM). Both FSI simulation study cases are solved using the commercial CFD software STAR-CCM+ and its integrated solvers. Additional analysis models are created using the commercial FEA program Femap and computed with the integrated finite element solver NX Nastran. The ultimate objective of the case study is to gain information on the modelling approaches for practical engineering work and to determine whether there are significant numerical differences.

The current study results are intended for theoretical purposes and may serve as early estimates for the suitability of the modelling approaches for practical engineering work. It is noted that due to the inherent complexity of fluid-structure interaction problems model testing remains the sole method for achieving validation data. In this sense the presented results should be validated by wind tunnel model tests.

2 Theoretical principles of vortex-induced vibration

2.1 Vortex-induced vibration

Structures that typically experience vortex shedding are bluff bodies such as bridges, marine cables and offshore risers [3], just to name a few. Vortex shedding is a phenomenon where an oscillating vortex street is formed behind a bluff structure [1]. A conceptual illustration of vortex shedding is presented in Figure 1. A numerical presentation of the phenomenon is shown in Figure 2. The interaction of an elastic structure with the oscillating vortex causes vortex-induced vibrations [1], which is defined as elastic structural motion due to the oscillating wake [4]. The main source of vibration is in the cross-flow (CF) direction, however in-line (IL) vibrations are also possible [5]. Vortex-induced vibrations are inherently a fluid-structure interaction problem as the fluid and solid domains interact dynamically with each other [6].

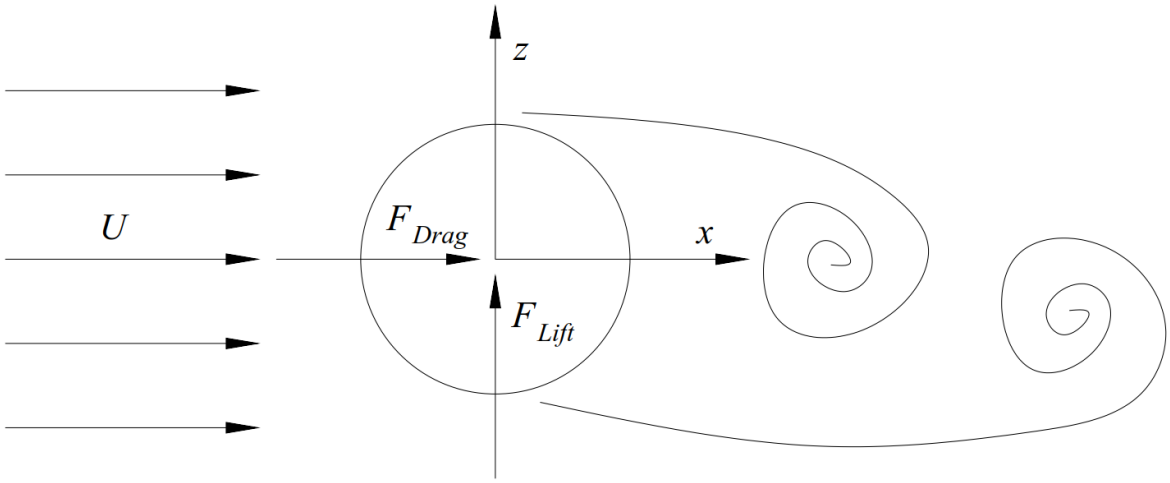

Figure 1.Conceptual presentation of vortex shedding and the genereted lift and drag forces behind a cylindrical cross-section.

The compressibility of a fluid is described by the Mach number. It is defined as the ratio of the fluid velocity, v, over the speed of sound, c, i.e., Ma = v/c. Considering the speeds at which cruise liners sail, the consideration may be limited to a Mach number range of Ma < 0.3. This is the region where fluid flow may be assumed incompressible [1].

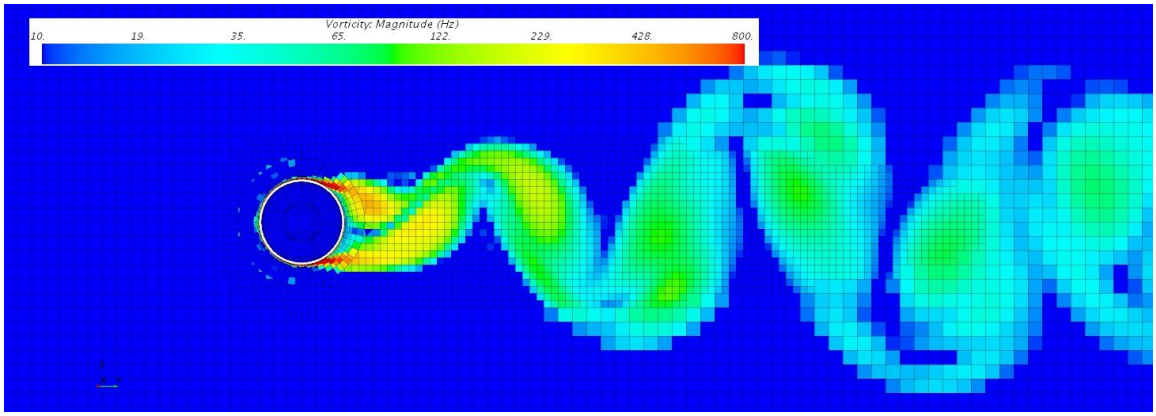

Figure 2. An example of numerically simulated vortex shedding behind a bluff structure.

Vortex shedding occurs as the incoming flow encounters the structure and the fluid pressure increases to the stagnation pressure at the leading edge of the structure where the flow velocity is zero. A boundary layer develops at the top and bottom sides of the structure. The flow is forced along the structure by the stagnation pressure. The boundary layers grow toward the end of the structure and finally separate behind it. [1] This creates two separate shear layers that trail in the wake of the structure as shown in Figure 2. Vortices are consequently generated as the boundary layer velocity near the structure is lower than near the free stream flow causing a velocity gradient in the flow [1]. This is due to the so called no-slip condition on the wall assuming that the relative flow velocity in way of the solid surface is zero [7]. The velocity gradient causes the characteristic rotating motion of the vortices.

The incoming fluid flow induces two transient force components, namely lift and drag, on the structure as shown in Figure 1. Lift force acts perpendicularly to the incoming flow, i.e., in the CF direction. Drag force acts in the IL direction of the flow. The force fluctuations occur at the vortex shedding frequency, f_s [1].

Vortex shedding behind a structure depends on a few fundamental non-dimensional parameters. The first is the Reynolds number, Re, which represents a measure of the fluid inertial forces over the viscous forces. Reynolds number describes the transition of the fluid flow from laminar to turbulent and is calculated as [1]:

$$\mathrm{Re} = \frac{UD}{\nu} \tag{1}$$

where U is the flow free stream velocity and ν is the fluid kinematic viscosity. D is the characteristic dimension which describes the structure's length dimension perpendicular to the flow direction.

Vortex shedding behind a structure is characterized by the Reynolds number range [1]. Reynolds number ranges and the associated vortex characteristics are presented for a smooth circular cross section in Table 1. The flow may also be described by the Reynolds number ranges as shown in Table 1.

Table 1. Vortex-shedding Reynolds number ranges for a smooth circular cylinder. Formed based on [8].

Reynolds number	Discription of vortex shedding
$\mathrm{Re} < 5$	Unseparated laminar flow
$5 \leq \mathrm{Re} < 40$	Separated flow, fixed pair of symmetric vortices
$40 \leq \mathrm{Re} < 150$	Laminar vortex street
$150 \leq \mathrm{Re} < 300$	Transition to turbulent vortices
$300 \leq \mathrm{Re} < 3\mathrm{x}10^5$	Fully turbulent vortex street
$3\mathrm{x}10^5 < \mathrm{Re} < 3.5\mathrm{x}10^6$	Turbulent boundary layer, narrow and disorganized wake
$3.5\mathrm{x}10^6 \leq \mathrm{Re}$	Turbulent vortex street re-established

Another important non-dimensional parameter that defines the vortex shedding frequency, f_s, is the Strouhal number, St, defined as [1]:

$$f_s = \frac{St\ U}{D} \tag{2}$$

Strouhal number for a circular cross-section is a function of Re. However, surface roughness and the incoming flow turbulence have an effect [1]. Strouhal numbers for various geometries are presented in literature, e.g., by Blevins [1] and DNV GL [4].

The recommended practice by DNV GL for vortex-induced oscillations [4] suggests that vibrations generally occur at a specific range of non-dimensional velocities termed as the reduced velocity V_r. Reduced velocity is calculated as [4]:

$$V_r = \frac{v}{f_i\ D} \tag{3}$$

where v is the instantaneous fluid velocity and f_i is i^{th} natural frequency of the structure. For wind exposed structures the relevant reduced velocity range for vortex-induced vibration is $4 < V_r < 8$ [4]. The velocity range depends on the mass ratio, m*. This is a measure of the structural mass compared to the buoyancy effect of the fluid calculated as [4]:

$$m^* = \frac{4m_l}{\pi\rho D^2} \tag{4}$$

where m_l is the mass of the structure per unit length and ρ is the fluid density.

Lock-in is a phenomenon inherently related to vortex shedding. If the vortex shedding frequency is close to the structure's eigenfrequency the two frequencies synchronize, i.e., the structural vibrations begin to control the vortex shedding frequency [1]. For flexible cylinders of multiple eigenmode response spectrum, a broad banded response is expected without clear lock-in [4].

2.2 Numerical consideration of VIV

In practical engineering vortex-induced vibrations are a relevant concern for multiple engineering structures and applications. In the field of civil engineering typical structures susceptible to VIV are bridges, towers and stacks [1]. In the marine field relevant structures are, e.g., offshore pipelines, cables and risers [9]. VIV may lead to structural failure via fatigue accumulation due to dynamic stress cycles [10]. Structural vibrations may also lead to excessive stresses that result in an ultimate limit state failure.

The importance of VIV in multiple engineering disciplines has led to an extensive spectrum of scientific literature on the subject. A detailed overview of VIV, in which the governing parameters of the phenomenon are thoroughly covered, is presented by Sarpkaya [9]. In the marine field, offshore applications are mostly present in scientific publications. Typical structures of interest are long cylindrical bodies submerged in water [9].

Previously, VIV has been exclusively analyzed with analytical methods based on experimental results. For this purpose, analytical formulae are presented, e.g., in [1, 2, 4].

These include the use of experimentally based lift and drag coefficients which relate the flow velocity, fluid properties and the structural geometry to the induced forces. The current state of the art, however, utilizes numerical modelling, almost exclusively.

Thorsen et al. [10, 11] and Ulveseter et al. [12] investigated vortex-induced vibration of a marine riser in multiple flow conditions. These studies were motivated by the inaccuracies present in the current industry standards for fatigue analysis of marine risers. Obtaining a more accurate model for the vortex-induced vibration leads subsequently to a more realistic fatigue estimate. These studies utilized semi-empirical VIV modelling approaches.

A civil engineering problem of wind-induced vibrations of heliostats used in a solar power plant was studied by Griffith et al. [13]. The expected structural eigenmodes and corresponding frequencies were first obtained through numerical finite element analysis. Subsequent experimental modal testing was conducted to obtain correlation data both for the wind exposed and near-stationary flow cases. It was found that the increase in wind speed leads to an increase in the aerodynamic damping. However, it is stated that despite the aerodynamic and structural damping the heliostat vibrations were characterized as lightly damped.

A typical VIV scenario in literature is a rigid, bluff body, e.g., cylinder which has only reduced number of degrees of freedoms (DOFs). In the simplest case, only the transverse degree of freedom is present. An article by Khan et al. [14] is a typical example of such a study. Reynolds-averaged Navier-Stokes modelling with SST k-ω turbulence model were applied to numerically study a rigid cylinder with only the transverse degree of freedom movement permitted. The cylinder was supported by an elastic spring-damper system. The computational domain in the study was essentially two-dimensional which represent a conventional approach for studying VIV utilizing coupled numerical analysis. Similarly, one DOF cylinders have been studied, e.g., in [3, 15]. RANS and turbulence modelling are discussed in more detail in Section 3.1.1.

A more complex problem setup was studied by Wang et al. [16]. An elliptical cylinder with both transverse and rotational degrees of freedoms was investigated in a 2D flow domain. It was found that for an aspect ratio of 1.0, i.e., circular cylinder, the rotational degree of freedom increases the transverse vibration amplitude compared to a one DOF system. However, the effect of the rotational DOF on the wake was limited. At higher aspect ratios the rotational DOF had significant effects on the response and the wake. This implies that the simplifications of the analyzed structure in terms of DOFs need to be well justified to retain physical accuracy.

A more sophisticated approach for analyzing VIV of long marine risers is presented in [17]. Three-dimensional finite element structural model with quadratic elements coupled with a large eddy simulation (LES) fluid model was used to evaluate the vibrational behavior in uniform and linear flow conditions. Fatigue accumulation due to VIV was again the motivation for an accurate modelling approach for marine risers. A response envelope comparison with the validation data is shown in Figure 3. The numerical results achieved in the study matched experimental results to an extent and the authors state that the used approach achieved reasonable accuracy. This highlights the complexity of VIV problems as even state of the art tools available in academia are unable to fully capture the physical behavior with complete accuracy.

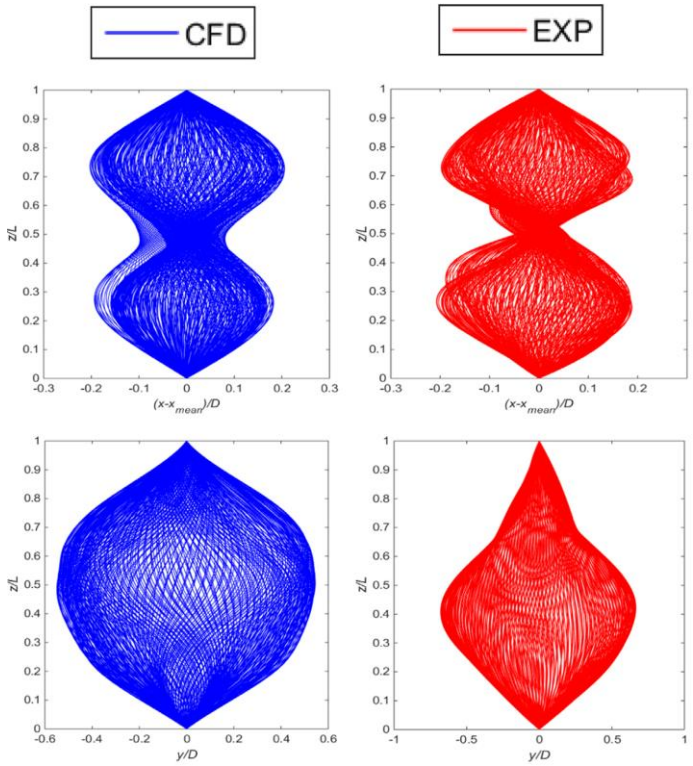

Figure 3. Structural response envelope comparison between numerical and experimental results [17].

The reasoning for studying vortex-induced vibrations in 3D is due to the complexity of the problem, as highlighted by the above studies. In a study by Zhao et al. [18], vortex-induced vibrations were studied for a rigid and elastically mounted cylinder in 3D and 2D. The authors found that the two-dimensional simulations either over- or underestimated the response amplitudes in the turbulent flow regime. This provides justification to apply numerical fluid dynamics in 3D in the present study. The three-dimensional vortices at a reduced velocity of $V_r = 4.0$ simulated in the study are shown in Figure 4. The intricacy of the wake field is evident even in the case of a simple cylinder geometry.

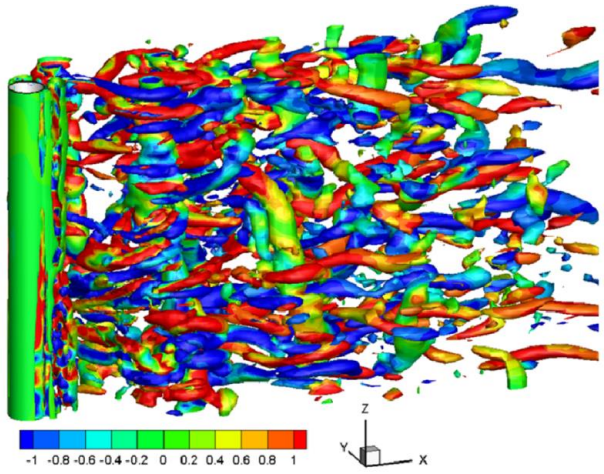

Figure 4. Vortices in a cylinder wake at V_r=4.0 and Re=1000 [18].

2.3 Vortex-induced FSI

Fluid-structure interaction is a phenomenon in which a solid and a fluid domain interact, i.e., the two domains are in a dynamic equilibrium state. The solid domain may experience rigid body motion, elastic or plastic deformations or both.

The scope of this section is specifically oriented towards vortex-induced FSI and how numerical methods have been applied for the analysis in both aerodynamic and hydrodynamic environments. For complex analyses where non-linearities are present, time domain simulations are typically applied [19]. In the present study, fluid-structure interaction is modelled directly in the time domain. Frequency domain analysis is only used in the pre-processing phase when aerodynamic effects are neglected.

Numerical methods for analyzing FSI can be divided into two main categories: partitioned and monolithic methods [20]. In a monolithic FSI simulation the equations that describe the fluid and structural physics are written into a single discrete equation system. The entire FSI problem is then solved as a single entity. [21] Partitioned methods, however, form separate equation systems for the fluid and the solid physics. These equation systems are solved by dedicated, separate solver algorithms. Data from fluid loads and structural displacements are transferred between the two domains via a coupling scheme. [20]

In this thesis, a partitioned approach to FSI is applied. Partitioned FSI analysis can be further divided into one- and two-way coupled analysis [20]. One-way coupling is the simpler analysis type in which the fluid domain is first computed. The transient pressure load and sometimes the frictional shear load to be used for the structural analysis are derived from the fluid solution. These are then used in a separate analysis step in which the structural response is calculated. Information flow in a one-way coupled analysis is only unidirectional, i.e., the fluid loads imposed on the structure cause a structural response which does not affect the fluid domain. A one-way coupled solution algorithm is presented in Figure 5.

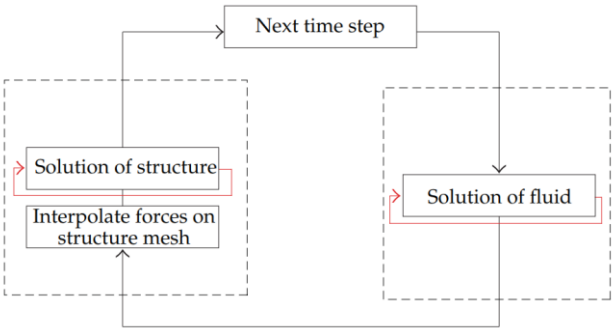

Figure 5. One-way coupled FSI algorithm [20].

Two-way coupled analysis represents a more sophisticated approach in which the information flows both ways. The structural deformations are transferred back into the fluid domain which adapts accordingly to the solid motions at certain accelerations and velocities. Two-way coupling is not a linear phenomenon because of the dynamic equilibrium that exists between the interacting solid and fluid domains in motion. Two different analysis strategies have been developed to deal with this coupling type, namely strong and weak coupling [20]. Strong coupling is an analysis method in which the fluid-solid equilibrium state is enforced to meet a given tolerance level within a numerical time step. In this method, the two solvers exchange information at each iteration step or at a specified number of

iterations [22]. The iterative loop within a time step continues until a convergence criterion is satisfied. An example of strong two-way coupling approach is presented in Figure 6.

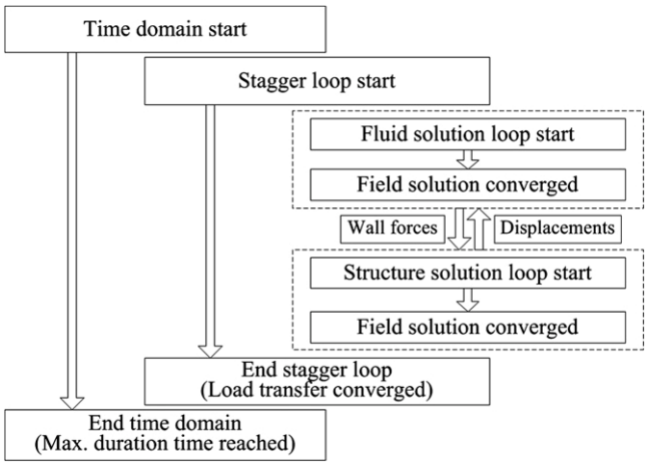

Figure 6. Strong, two-way coupled FSI solver algorithm [23].

Weakly coupled FSI simulations are less computationally intensive as the relevant information between the structural and fluid solvers are exchanged only once per time step. Fluid and solid domains are typically solved iteratively in succession. First, the fluid domain is solved, and the fluid loads are imposed on the solid domain. Second, the solid domain is solved separately. In the final stage, the solid displacements are transferred on the fluid domain which concludes the time step. Weak two-way FSI coupling has been utilized to study VIV of vertical risers, e.g., [17]. The coupling approach utilized in the article is illustrated in Figure 7. Weak coupling is mostly suitable for problems in which the structural domain has little effect on the fluid domain and is therefore closer to the one-way coupled FSI approach. Strong coupling implies that the solid domain has considerable effect on the fluid domain [20]. In such a case, a more computationally intensive approach is justified.

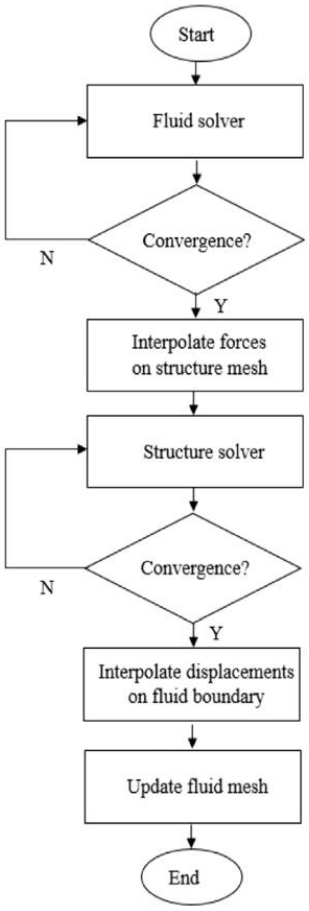

Figure 7. Single time step within a weak, two-way coupled FSI solver algorithm [17].

Increase in the available computational processing power has made it possible to conduct ever more complicated numerical analyses. The trend is visible in the scientific publications considering FSI. Accordingly, focus has been shifted from purely experimentally based analytical modelling to complex coupled numerical simulations which couple elastic solid mechanics and fully turbulent three-dimensional fluid flow. Beyond academia the same shift occurs in practical engineering as numerical analysis is more often the choice over conservative analytical methods. As this thesis focuses on the current state of the art numerical methods it is relevant to review how FSI has been discussed in scientific publications.

In naval architecture, a typical FSI problem is the rigid body ship motion coupled with the hydrodynamic effects. Typically, either the full six DOF ship motions or a selected reduced set of DOFs are calculated using potential flow theory [24]. The problem becomes more complex when the forces due to internal tank fluids, i.e., sloshing loads are considered. For example, such a problem was studied in [25]. In this case, sloshing loads were idealized using FEA and coupled with a six DOF ship motions model set in a certain sea state. Accordingly, the FSI problem was simulated in time domain and each time step dived into sub-iteration steps. The coupling effect was found to have a considerable impact on response parameters such as the roll amplitude.

In the field of naval architecture FSI with elastic solid mechanics has typically been limited to considering the hull girder responses under hydrodynamic loads. A comprehensive review on the topic is presented, e.g., by Hirdaris et al. [26]. The article describes the typical

dynamic hull girder responses of springing and whipping, i.e., the resonant and transient vibrations of the hull girder due to wave loads. The phenomenon of elastic hull response under hydrodynamic loads is termed hydroelasticity. [26] Modern approach to hydroelasticity couples RANS based CFD and structural FEA as in [27]. In the article, FSI simulation was conducted to study the dynamic behavior of a flexible barge in head waves. To fully consider the non-linearities arising during the wave-hull interaction, a strong two-way coupled approach was utilized. Comparison with model test results and two-dimensional linear hydroelastic simulation results showed that the RANS based FSI simulation could provide a more accurate estimate of when non-linear effects have strong influence. To the author's understanding no scientific publications exist dedicated to assessing fluid-structure interaction in wind-induced vibrations of ship deck outfitting structures.

A complex FSI case in the field of civil engineering has been studied by Xu et al. [19] in which the response of a three-span suspension bridge with two floating pylons due to aerodynamic and hydrodynamic effects were considered. In this study hydrodynamic effects, i.e., added mass, added damping and wave loads were modelled using potential flow theory. Wind forces due to mean wind speed as well as due to linear and nonlinear buffeting were considered. Detailed formulas for the force contributions are presented in the paper. The modelled fluid contributions were coupled into the structural model by implementing them into the equations of motion of the bridge discretized with FEA. The response of the bridge was then calculated in the time domain to account for the effects of non-linearity. It is stated that, although the section moment increased monotonically with wave height, the increasing average wind speed altered the systems properties. This combination makes it difficult to choose the correct worst-case scenario for design loads of the bridge. Similar challenges are present in the case study of this thesis. Due to the non-linear nature of VIV the worst-case wind load scenario is not trivial. Thorough worst-case scenario analysis would require multiple loading conditions of wind speeds in altering directions, possibly coupled with, e.g., a Monte Carlo analysis, as done in [19].

An article by Lee et al. [28] represents the state-of-the art in academic fluid-structure interaction simulation for VIV. The authors studied vortex-induced vibration of a hydrofoil in crashback condition, i.e., the propeller operating in the reverse direction. The numerical method applied hybrid RANS-LES with delayed detached-eddy simulation and high quality structured finite volume mesh to solve the fluid equations. Solid mechanics were solved using finite element method and the domain was discretized with quadratic elements. FSI coupling was done using a strongly coupled algorithm. Based on the comparison between experimental and numerical data the authors declare a reasonable agreement of the results. However, more accurate results could be achieved via further mesh refinement and a smaller time step. The simulated physical time in the study was only 2.5 s which was limited by the computational cost of the applied methods. Despite the considerable mesh size saving obtained by the structured finite volume mesh over an unstructured mesh, applying LES requires an unpractically small time-step.

As stated before, vortex-induced vibration and FSI problems in general are complex and numerically demanding problems and thus reducing the computational cost of simulations, especially in practical engineering, is important. One way of reducing the computation time is to reduce the model's DOFs. For fully three-dimensional problems this may be done by utilizing beam or plate, i.e., line or surface elements for the solid domain. Qian-bei et al. [29] utilized one-dimensional beam finite elements in conjunction with three-dimensional finite

volume method to study VIV of elastic tubes in cross flow. The weakly coupled FSI algorithm introduced in the article was validated with a model test. Considerable computational savings were shown using beam elements over fully three-dimensional solid elements. The ideal approach in the case study of this thesis would be to use either plate or beam elements to discretize the solid domain. However, the software used in the study only supports three-dimensional elements and therefore this approach remains a future development step.

2.4 Modelling approach

Practical engineering design and analysis work can be composed into a process described with a flow chart. To highlight and explicitly define the steps taken in the present study, the process is shown in Figure 8. The overall procedure can be divided into three phases where specific modelling steps are made. The first phase is termed pre-processing and it comprises of the steps from the first modelling assumptions to the selection of boundary conditions. The second stage is the solution, which includes the numerical computation of the problem at hand. This step is fully taken care of by the solvers integrated in the software and is only affected by the choices made in the pre-processing phase. The final phase of the procedure comprises of the results and possible validation step and it is called the post-processing phase.

This thesis mostly focuses on the steps involved in the pre-processing stage, as this is the phase in which the engineer's choices define the quality and validity of the obtained results. As seen from Figure 8, in the post-processing phase an unsatisfactory result may initiate a loop back to any of the steps in the pre-processing phase, thus initiating the process forward from that point on.

It is important to note that all the choices made during the pre-processing phase will eventually affect the obtained results to an extent. Therefore, all choices must be based on sound engineering judgement. The significance becomes especially clear when considering the first step of the entire modelling procedure, i.e., initial assumptions. Any unjustified, and thus false, assumptions will render the entire process useless even if all the rest of the steps would be done correctly.

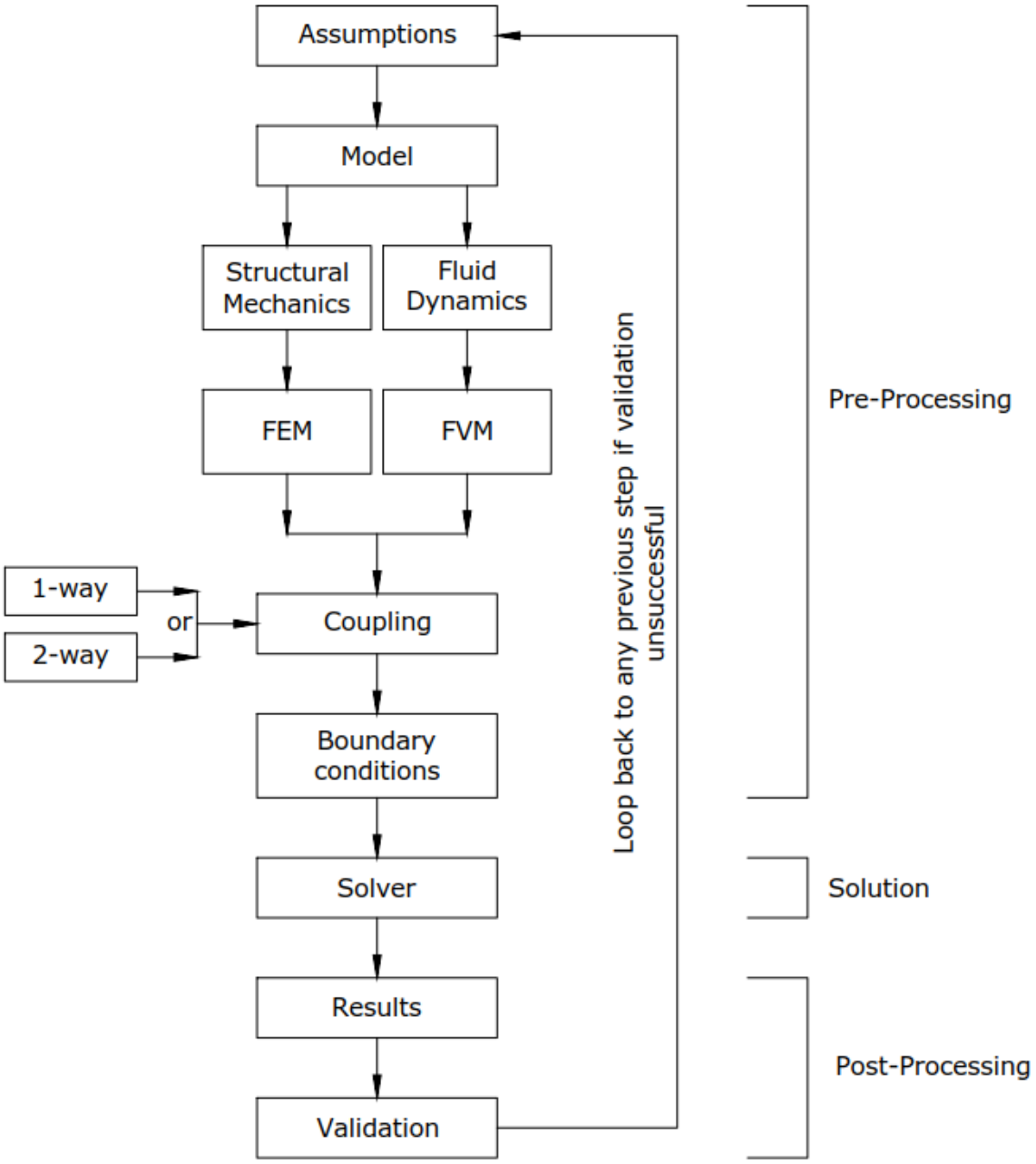

Figure 8. Modelling approach for fluid-structure interaction analysis.

3 Numerical method

A major part of the theory within modern engineering analysis is hidden inside the software used to solve the problem. However, understanding the underlaying theory is of utmost importance for the engineer and analyst to achieve results that have physical validity. Fluid-structure interaction problems contain both theory of fluid dynamics as well as of solid mechanics. In this chapter the relevant theories of both fields are presented.

The relevant theories have been derived by applying the principles of continuum mechanics, and a discretization scheme must be applied before a numerical solution can be calculated. The numerical methods are therefore an essential part of modern engineering analysis. The methods utilized in this thesis have been chosen from the most suitable state of the art methods available. The selection has been conducted reflecting on scientific publications, sound engineering judgement and within the limitations of the software. The commercial CFD software STAR-CCM+, that is used for the FSI analyses, utilizes the industry's most common methods for both CFD and structural dynamics, which are discussed in the following sections.

3.1 Fluid dynamics modelling assumptions

In this thesis the fluid domain has been idealized using the commercial software STAR-CCM+, which utilizes finite volume method to discretize the continuous governing equations. In this section the underlaying theory of fluid dynamics and the applied numerical methods are presented.

3.1.1 Governing equations

The physical fluid domain is associated with two physical conservation laws that govern the flow solution. These are the conservation of mass and momentum. The first can be expressed as the continuity equation [30]:

$$\frac{\partial \rho}{\partial t} + \nabla \cdot (\rho \mathbf{v}) = 0 \tag{5}$$

where ρ is the fluid density, t is time and $\mathbf{v}$ is the fluid velocity vector.

For the case considered in this thesis the Mach number is well below 0.3 (see Section 2.1) and for this reason the air flow may be considered incompressible. Thus, Eq. (5) can be further simplified for an incompressible fluid in the form [30]:

$$\nabla \cdot \mathbf{v} = 0 \tag{6}$$

The conservation of momentum of a fluid is expressed with the Navier-Stokes equations (N-S) [30]:

$$\frac{\partial \mathbf{v}}{\partial t} + \mathbf{v}(\nabla \cdot \mathbf{v}) = -\frac{1}{\rho}\nabla p + \nu \nabla^2 \mathbf{v} + \mathbf{g} \tag{7}$$

where is p the fluid pressure, ν is the fluid kinematic viscosity and $\mathbf{g}$ is the volume force vector.

Due to turbulence, the length and time scales within the simulated flow vary largely from the smallest eddies to the largest. This renders any direct computation of N-S computationally unfeasible, and therefore the effect of turbulence must be modelled. [30] Currently, the most widely used method for simulating turbulent flows is RANS. Other option could be to use LES or even hybrid RANS-LES idealization that could possibly result in mildly improved error margins at a considerably higher computational cost [28, 30, 31]. Accordingly, RANS was chosen as the numerical method in this thesis.

RANS are obtained through a time-averaging process where the instantaneous quantities, i.e., velocity and pressure are expressed as a sum of the average value and an instantaneous fluctuation. RANS equations together with the continuity equation are written as [32]:

$$\frac{\partial \bar{v}_i}{\partial x_i} = 0 \tag{8}$$

$$\rho \frac{\partial \bar{v}_i}{\partial t} + \frac{\partial}{\partial x_j}\left(\bar{v}_j \bar{v}_i\right) = -\frac{\partial \bar{p}}{\partial x_i} + \rho g_i + \mu\left(\frac{\partial^2 \bar{v}_i}{\partial x_j x_j}\right) - \rho \frac{\partial \overline{v_i' v_j'}}{\partial x_j x_i} \tag{9}$$

where v' is instantaneous velocity, x_i is the spatial coordinate and μ is the fluid dynamic viscosity. The final term of Eq. (9) is called the Reynolds stress. According to the eddy viscosity hypothesis this term represents the influence of turbulent viscosity [30]. It is solved using a separate turbulence model.

For this study the SST k-ω turbulence model by Menter [33] was chosen. The turbulence model choice was justified by reviewing scientific publications. For example, the wind-induced vibration study by Sun et al. [31] demonstrated that a standard k-ω turbulence model is superior over a k-ε turbulence model. The superiority of k-ω turbulence models compared to k-ε models in separated flows is discussed in [34]. Especially for aerodynamic flows, the benefit of SST k-ω turbulence model has been recognized [35]. The SST k-ω turbulence model has been successfully applied in multiple FSI studies, e.g., [3, 14, 15, 28, 36]. Specifically in wind, this turbulence model has been utilized to study the wind-induced heeling moment for the dynamic stability assessment of ships [37]. The STAR-CCM+ manual [22] also suggests using k-ω type turbulence models for aerospace applications, and specifically the SST k-ω model for most problems. Considering the above, SST k-ω is a justified turbulence model choice. In SST k-ω turbulence model, the turbulent dynamic viscosity ν_T is calculated using the turbulent kinetic energy per unit mass, k, and specific rate of dissipation of turbulent kinetic energy, ω [34]. Separate differential equations are used for both variables. Turbulent kinematic viscosity is calculated as $\nu_T = k/\omega$ [32].

RANS modelling only resolves the averaged flow properties as discussed above. However, near solid walls, i.e., on surfaces where the no-slip boundary condition is imposed, turbulence has pronounced and narrow amplitude fluctuations. Therefore, to resolve these accurately infeasibly small grid steps would be required in the normal direction to the wall. An additional problem near the wall may be related to the turbulent viscosity, which should decrease approaching the wall. RANS modelling is unable to predict this accurately and results in an exaggerated turbulent viscosity. Without an additional model the incorrectly computed wall region would eventually impede correct modelling of the entire flow region due to the convection of momentum. A method to solve this problem is to apply turbulence modelling starting from an extent off the wall and using wall functions in the near wall region. [30] This approach is used in the present study. In STAR-CCM+ the method is called

wall treatment. It uses the law of the wall and the consequent layers therein: viscous sublayer, buffer layer, and log-law layer, to compute the turbulence quantities. [22]

Wall treatment regions are divided into two layers depending on the non-dimensional cell centroid normal distance from the wall, y+. It is calculated as $y^+ = yv^*/\nu$. Parameter y is the cell center normal distance from the wall surface. The reference velocity v^* is calculated using a turbulence model dependent formula. Low-y^+ wall treatment is applied for the viscous sublayer, for which $y^+ < 5$. y^+ values near unity are preferred. High-y^+ treatment applies for $y^+ > 30$, i.e., in the log-law layer. For computational meshes where variable y^+ values are present in multiple ranges All-y^+ treatment may be applied. This approach combines the two previous y^+ treatments for the corresponding mesh y^+ values. Additionally, the method can deal with cells in the buffer layer region, i.e., $5 < y^+ < 30$. [22] To obtain good quality results meshes with y^+ values in the buffer layer region should be avoided. In this study All-y^+ wall treatment is used to cover varying y^+ ranges.

One more technique is required to solve the governing equations. The pressure gradient in Eq. (9) is a driving component of the velocity. However, no explicit equation exists to directly solve the pressure. Considering that the velocity field must satisfy the continuity condition given in Eq. (8), an indirect link exists between the velocity and pressure. The method used to derive the pressure is called pressure correction. For this purpose, iterative algorithms have been developed to solve the pressure for CFD applications. The typical algorithm, namely SIMPLE, utilizes an initial guess for the pressure field to compute the linearized momentum equation and continuity condition. A new pressure value is then computed within an iterative loop until convergence is achieved. [32]

3.1.2 Finite volume method

To obtain a numerical solution to a continuous equation such as Eq. (9), a discretization method must be applied. Generally, this means that all the parts within the equation are approximated with algebraic expressions. The most common discretization method utilized in commercial CFD is the finite volume method. The software used in this study, STAR-CCM+, applies this method to solve the numerical flow problem. Therefore, it is relevant to investigate this method further.

In FVM the continuous computational domain is divided into finite volumetric cells. These cells form the computational mesh and contain the flow quantities at a discrete point, i.e., cell center point and the cell surface center points. FVM differs from many other simpler discretization methods, e.g., finite differencing by applying the discretization directly to the integral forms of the governing equations, which are written for an arbitrary control volume. This arbitrary control volume, shown in Figure 9, has surface areas S_i, surface normals $\mathbf{n_i}$, and a finite volume Ω. Each cell of the computational mesh is considered as a control volume for which the integral equations may be applied to. As the values for S_i, $\mathbf{n_i}$, and Ω are known for each cell, the integral equations may be approximated with algebraic equations. These discretized equation equations utilize the parameter values at adjacent cells, e.g., for derivative values. Additional interpolation schemes must be applied for the surface integrals that utilize the parameter values at the cell surfaces. [30]

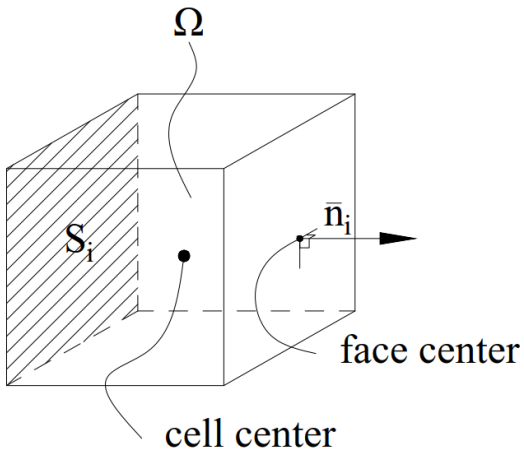

Figure 9. Arbitrary finite volume cell.

FVM discretizes the spatial domain and therefore a temporal discretization is still required to obtain an algebraic representation for the time derivatives. Similarly, as the spatial domain is divided into discrete cells, the time domain is also divided into discrete time steps. There are two different temporal discretization approaches: explicit and implicit schemes [30]. The first utilizes values from the present time step, n, and the previous time step, n-1. Thus, it can be solved explicitly. Implicit schemes also utilize values from the next time step, i.e., n+1. Therefore, they cannot be solved explicitly but as a system of algebraic equations [30]. Commercial CFD often utilizes implicit schemes despite higher computational cost over explicit schemes as they result in more stable solutions [30]. An implicit scheme is also applied in the present study as, despite higher computational cost, it leads to superior stability of the solution and allows for a larger time step [30].

A typical time derivative present in Eq. (9) is the first time derivative of velocity $\partial v_i/\partial t$. To derive a numerical scheme the following approach may be taken using the Taylor series expansion. First, the Taylor series expansion for the next time step of v^{n+1} is written:

$$v_i^{n+1} = v_i^n + \frac{\partial v}{\partial t}\Big|_i^n \Delta t + O((\Delta t)^2) \tag{10}$$

where n is the time step and i is the spatial step. Higher-order terms in the Taylor series expansion are represented by $O((\Delta t)^2)$.

Now, modifying the above equation, the derivative can be expressed as:

$$\frac{\partial v}{\partial t} = \frac{v_i^{n+1} - v_i^n}{\Delta t} + O(\Delta t) \tag{11}$$

Neglecting the higher order terms, a first-order forward difference scheme is achieved with a truncating error of $O(\Delta t)$ [30]. This presents how temporal discretization is derived via Taylor series expansion. Higher-order methods may be derived using multiple Taylor series expansions. For the present study, the simple scheme presented in Eq. (11) would not be sufficiently accurate as it would lead to unacceptably high numerical dissipation [30]. Therefore, an implicit, second-order scheme, i.e., with a truncating error decreasing to the second power of Δt is applied. The solver used in STAR-CCM+ is called Implicit Unsteady [22].

The discretized set of governing equations are solved in STAR-CCM+ with Segregated Flow solver algorithm [22]. It calculates the conservation equations sequentially solving for the three velocity components $\mathbf{v_x}$, $\mathbf{v_y}$, $\mathbf{v_z}$, and pressure **p** by the SIMPLE pressure correction algorithm (see Section 3.1.1). The discretized system of algebraic equations is solved iteratively using an algebraic multigrid method. The algorithm is called AMG Linear and it applies under-relaxation sweeps [22]. Under-relaxation applies a relaxation factor between 0.0 and 1.0 that is used to multiply the difference between the current and previous parameter approximation. New approximation is obtained as a sum of the previous iteration value and the under-relaxed difference. The procedure is used reduce possible overshoot of the approximation and thus accelerate the convergence of the iterative solution. [30] The difference between the exact and the approximate solution is termed the residual value. The iterative procedure calculates the change of the desired parameter value, e.g., $\mathbf{v_x}$ that results in a specific residual value. These residual values are monitored to determine when the convergence criterion is satisfied, i.e., when the residual value is below a certain limit. [22] (see Section 3.2.2)

3.2 Structural response

In this study solid mechanics are calculated based on the assumption of small displacements. This justifies the use of linear elastic theory to model the structural behavior. The structural response is calculated using the Solid Stress solver available in STAR-CCM+ [22]. The applied numerical method is linear FEA.

3.2.1 Solid mechanics

FSI problems are inherently dynamic problems. The solid domain is governed by the equilibrium equations together with the strain-displacement relation and the stress-strain relationship [38]. The equilibrium of a continuous solid domain with multiple degrees of freedoms is expressed by the Newton's equation of motion, which in matrix form is written as [39]:

$$\mathbf{M\ddot{u}} + \mathbf{C\dot{u}} + \mathbf{Ku} = \mathbf{f} \tag{12}$$

where **M** is the mass matrix, **C** is the damping matrix and **K** is the stiffness matrix. The structural motions are represented by the acceleration vector $\ddot{\mathbf{u}}$, the velocity vector $\dot{\mathbf{u}}$ and the displacement vector **u**. The external force contributions on the structure are represented by the external force vector **f**.

The mass matrix represents the inertia of the structural system. The damping matrix contains the components, which contribute to the dissipation of energy during structural motion. The stiffness matrix describes the stiffness properties of the structure. [39] In the present study, the external force contributions include the gravitational body force and surface traction.

Deformations in the solid domain are described by the strain tensor, which is obtained through the strain-displacement relationship. Assuming linear elastic material behavior, i.e., small strains, the relationship is expressed as [39]:

$$\boldsymbol{\varepsilon} = \mathbf{Bu} \tag{13}$$

where $\boldsymbol{\varepsilon}$ is the strain matrix and **B** is the strain-displacement matrix, which contains the derivatives relating displacements to stresses. The constitutive relation which relates the deformations to stresses under the linear elasticity assumption is given by the Hooke's law [38]. In matrix form it is written as [40]:

$$\boldsymbol{\sigma} = \mathbf{D}\boldsymbol{\varepsilon} \tag{14}$$

where $\boldsymbol{\sigma}$ is the symmetric Cauchy stress tensor, **D** is the material parameter matrix and $\boldsymbol{\varepsilon}$ is the strain matrix. In the case study of this thesis, in addition to linear elastic, the material properties are assumed isotropic. Therefore, matrix **D** is symmetric and fully defined by the material parameters, which are the Young's modulus, E, and the Poisson's ratio, ν_p [39].

For dynamic problems where the structural system is placed within a fluid domain, the solid motion also induces the motion of the fluid. Therefore, the system experiences an additional mass effect called the added mass, $\mathbf{M_f}$. Including the added mass, Eq. (12) is written as [40]:

$$(\mathbf{M} + \mathbf{M_f})\ddot{\mathbf{u}} + \mathbf{C}\dot{\mathbf{u}} + \mathbf{K}\mathbf{u} = \mathbf{f} \tag{15}$$

When structural systems are analyzed in air, the density of air is considerably lower than the density of the structure. Therefore, the added mass term may be neglected. However, in typical marine application where the system is placed in water the added mass must be considered. In STAR-CCM+ the added mass effect is automatically computed when solving two-way coupled FSI problems [22]. Therefore, in the case study the added mass is included in the two-way coupled model.

3.2.2 Finite element method

Similarly to FVM in CFD, in structural dynamics the continuous solid domain is divided into discrete finite partials called finite elements. Each finite element is formed by nodes at the element corners, e.g., four nodes at the corners of a two-dimensional plate element. The displacement field within the analyzed solid part is described by the displacement of all the elemental nodes, i.e., as a sum of the elemental subdomains [41].

To obtain a numerical approximation of the exact solution the nodal displacements are expressed in terms of shape functions. The displacement field is solved at the nodes and intermediate values are calculated through interpolation using the shape functions. [42] In conventional engineering polynomial shape functions are used which are either linear or, if higher-order shape functions are used, second-order polynomials. In STAR-CCM+ both linear and quadratic finite elements based on Lagrange shape functions are available [22]. The solid displacement field is expressed in terms of the shape functions and nodal displacement values as [41]:

$$\mathbf{u}(\mathbf{x},t) = \mathbf{N}(\mathbf{x})\mathbf{u_n}(t) \tag{16}$$

where **N** is the matrix that contains the shape functions and $\mathbf{u_n}$ is the nodal displacement vector.

Applying the principle of virtual work to the equilibrium equations of the structural system, the problem is expressed in the weak form. The integral form utilizes the arbitrary variables, virtual displacement and virtual strain. The weak form expression is written as [40]:

$$\int_\Omega \delta\mathbf{u}^T\rho_s\frac{\partial^2\mathbf{u}}{\partial t^2}d\Omega+\int_\Omega \delta\mathbf{u}^T\mu_s\frac{\partial\mathbf{u}}{\partial t}d\Omega+\int_\Omega \boldsymbol{\delta\varepsilon}^T\mathbf{D}\boldsymbol{\varepsilon}d\Omega-\int_\Omega \delta\mathbf{u}^T\mathbf{b}d\Omega-\int_\Gamma \delta\mathbf{u}^T\mathbf{t}d\Gamma=0 \quad (17)$$

where Ω is the solid volume, Γ is the solid surface, ρ_s is the solid material density, μ_s is the viscous structural damping, $\mathbf{t}$ is the surface traction and $\mathbf{b}$ is the body force. Inertia, damping, stiffness and force matrix contributions from Eq. (12) are represented in the same order in Eq. (17). The first integral represents the inertia of the system, the second integral is the damping and the third is the stiffness contribution. External forces are divided into two integral components. These are the volumetric body force and the surface traction, respectively.

The variational forms of the displacement field in Eq. (16), and the strain-displacement relation in Eq. (13) are given as [40]:

$$\boldsymbol{\delta u} = \mathbf{N}\boldsymbol{\delta u_n} \quad (18)$$

$$\boldsymbol{\delta\varepsilon} = \mathbf{B}\boldsymbol{\delta u} \quad (19)$$

Introducing the finite element approximation, i.e., the displacement field discretization of Eq. (16), the weak form in Eq. (17) is approximated as the sum of the integrals over the individual elements. The discretized equation system in which the existing initial stresses and strains have been neglected is expressed as [42]:

$$\sum_e \delta\mathbf{u}_\mathbf{n}^T\left(\int_{\Omega_e}\mathbf{N}^T\rho_s\mathbf{N}d\Omega\,\ddot{\mathbf{u}}_\mathbf{n}+\int_{\Omega_e}\mathbf{N}^T\mu_s\mathbf{N}d\Omega\dot{\mathbf{u}}_\mathbf{n}+\int_{\Omega_e}\mathbf{B}^T\mathbf{D}\mathbf{B}d\Omega\mathbf{u}_\mathbf{n}-\int_{\Omega_e}\mathbf{N}^T\mathbf{b}d\Omega-\int_{\Gamma_e}\mathbf{N}^T\mathbf{t}d\Gamma\right)=0 \quad (20)$$

As the virtual displacement is an arbitrary variable the equation must be valid for all virtual displacements. Thus, the virtual displacement can be cancelled from the expression. Now the equation set can be grouped into matrix forms consisting of the integral elemental contributions. This takes the form [42]:

$$\widetilde{\mathbf{M}}\ddot{\mathbf{u}}_\mathbf{n}+\widetilde{\mathbf{C}}\dot{\mathbf{u}}_\mathbf{n}+\widetilde{\mathbf{K}}\mathbf{u}_\mathbf{n}=\tilde{\mathbf{f}} \quad (21)$$

where the element mass matrix is $\widetilde{\mathbf{M}}=\sum_e\int_{\Omega_e}\mathbf{N}^T\rho_s\mathbf{N}d\Omega$, the element damping matrix is $\widetilde{\mathbf{C}}=\sum_e\int_{\Omega_e}\mathbf{N}^T\mu_s\mathbf{N}d\Omega$, the element stiffness matrix is $\widetilde{\mathbf{K}}=\sum_e\int_{\Omega_e}\mathbf{B}^T\mathbf{D}\mathbf{B}d\Omega$ and the element external force matrix is $\tilde{\mathbf{f}}=\sum_e(\int_{\Omega_e}\mathbf{N}^T\mathbf{b}d\Omega+\int_{\Gamma_e}\mathbf{N}^T\mathbf{t}d\Gamma)$.

The matrices in Eq. (21) are assembled from the submatrices of the individual elements. The submatrices are calculated through numerical integration over the element domain with a suitable quadrature [40]. The present study is conducted with the finite element solver integrated in STAR-CCM+, which applies the Gaussian quadrature [22].

As can be seen from the mathematical descriptions of the elemental matrices, the stiffness and mass matrices are defined by the generally known material parameters, described in Section 3.2.1. However, the definition of the damping matrix is not trivial, as the structural damping parameter, μ_s, is not known [40]. One approach to solve the issue is to assume Rayleigh damping [40], which is the approach used in STAR-CCM+ [22]. Rayleigh damping

assumes that the damping matrix may be expressed as a linear combination of the mass and stiffness matrices [40]:

$$\mathbf{C} = \alpha\mathbf{M} + \beta\mathbf{K} \tag{22}$$

where α is the mass-proportional Rayleigh damping coefficient and β is the stiffness-proportional Rayleigh damping coefficient.

Through a technique called modal analysis the structural natural frequencies and corresponding eigenmodes can be obtained in the frequency domain from Eq. (12). Both the mass and stiffness matrices are diagonalized in the process. As Rayleigh damping is assumed, the damping matrix, being the above described linear combination in Eq. (22), becomes diagonal as well. Assuming modal damping, the result is a set of diagonal, uncoupled matrices in which each equation represent one degree of freedom. An arbitrary degree of freedom in Eq. (12) may be written in terms of the modal degrees of freedom, q_i, as [39]:

$$\ddot{q} + 2\zeta_i\omega_i\dot{q} + \omega_i^2 q = g_i \tag{23}$$

where ζ_i is the modal damping ratio, ω_i is the i^{th} natural frequency and g_i is the generalized load in the modal system. $2\zeta_i\omega_i$ is expressed using the Rayleigh damping coefficients as $\alpha + \omega_i^2\beta$. Factors α and β may be obtained through experiments [40]. Rayleigh damping can also be expressed as either purely stiffness-proportional damping for which $\alpha = 0$, or mass-proportional damping, $\beta = 0$. Stiffness-proportional damping describes the internal material damping, whereas mass-proportional is a measure of frictional damping. [39]

The structural damping component in dense fluids, e.g., for structures in water, may be assumed zero in computational analysis, as it is negligibly small compared to the added damping due to the induced fluid motion [9]. For the scope of this thesis, obtaining the structural damping factors experimentally is unfeasible. As in [13], the case study structure is assumed lightly damped. A conservative approach in which structural damping is neglected should result in the maximum response amplitudes [6, 18]. Therefore, in this study additional structural damping has been neglected, i.e., $\alpha, \beta = 0$.

The coupled structural dynamic response has been solved directly in the time domain. Therefore, modal analysis has only been applied for preliminary structural analysis using NX Nastran [43]. As seen in section 3.1.2 for transient fluid dynamic solutions, an additional discretization in the time domain is required to solve the dynamic structural system presented in Eq. (21). In STAR-CCM+ the dynamic structural system is solved using either backward Euler or Newmark methods, which are first-order and second-order accurate in time, respectively [22]. These are direct analysis methods which solve the following time step value through interpolation over a discrete time step [39]. As temporal accuracy is desired for the study case presented in this thesis, second-order accurate method was considered more suitable. Additionally, it leads to lower numerical damping [22]. Second-order temporal discretization is also automatically enforced as a second-order temporal scheme is applied in the fluid domain. Therefore, the Newmark method was applied.

To solve the finite element problem, the above introduced equations are ordered into a single matrix. For simplicity, a purely quasi-static solid mechanics problem is presented. In FEA this is written as [42]:

$$\mathbf{K}\mathbf{u}_\mathbf{n} = \mathbf{f}_\mathbf{n} \tag{24}$$

To solve the nodal displacements, $\mathbf{u_n}$, the stiffness matrix $\mathbf{K}$ must be inverted. Multiplying with the inverted matrix gives the displacement values as [42]:

$$\mathbf{u}_\mathbf{n} = \mathbf{K}^{-1}\mathbf{f} \tag{25}$$

However, the number of DOFs, i.e., the number of unknown displacement values is typically very large. The size of the stiffness matrix is even larger as it is a n_{dof} times n_{dof} matrix. For a dynamic problem the matrix is even more complicated as it has contributions from the mass and damping matrices as well as the chosen time discretization [22]. Therefore, a simple matrix inversion is not feasible. In STAR-CCM+ the solution is obtained using a sparse direct matrix solver algorithm, MUMPS [22, 44]. This is an iterative method in which Eq. (24) is expressed in the following form [42]:

$$\mathbf{f} - \mathbf{K}\mathbf{u}_\mathbf{n} = \mathbf{r} \tag{26}$$

where $\mathbf{r}$ represents the residuals of the equations.

Eq. (26) may be written with an effective stiffness matrix. Introducing the iterative displacement step the problem is now written as [22]:

$$\mathbf{K}^\mathbf{i}\Delta\mathbf{u}_\mathbf{n}^\mathbf{i} = \mathbf{r}^\mathbf{i} \tag{27}$$

where i is the iteration step, $\mathbf{K^i}$ is the stiffness matrix at iteration step and $\Delta\mathbf{u}_\mathbf{n}^\mathbf{i}$ is the displacement iteration step. The displacement step is used to update the initial displacement field as $\mathbf{u}_\mathbf{n}^{\mathbf{i+1}} = \mathbf{u}_\mathbf{n}^\mathbf{i} + \Delta\mathbf{u}_\mathbf{n}^\mathbf{i}$. Boundary conditions provide the initial conditions for the first iteration step. The residuals at each iteration step are calculated as $\mathbf{r}^\mathbf{i} = \mathbf{f} - \mathbf{K}^\mathbf{i}\mathbf{u}_\mathbf{n}^\mathbf{i}$. The iteration procedure continues until the residuals converge below a set tolerance level.

3.3 Fluid-structure coupling

To numerically solve partitioned fluid-structure interaction problems the separate solver interfaces for fluid and structural systems must be coupled. In most cases the two solvers have separate dedicated software, which would require an external code or program to transfer the information between the solvers. However, STAR-CCM+ has both the CFD and structural FEA integrated within the same software, thus making an external coupling code unnecessary.

The coupling in STAR-CCM+ is done with the dedicated Fluid Structure Interaction solver [22]. This is an implicit solver, which applies fixed-point iterative method. Under-relaxation is used to accelerate the convergence. A fluid-structure interface surface is created at the surface where the fluid and structural domains meet. This surface is used to map and transfer the fluid loads onto the finite element mesh. Similarly, in the case of two-way coupling the structural displacements are transferred to the fluid mesh along the interface. The surface type in STAR-CCM+ used for FSI problems is Mapped Contact Interface [22]. It allows for non-conformal meshing to be used at the interface of the fluid and solid regions. Cell faces on the fluid region are linked with cell faces on the solid mesh with a proximity-based algorithm. The forces transformed from the fluid to the solid domain are termed mapped reaction forces. A conceptual presentation of the mapping is shown in Figure 10 where the

fluid pressures from the CFD finite volume cells are mapped onto the adjacent finite element vertices.

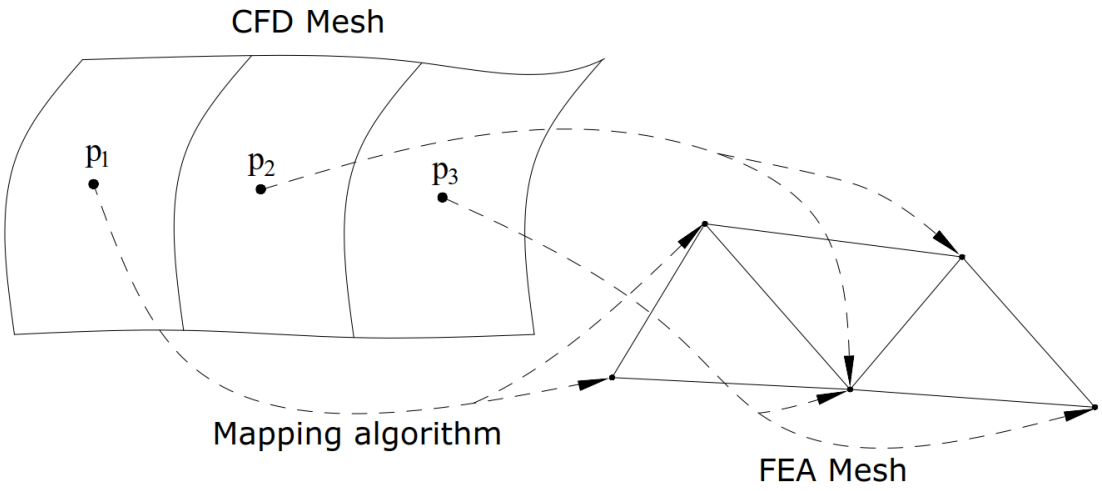

Figure 10. Conceptual representation of the mapping algorithm.

In the case of two-way coupled FSI simulations an additional simulation step is required to account for the solid deformations and the subsequent change in the fluid domain. This is done via a mesh morphing algorithm which transforms the fluid domain according the solid displacement. The morphing boundary defines a set of control points which are each associated with a solid displacement vector. The finite volume mesh motion is then interpolated from these displacement vectors. The morpher redistributes the fluid mesh vertices according to the interpolation field. Space conservation law is applied in the moving control volumes. [22] This enforces the conservation of mass within the moving domain by including the change of volume and relative velocity into Eq. (6) [7]. In STAR-CCM+, two-way coupling also activates the automatic added mass control discussed in Section 3.2.1.

The following subsections cover the details and the numerical approaches used in the case study. First, the one-way coupling approach is discussed. This is followed by the two-way coupling procedure.

3.3.1 One-way coupling

One-way coupled fluid-structure interaction is suitable for problems in which the two domains are weakly coupled. This requires that the structural response has negligible effect on the fluid flow. [22] The benefit of one-way coupling is that it offers considerably lower computational cost over two-way coupling and that it does not require additional methods to account for the motion of the fluid mesh [20].

The solver approach for one-way coupled FSI simulation used in the current study is illustrated in Figure 11. First, the fluid domain problem is solved in an iterative time loop in which each time step, Δt_i, is divided into subiteration steps. The iterative loop solves each time step until a convergence criterion or maximum number of iterations is satisfied. The fluid flow is solved until overall physical flow time limit is reached. Solvers used in the simulation are listed for both domains in the flow chart.

The flow solution results in transient pressure and shear loads, which are mapped onto the fluid-structure interface surface. Through the interface surface the pressure and shear loads are transferred onto the structural solver as an external dynamic force load, $\tilde{\mathbf{f}}$, presented in Eq. (21). The finite element structural solver then solves the dynamic structural response directly in time domain using the Newmark method. The approach used in the current study calculates the structural response within the same time loop as the fluid domain with the same time step value.

The result of the one-way coupled approach is the dynamic structural response which is obtained as a time signal in the time span of the fluid flow. As can be seen in Figure 11, data between the structural and fluid domains is only transferred in one direction. No information of the structural response is mapped back onto the fluid domain.

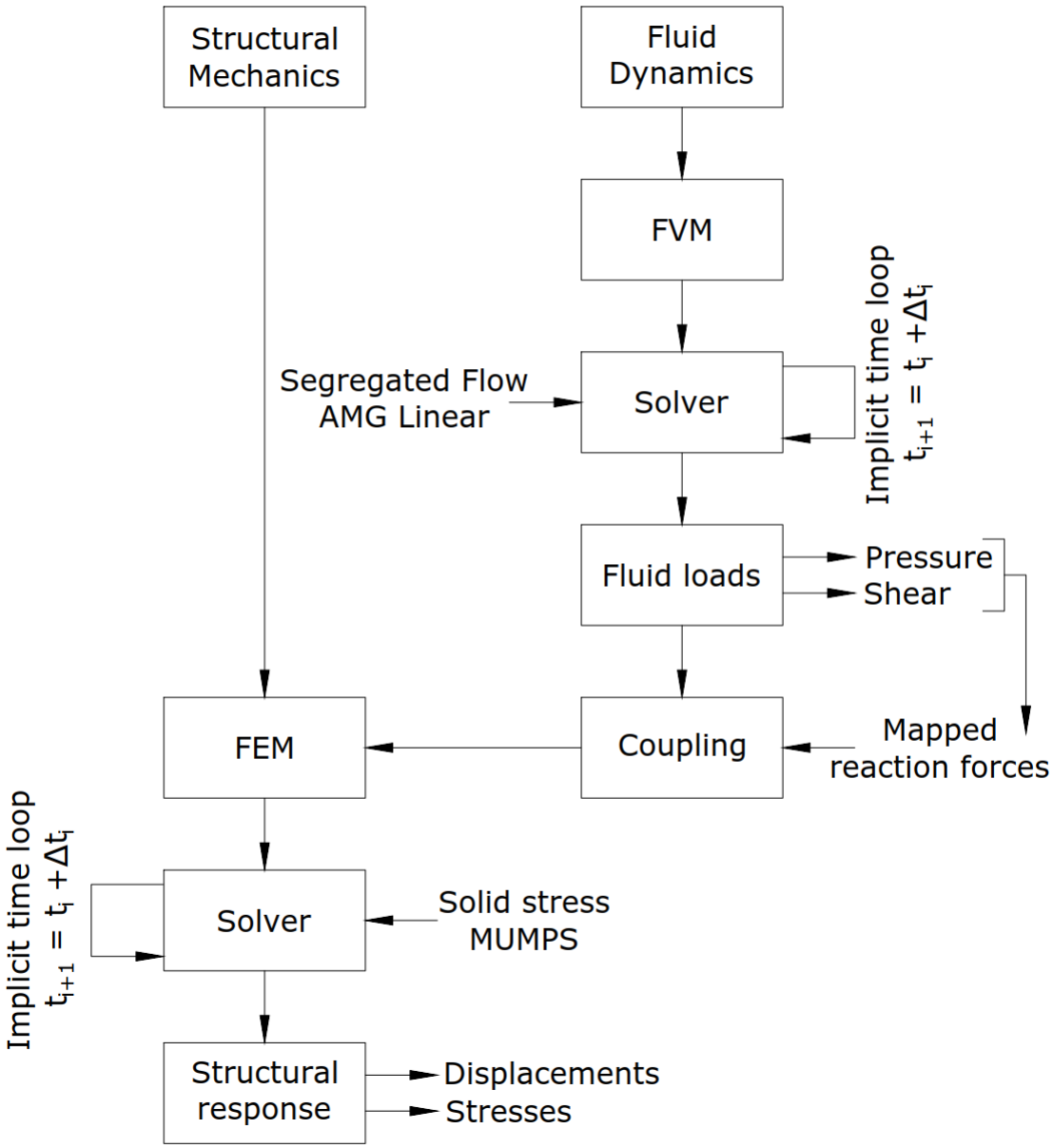

Figure 11. One-way coupled FSI solver approach.

3.3.2 Two-way coupling

The two-way coupled solver approach is illustrated in Figure 12. Two-way coupling approach is suitable for FSI problems where the fluid and solid physics are strongly coupled, i.e., the structural response has considerable influence on the fluid domain [20, 22].

Two-way coupled solver algorithm can be realized either by weak or strong coupling approaches. Weakly coupled FSI solution is done explicitly, i.e., the fluid loads and corresponding structural displacements are exchanged between the two solvers only once per each time step. This is equivalent to the flow chart path in Figure 12, where the check convergence step is always “Yes”. The fluid solver, however, is run iteratively as shown in Figure 11 since the flow solution must converge at each time step before coupling.

In the present study a strongly coupled FSI approach is employed. Strong two-way coupling is realized implicitly. The information of fluid loads and structural displacements are exchanged multiple times within a time step. In the case study simulation this is done at each subiteration step. This process is continued until either the convergence tolerance is met or the maximum number of iterations is reached, after which the algorithm moves onto the next time step.

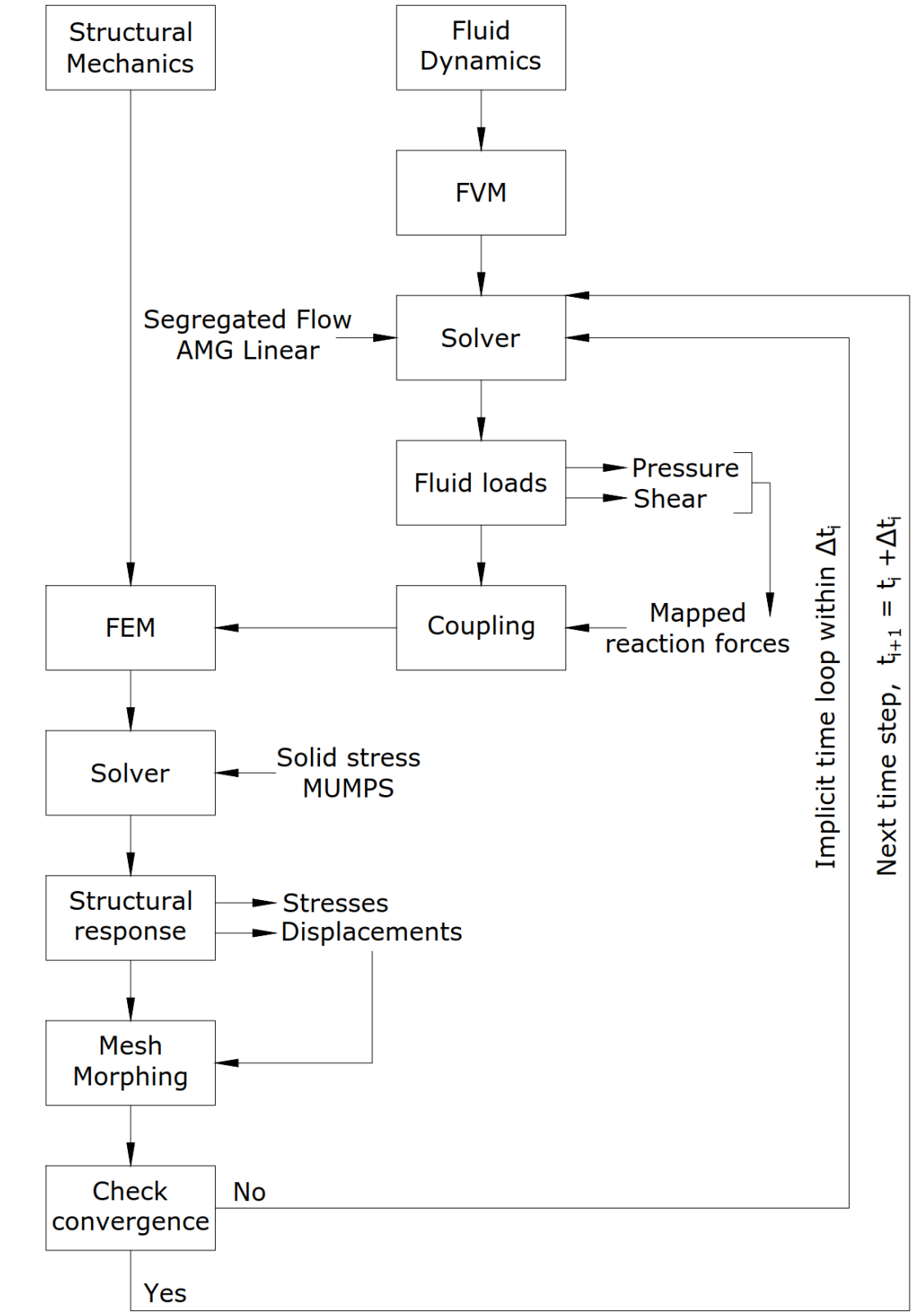

Figure 12. Two-way coupled FSI solver approach.

4 Case study

The presented case study aims to investigate how current industry state of the art one-way coupled fluid-structure interaction modelling compares with the more complex strong two-way coupled FSI simulation. Additional comparison of the coupled results is made with conservative quasi-static and quasi-dynamic analyses. This combination aims to uncover the differences between the different modelling approaches and to serve as a benchmark for future development. Multiple numerical models are employed to compensate for the lack of experimental and model test data.

As the analysis geometry, a typical deck amusement structure was idealized as a portal frame. The structure was excited by a constant velocity wind directed perpendicularly towards the frame. The case was studied for a total simulation time of 10.0 s. Both coupled FSI analyses were conducted using commercial CFD software Simcenter STAR-CCM+ version 2019.1, which includes a structural solver for linear elastic solid mechanics. Additionally, commercial FEA program Femap version 12.0.0 was used to model the geometry. Eigenmodes and natural frequencies of the portal frame were obtained prior to the coupled analysis using the structural solver NX Nastran version 12.0.2 integrated in Femap. These values were used as parameters for the coupled analyses' velocity boundary condition to set it to a range in which vortex-induced vibrations are likely to occur. Additionally, they serve as a baseline for the transient results. Quasi-static and quasi-dynamic results were also computed by NX Nastran.

CFD and FSI simulations were computed on a workstation with an Intel Xeon Gold 6140 2.30 GHz processor. Eleven processor cores were allocated for the computation. All FEA calculations with NX Nastran were completed on a PC with an Intel i5-7200U 2.50 GHz processor and four cores.

4.1 Portal frame structure

The portal frame structure is presented in Figure 13. The structure is made of aluminum and its topology and dimensions are similar to typical amusement structures found on the upper decks of modern cruise ships. The dimensions and material parameters are presented in detail in Table 2. The objective of the portal frame idealization has been to reduce the complexity of a complete amusement structure to a level that can be comprehensively analyzed using multiple models. The key principle has been to retain the geometrical properties that are relevant for the vortex shedding phenomenon. The modelled structure is composed of three differing geometric sections: one horizontal cylinder, two horizontal box beam sections supporting the cylinder, and two cylindrical pillars supporting the entire structure. All parts are hollow and characterized as thin-walled for the wall thickness to length ration is small, i.e., $t \ll L$. There is an opening on the pillar surface inside the connection of the box beam and the pillar. The structure is fixed to its foundation at the lower ends of the pillars.

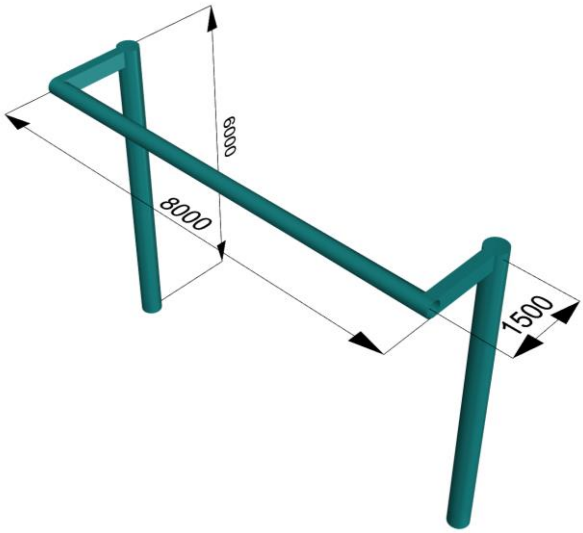

Figure 13. The portal frame structure analyzed in the case study. Dimensions are in mm.

Before conducting the coupled FSI analysis, an uncoupled eigenmode analysis was conducted to identify the dry eigenmodes and corresponding natural frequencies of the structure. These are called the dry eigenmodes as aerodynamic effects, namely aerodynamic damping and added mass, are not considered. The analysis was done using the commercial FEA solver NX Nastran which utilizes a modal analysis technique to calculate the structural eigenmodes and mode shapes. The modal analysis solver is known as SOL 103 within the software [43].

Table 2. Dimensions and material parameters of the portal frame

Parameter	Value
$L_{cylinder}$	8000 mm
$D_{cylinder}$	300 mm
$t_{cylinder}$	8 mm
H_{box}	300 mm
b_{box}	200 mm
t_{box}	8 mm
L_{box}	1500 mm
H_{pillar}	6000 mm
D_{pillar}	400 mm
t_{pillar}	12 mm
ρ_{Al}	2800 kg/m^3
E	69 GPa
ν_p	0.33

It would have been ideal to conduct the modal analysis using the same three-dimensional solid element mesh as in the FSI calculations. However, it was neither possible to conduct the modal analysis in STAR-CCM+ nor to export the solid mesh to be analyzed with NX Nastran. Therefore, the structure was discretized using eight-noded, quadratic plate elements in Femap. Using plate elements was justified, as the structure is thin-walled [42]. Plate elements are the industry standard element for local structural analysis. The global element

size was set to 50 x 50 mm according to DNV GL standard for local finite element analysis [45]. Quadratic elements, i.e., discretized with second-order polynomial shape functions were used to improve the accuracy of the solution without increasing the element count [38]. The model consisted of 9742 plate elements and 24 triangular elements. A fixed nodal boundary condition was set at the nodes on the pillar end surfaces. Fixed boundary condition prohibits both displacements and rotations at the selected nodes. Based on engineering judgement the model is believed to give a good representation of the system's dynamic behavior.

Table 3. Results of the portal frame's dry modal analysis.

Mode no.	Natural frequency [Hz]	Reduced velocity	Mode shape
1	5.9	10.13	
2	6.8	8.82	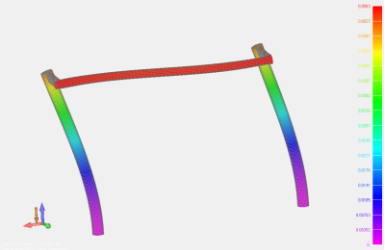
3	8.4	7.18	
4	13.8	4.34	
5	16.4	3.66	

The results of the modal analysis consist of the ten first, i.e., lowest natural frequencies and the corresponding eigenmodes. The frequency results for the first five natural frequencies are presented along with the corresponding reduced velocities in Table 3. Mode shapes are shown colored with the normalized total displacement. All observed eigenmodes are characterized as antisymmetric since the deformations include both bending and torsion. Deformations in the figures have been scaled to magnify the characteristic behavior. Two of these natural frequencies are within the expected VIV range of $4 < V_r < 8$, suggested by [4]. These modes are numbers three and four.

Results of the preliminary calculations were used to initialize the FSI analyses so that the imposed wind velocity is in a relevant range. They were also used in the analysis of the case study results to identify the vibrational modes of the portal frame undergoing VIV. It should be noted that natural frequencies of the plate model may differ from that of the solid element model.

4.2 Environmental conditions

The portal frame structure is located on the wind-exposed top deck of a cruise ship. In the case study the structure was exposed to a constant head wind condition with a uniform velocity field. The cruise ship was assumed to sail with a typical operational speed of 18.0 knots.

During operation, the ship encounters multiple sea states which may be characterized by the Beaufort scale [46]. The top deck was assumed located at 50 m above the sea surface. The wind speed at the top deck level may be obtained using a logarithmic wind speed profile suggested in [4]. When the wind speed was calculated, the ship's head speed was also accounted for. In the case study the structure was analyzed at a Beaufort number of 5 which is described as a fresh breeze [46]. At this Beaufort number, the average wind speed 10 m above the sea surface is 10.7 m/s [46]. The resulting wind speed at the top deck level was 18.07 m/s. A constant 35 knots wind speed was adopted which corresponds to 18.0 m/s. The wind speed at this Beaufort number results in favorable vortex shedding characteristics for the case study. Additionally, it does not represent an ultimate limit case but rather a normal operational condition.

Table 4. Fluid properties and characteristic vortex-shedding parameters.

Parameter	Value
ρ_{air}	1.225 kg/m^3
μ	1.85508 x10^{-5} Pa·s
U	18.0 m/s
Re	2.9 x10^5
St	0.23
f_s	13.8 Hz

The material parameters adopted for air in the case study are presented in Table 4, along with the results of the following calculations. Vortex-induced vibration is expected to occur mainly for the cylinder part, as it is a slender section and less stiff compared to the pillars and box beams. The Reynolds number of the considered cylinder section was calculated applying Eq. (1). Based on Table 1, the resulting Re = 2.9 x10^5 suggests that the wake is

fully turbulent, which supports the use of RANS fluid modelling over simplified methods. The Strouhal number at this Reynolds number range for a smooth, vibrating circular cylinder is approximately 0.23 [4]. According to Eq. (2), the corresponding vortex shedding frequency is 13.8 Hz. As the shedding frequency is very close to the portal frame's 4^{th} eigenmode's natural frequency, it should lead to a detectable lock-in phenomenon [1]. Resonance might also occur as the frequencies are close to identical.

4.3 CFD model

This section introduces the computational fluid dynamics model used for the case study. Special attention is given to the computational mesh and the boundary conditions. The numerical schemes used in the fluid solver are also summarized.

The numerical schemes used in the CFD calculations are presented in Table 5. For the CFD case alone, a longer time step than $1/10^{th}$ of the vortex oscillation period might be sufficient [47]. However, for FSI calculations a smaller time step, equal to $1/100^{th}$ of the period of the highest considered eigenmode, is suggested by the STAR-CCM+ manual [22]. Similar time step has been utilized in [47]. The required time step would be computationally unfeasible and thus a larger time step was chosen at the cost of reduced accuracy. The time step used in the calculations was 0.002 s, which is approximately 1/36 of the period of the 5^{th} eigenmode of the structure and 1/84 of the period of the 1^{st} eigenmode. The larger time step does not capture any high-order oscillations such as seen in the FSI study by [47]. In the present case such small amplitude high frequency vibrations are considered beyond the practical scope, especially considering that all structural damping is neglected. The time step used in the present study is a compromise between temporal accuracy and computational efficiency.

Each time step was divided into ten iteration steps within the Implicit Unsteady time discretization scheme. The required number of iterations was experimentally determined before conducting the simulations by monitoring the convergence of velocity values in specific domain locations together with the residual values. The utilized Segregated Flow solver used under-relaxations factors of 0.8 and 0.2 for velocity and pressure, respectively. Gradient values were solved using Hybrid Gauss-Least Squares Method, details of which may be found in [22].

Table 5. Finite volume discretization schemes utilized in the CFD simulations.

Domain	Scheme	Order of accuracy
Temporal	Implicit Unsteady	2^{nd}
Spatial	Second-Order Upwind	2^{nd}
Gradients	Hybrid Gauss-LSQ	-

The computational mesh was constructed using two primary meshers: Trimmed mesher and Prism Layer mesher [22]. Trimmed mesher was used to generate the primary cell grid whereas Prism Layer mesher was used at the solid wall surface to obtain a favorable mesh density for the wall treatment. The fluid volume mesh and the global coordinate system are presented in Figure 14. The dimensions in the figure refer to the portal frame dimensions. L is the width of the structure in the x-direction and H is the height of the portal frame in the z-direction.

The Trimmed mesher created the core volume mesh composed of hexahedral cells, the size of which was defined by a base value. A template of hexahedral cells was generated and then cut using the surfaces that limit the fluid domain. [22] Additional refined trimmed mesh sections were created at the wake of the cylinder and both pillars. Refinement zones are visible in Figure 14 and detailed views are presented in Figure 16 for the final mesh configuration.

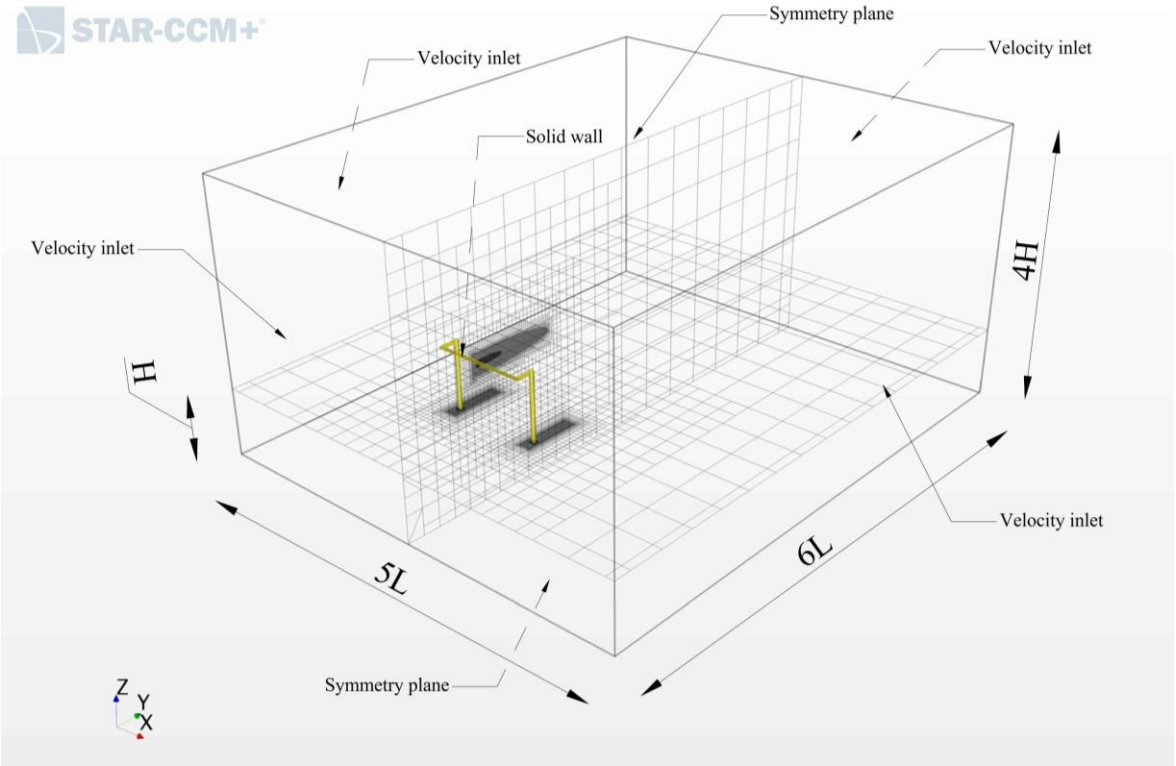

Figure 14. CFD simulation domain and the used boundary conditions.

At the solid wall surfaces, a more refined cell size is required for the wall treatment as discussed in Section 3.1.1. This was achieved using Prism Layer mesher which creates a desired number of prismatic cell layers along the no-slip solid surfaces [22]. Prismatic layer is generated defining its total thickness, the number of layers and the geometric progression factor. The inner most prismatic cells are the smallest and the geometric progression defines the size of the next cell through a factor of constant stretching.

The boundary conditions applied on the CFD domain are presented in Figure 14. The inlet surface, outlet surface and both domain box side surfaces were defined as velocity inlet surfaces, i.e., the velocity on the surface was a vector equal to U**j**. The top and bottom surfaces of the domain were considered sufficiently far from the portal frame structure and thus they were set as symmetry planes. The portal frame surface was a no-slip wall surface which means that the velocity on the wall surface relative to the wall was zero. In the case of one-way coupled FSI and pure CFD simulations this meant that the velocity on the wall surface was zero. However, in the two-way coupled FSI simulations the fluid velocity on the portal frame surface was equal to the velocity of the portal frame surface.

During the initial simulation runs it was discovered that the force components were mesh dependent. Both the magnitude and the frequency of the lift force varied depending on the mesh density as did the magnitude of the drag force. Therefore, it was necessary to conduct

a mesh convergence study on the CFD mesh to verify the accuracy of the final mesh configuration before the FSI simulations. The total drag force and the lift force on the portal frame due to pressure were selected as the studied variables. The force root mean square (rms) amplitude was selected as the monitored value because it can take into account the contribution of both negative and positive force values. Additionally, power spectral density (PSD) was used to obtain the frequency response of the lift force. The convergence study was conducted using three different mesh densities: a coarse mesh, a medium mesh and a fine mesh. The average solver time for a single time step during the simulation was recorded to indicate the computational cost of each mesh density.

The physical simulation time in the grid convergence study was 5.0 s. Comparison results were obtained from 3.0 s to 5.0 s. The first three seconds were required for the solution residuals, namely velocity, pressure, turbulent kinetic energy and specific dissipation rate to properly converge in all mesh configurations. Results of the grid convergence study are presented in Table 6. The lift force frequency response spectrum is presented in Figure 15.

Table 6. Grid convergence study results.

Parameter	Coarse Mesh	Medium Mesh	Fine Mesh
Total cell count	3.23 x10^6	4.70 x10^6	6.62 x10^6
Solver time/Δt	29.7 s	47.8 s	65.7 s
$Lift_{rms}$	31.2 N	49.0 N	53.6 N
f_{lift}	17.5 Hz	15.5 Hz	14.5 Hz
$Drag_{rms}$	551.1 N	688.7 N	779.0 N

More mesh sizes with total cell counts ranging from 6.6 M to 10 M and above could be studied in the future to minimize the uncertainties related to the upward convergence. This is, however, computationally unfeasible in the scope of this thesis. The following conclusions are made considering the above.

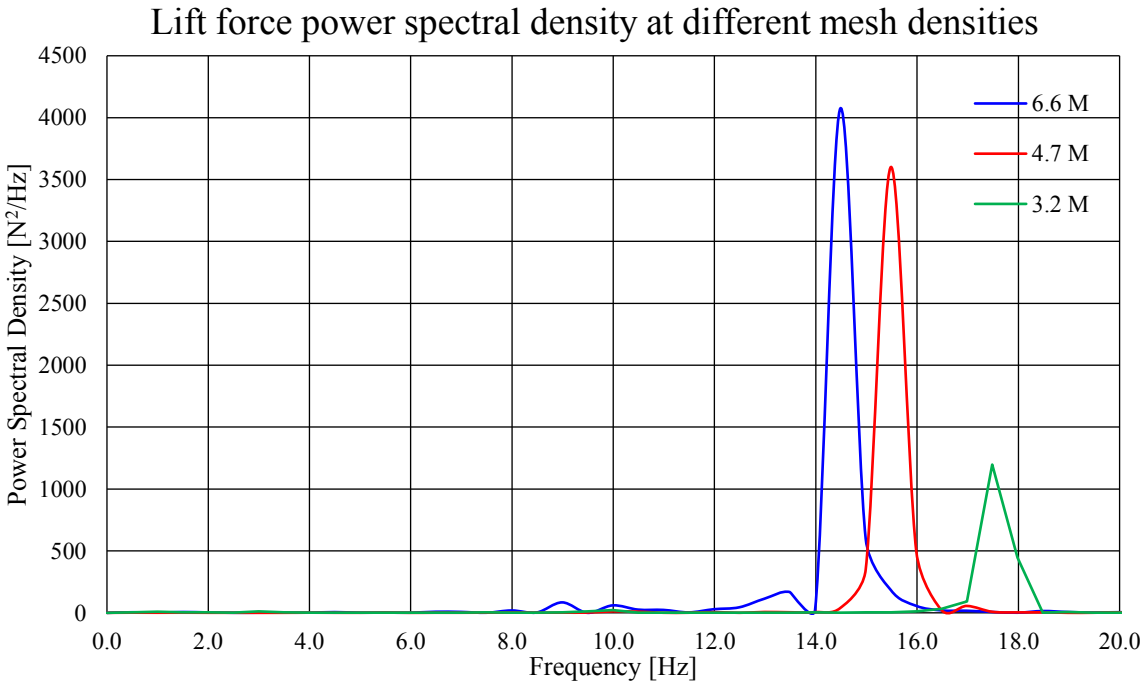

Figure 15. Lift force power spectral density at different mesh densities

Based on the grid convergence study, the coarse mesh is unable to capture the physical behavior of the flow. This mesh density does not capture the energy content of the oscillating lift force as evident in Figure 15. The force amplitude ranges are also well below those simulated with the denser meshes. Starting from the medium mesh, the lift force rms amplitude seems to converge to a value around 50 N. As seen in Figure 15, the frequency peak exhibits converging behavior. The peak value seems to increase with the increasing mesh density and the frequency starts to converge toward the analytical estimate of 13.8 Hz. Too coarse mesh in the cylinder wake seems to numerically dissipate the vortices which leads to both a higher frequency oscillation as well as lower energy content in the vortices. The higher frequency compared to the initial estimate may partially be due to the numerical part including the box beam sections as the analytical method is aimed for a uniform cylinder. The frequency peak estimated by the fine mesh is closest to the initial estimate. The medium mesh is unable to fully capture the amplitude of the drag force which seems be somewhere above 770 N. This value was predicted by the fine mesh. The fine mesh was chosen for the final FSI simulations as it appears to most accurately capture the physical force behavior. Additionally, this mesh configuration should lead to the highest response due to the largest force amplitudes and the vortex-shedding frequency closest to the portal frame's natural frequency. The computational cost of using higher mesh densities would be unfeasible, especially for the two-way coupled FSI.

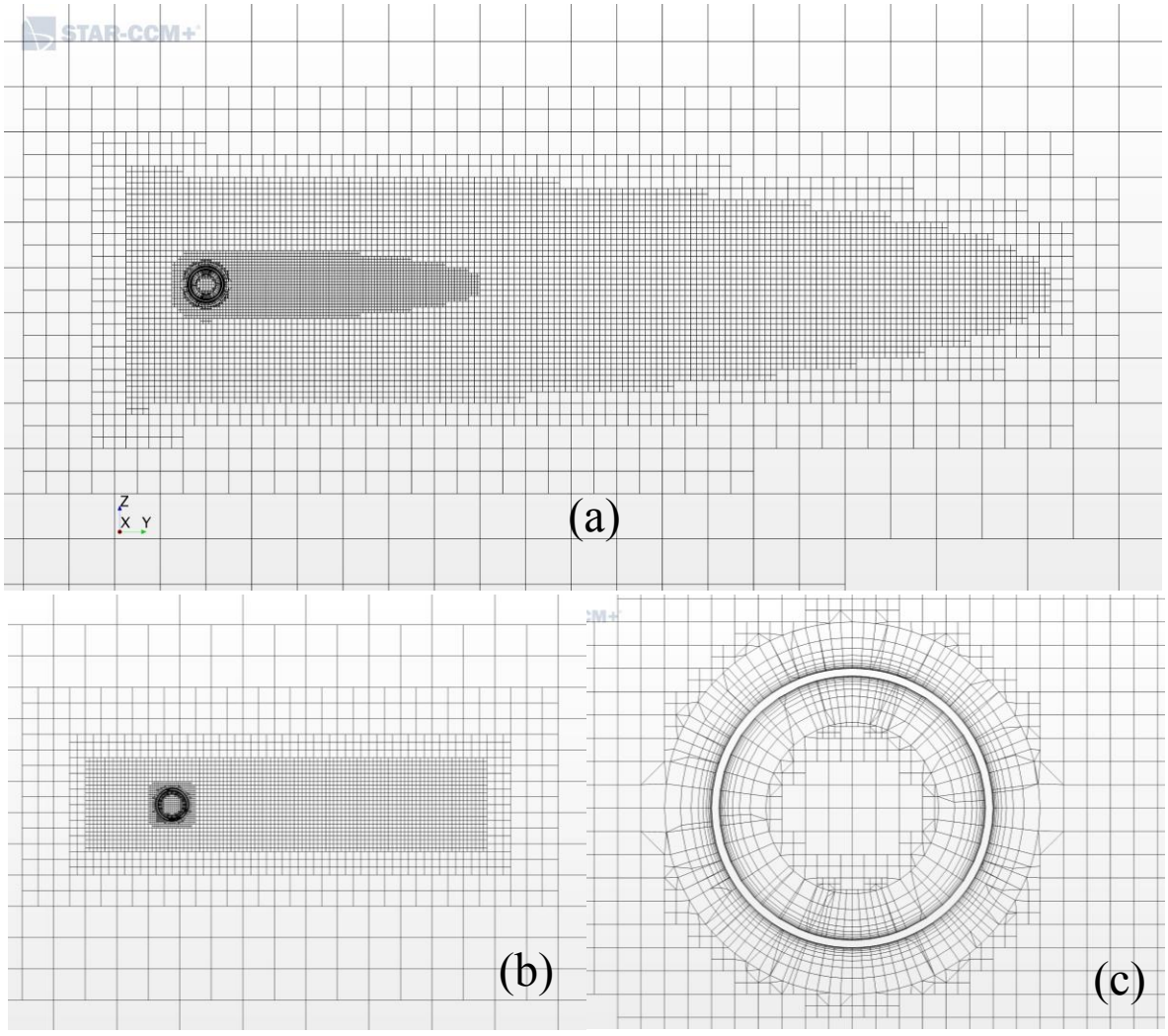

Figure 16. Detailed views of the refinement zones in the CFD mesh.

The same CFD mesh was used to obtain the force results for the quasi-static and quasi-dynamic cases as well to compute the one- and two-way coupled FSI simulations. Therefore, possible discrepancies between the numerical flow field and the physical reality do not affect the final result comparison. The results can be used to determine the differences between different modelling approaches in a way that the objective of the thesis is satisfied.

In the final mesh configuration the Trimmed mesher used a base value of 0.8 m. This base value resulted in a favorable mesh topology considering the complete numerical domain. The largest cells on the outer surfaces and in the outlet region had a base size of 3.2 m. Both the pillar and the larger wake refinement regions used a base cell size of 50 mm. The smaller wake refinement region in the cylinder wake used a base size of 25 mm. A layer of ten prismatic cells was generated at the portal frame surface. The stretch factor was 1.5 and the total thickness of the prismatic layer 50 mm. The resulting smallest cell height was 0.44 mm and the largest prismatic cell had a height of 17.0 mm. Two intermediately sized cells were generated at the section transition zones where the base cell size changed. Detailed views of the cylinder wake and the pillar wake refinement zones as well as the prismatic layer on the cylinder surface are presented in Figure 16 (a), (b) and (c), respectively.

4.4 FEA model

This section is dedicated to describing the finite element model constructed in STAR-CCM+ and used for the coupled FSI simulations. The emphasis is on the finite element mesh and the boundary conditions. Additionally, the structural dynamics solvers are summarized.

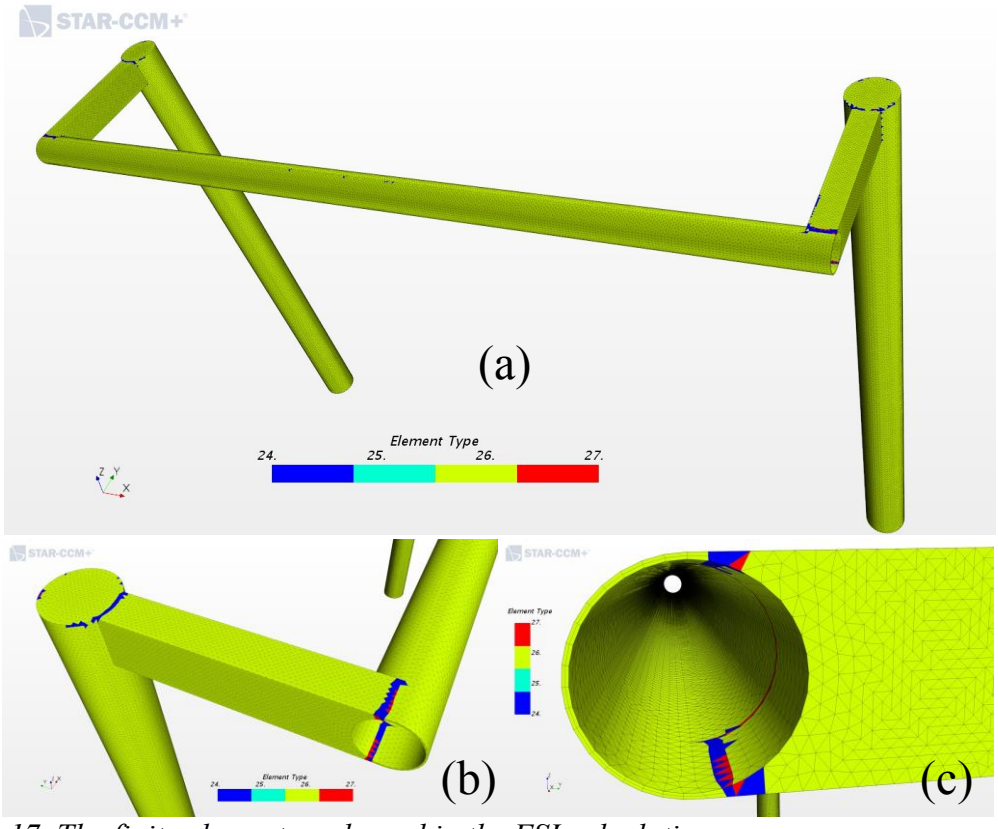

Figure 17. The finite element mesh used in the FSI calculations.

The finite element mesh is shown in Figure 17 where the element types are indicated with the type indicator numbers. Number 24 indicates 10-noded tetrahedral, 26 15-noded wedge,

and 27 13-noded prismatic elements. The solid domain was discretized using fully three-dimensional solid elements. The typical element, shown in Figure 18, has a wedge geometry that may be applied for thin walled structures [22]. Hexahedral elements would be preferable [22], however, these were not available using automatic meshing. The FEA mesh was created in STAR-CCM+ using an automatic Tetrahedral mesher together with a Thin mesher [22]. The STAR-CCM+ manual [22] suggests using at least two elements in the bending direction. Therefore, two layers of thin wedges were created in the thickness direction of the portal frame parts, as visible in Figure 17 (c) on the cylinder end surface. Prismatic or tetrahedral cells may be generated by the automatic mesher at regions where the thickness or the geometry varies considerably. This is visible in Figure 17 (b) and (c) where the prismatic and tetrahedral elements are shown located primarily in the sharp pillar corners and the connections of the box beams and the cylinder. The base element size was set to 25 mm. This resulted in a FEA mesh that based on the engineering judgement was considered to give a good idealization of the structural dynamics. Quadratic solid elements were used to avoid numerical locking [22]. The resulting solid finite element mesh contained 233,778 cells comprised of 228,814 wedge elements, 3,388 tetrahedral elements and 1,576 prismatic elements.

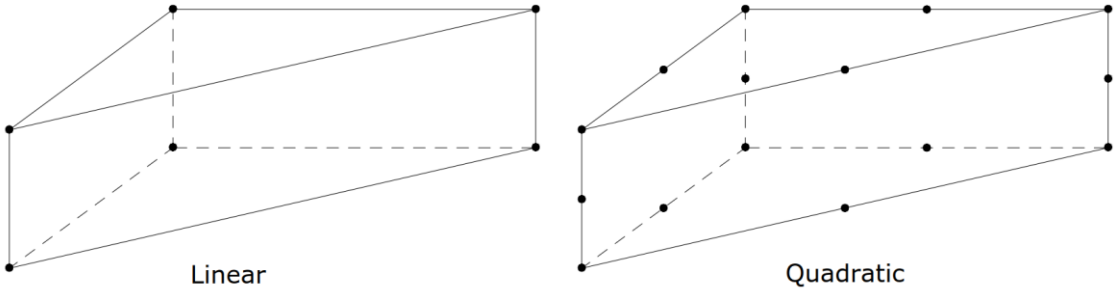

Figure 18. Three-dimensional solid wedge element geometry. Linear element shown on the left and quadratic element with the additional mid-side vertices on the right. Nodes are highlighted with black dots.

The finite element model of the portal frame was constrained at the lower ends of the pillars. All degrees of freedom were fixed at the two pillar end surfaces. This corresponds to the same boundary condition as applied in Femap in the dry analysis phase.

In addition to the mesh, the finite element model is described by the discretization schemes and solvers used to compute the numerical solution. The numerical methods have been discussed in detail in Sections 3.2.1 and 3.2.2. Therefore, the used approaches are simply presented in Table 7. Structural dynamics were solved using the same time step of 0.002 s as in the CFD calculations.

Table 7. Numerical approaches applied in the finite element model during coupled FSI analysis.

Application	Model/Solver	Type
Solid domain	Linear elasticity	Quadratic 3D FE
Temporal domain	Newmark	2nd Order
Sparse direct matrix solver	MUMPS	-

4.5 Quasi-static reference model

To obtain the simplest and most conservative reference for the FSI simulation results, a simple beam model was created in Femap. The portal frame was discretized with linear beam elements and constrained at the pillar ends similarly to the above-mentioned FEA model. A quasi-static approach was employed, i.e., the inertial effects were assumed negligible and only the stiffness of the structure affected the response. Therefore, the problem was reduced to a constant force due to drag and lift being exerted on the portal frame in static equilibrium. The finite element beam model is shown in Figure 19. The pillar sections were discretized with 12 elements, box beam sections with 3 elements and the cylinder section with 16 elements. The eigenmodes of the beam model were analyzed using the same modal analysis solver as for the plate model. The results are presented in the Appendix 1.

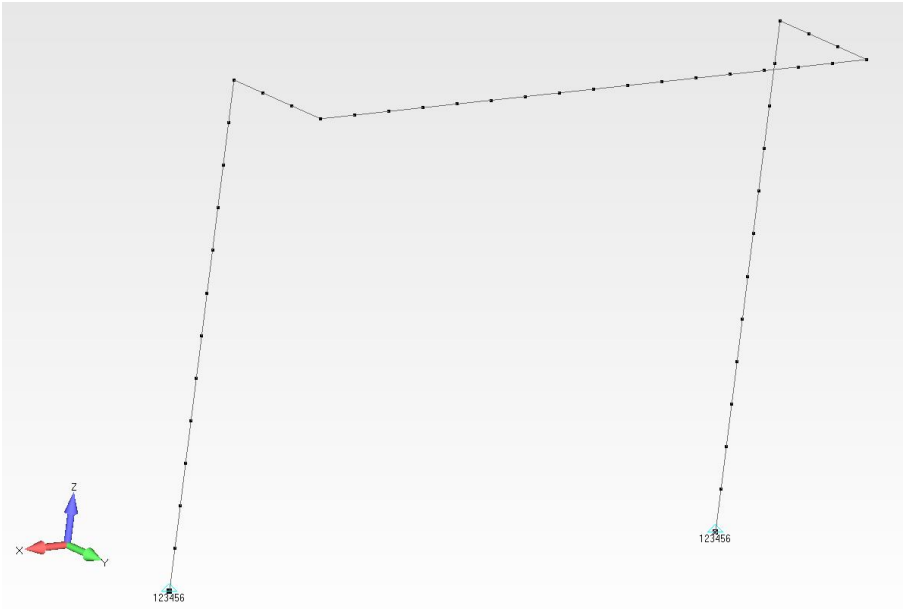

Figure 19. Finite element beam model. Element vertices are illustrated with black dots.

Loading for the quasi-static modelling was obtained using the same CFD model as in the FSI calculations. The time histories of drag and lift forces from the one-way coupled FSI simulation were used. These correspond to the values calculated with pure CFD since the structural deformation did not affect the fluid domain. The model was divided into two regions for which the lift and drag forces were obtained. Cylinder and both box beams were considered as one part. The two pillars were considered as the second part, but the forces were applied separately on each pillar. Only the force contribution due to the aerodynamic pressure was considered and thus the total lift force corresponded to the lift force on the cylinder section. The maximum total drag force was divided between the cylinder and pillar sections based on the projected frontal areas. The peak maximum and minimum of the lift force and the maximum drag force values were used as the worst-case scenario loading conditions in the quasi-static analysis. The obtained forces were applied as point loads at the respective part's midspan which was considered the worst loading condition. The loading condition was simplified assuming that CF forces on the pillar sections were negligible and thus only the drag force on the pillars was considered. The peak force values obtained from the one-way coupled FSI calculations are presented in Table 8.

4.6 Quasi-dynamic reference model

The second set of reference results was obtained utilizing the same finite element beam model as for the quasi-static case. Instead of point loads line loads were applied. The analysis was conducted using the direct transient response finite element solver SOL 109 in NX Nastran [43]. All damping was neglected in the transient analysis. The model was first loaded only with the gravity induced load from 0.0 to 1.0 seconds after which the drag and lift forces were applied until the total end time of 11.0 s. The results of the final ten seconds were used in the final comparison. The time step was equal to that in the FSI simulations, i.e., $\Delta t = 0.002$ s.

Based on the drag force time histories and their frequency spectra, the drag forces may be assumed constant similarly to the quasi-static case. Therefore, the maximum drag force value in Table 8 was used as equally distributed line loads, divided similarly as in the quasi-static case between the cylinder and pillar sections. The cylinder lift force due to the pressure load was extracted from the one-way coupled FSI simulation as a single time history signal. A line load was obtained assuming the lift force to be equally divided along the cylinder span. The force signal was applied in the quasi-dynamic model divided by the length of the cylinder beam. The recorded total lift force from the one-way coupled simulation is presented in Figure 22.

5 Results

This chapter is dedicated to presenting the numerical results obtained in the case study. The results are discussed separately in Chapter 6. Results are divided into four sections. First, the numerically simulated flow field is illustrated. The focus is on visual observation. The second section presents the dynamic wind loading experienced by the portal frame. Third, the displacement results are introduced. For this purpose, values at the center point on the top surface of the cylinder and at the pillar upper end surface are used. In the fourth section, the stress values are presented. Due to the wind-induced vortex shedding the portal frame is subjected to multiaxial dynamic loading. This excites the portal frame structure's antisymmetric eigenmodes that combine bending and torsion. Therefore, von Mises stress has been chosen as the compared stress value since it may be used for ductile material to evaluate the combined stress state [48]. Power spectral density has been used to evaluate the frequency responses of the monitored time history values.

The FSI simulations were computed for a total physical time of 13.0 s. Similar to the grid convergence study, the first 3.0 s were initialized with only the fluid domain solvers active. This allowed the flow field residuals to converge sufficiently before activating the Solid Stress and FSI coupling solvers. The results are presented for the final 10.0 s of the simulations. For clarity, the four different models are termed Models I, II, III and IV in the order of increasing complexity, i.e., quasi-static, quasi-dynamic, one-way coupled FSI and two-way coupled FSI, respectively.

5.1 Numerical flow field

Vortex shedding behind the horizontal cylinder is shown in Figure 20 using streamlines colored with the velocity magnitude at the cylinder midspan cross-section plane. The subfigures are ordered according to the propagation of time. The vortex is first seen rolling at the bottom surface of the cylinder in Figure 20 (a). As the vortex grows going from Figure 20 (b) to (c), the second vortex starts to reach its maximum size. In Figure 20 (d) the top vortex is starting to grow as the maximum vortex size at the bottom is reached. This cycle continues with the top vortex growing and the bottom vortex being transported along the wake. This oscillating vortex cycle continues as the simulation time propagates.

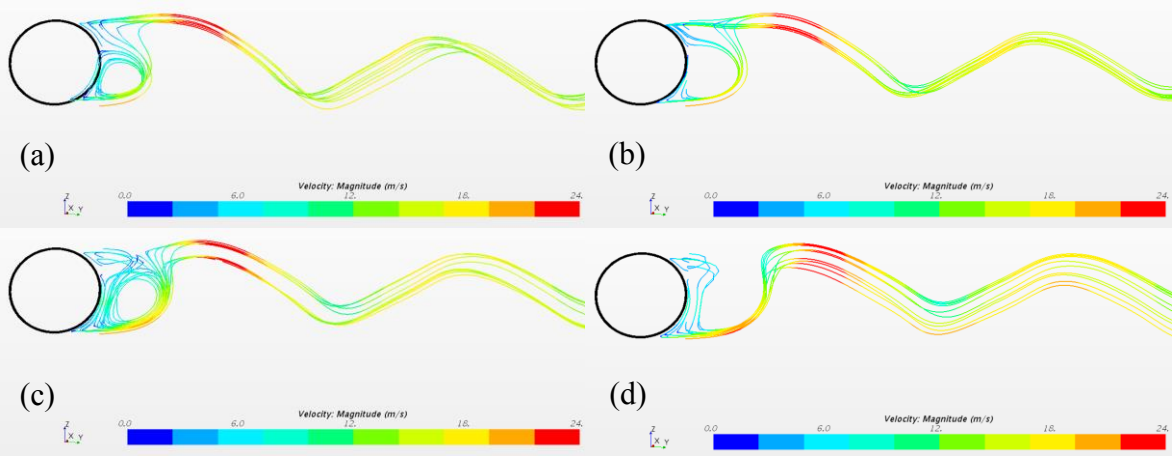

Figure 20. Streamlines colored with the velocity magnitude behind the cylinder at the midspan cross-section. Taken from Model III.

Fully three-dimensional vortex street behind the portal frame is shown in Figure 21. Vortices are visualized using positive Q-criterion values [49]. Vortex shedding occurs behind both pillars and the cylinder section. The random nature of the phenomenon in the wake is visible as the vortices interact with each other. Vortex shedding occurs periodically but not in the same phase at each cross-section, i.e., similar cross-sections as in Figure 20 show vortices in a different phase of development at the same time instance. Randomness and vortex interaction seem to be more dominant in the cylinder wake. This is further emphasized by the smaller cell size in the cylinder wake refinement zone. Some numerical dissipation has been observed in the cells further in the wake where the cell size increases. The increase in cell size was necessary to reduce the computational cost of the simulation.

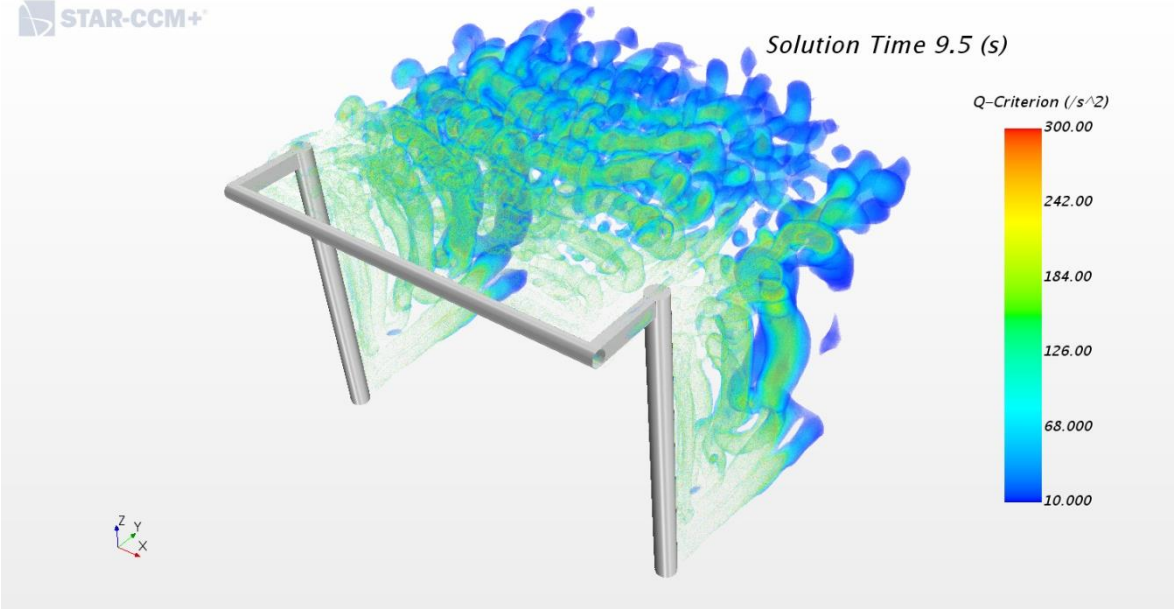

Figure 21. Turbulent vortices behind the portal frame visualized with Q-criterion. Taken from Model III.

5.2 Dynamic wind loading

The dynamic wind loading is described by the force components on the portal frame. Lift and drag forces due to pressure were monitored as the contribution of viscous shear forces in air was assumed negligible. The force frequency components were analyzed using the PSD of the time histories. The characteristic force values comprise of the rms value and the maximum and minimum values. These are presented in Table 8. Differences were calculated comparing the two-way coupled results to the values from the one-way coupled simulation.

Table 8. Characteristic force values in the FSI calculations.

Parameter	One-way	Two-way	Difference
$Lift_{rms}$	55.8	88.2	58 %
$Lift_{max}$	113.7	218.4	92 %
$Lift_{min}$	-124.9	-251.2	101 %
$Drag_{rms}$	778.6	782.7	1 %
$Drag_{max}$	799.1	857.5	7 %
$Drag_{min}$	757.0	720.1	-5 %

The lift force time history simulated using the one-way coupled FSI analysis is presented in Figure 22. The equivalent graph of the two-way coupled Model IV is shown in Figure 23. The maximum absolute lift force value occurs in both simulations in the downward direction. Due to the combined effect of gravitation this is the worst-case loading direction. In Model III the largest instantaneous lift force of -124.9 N occurs at the time instance of 12.87 s. In Model IV the absolute maximum of -251.2 N is experienced at 12.616 s. The time history of the two-way coupled simulation exhibits clearly sinusoidal oscillations. In the one-way coupled simulation the lift force oscillates more uniformly around the mean value.

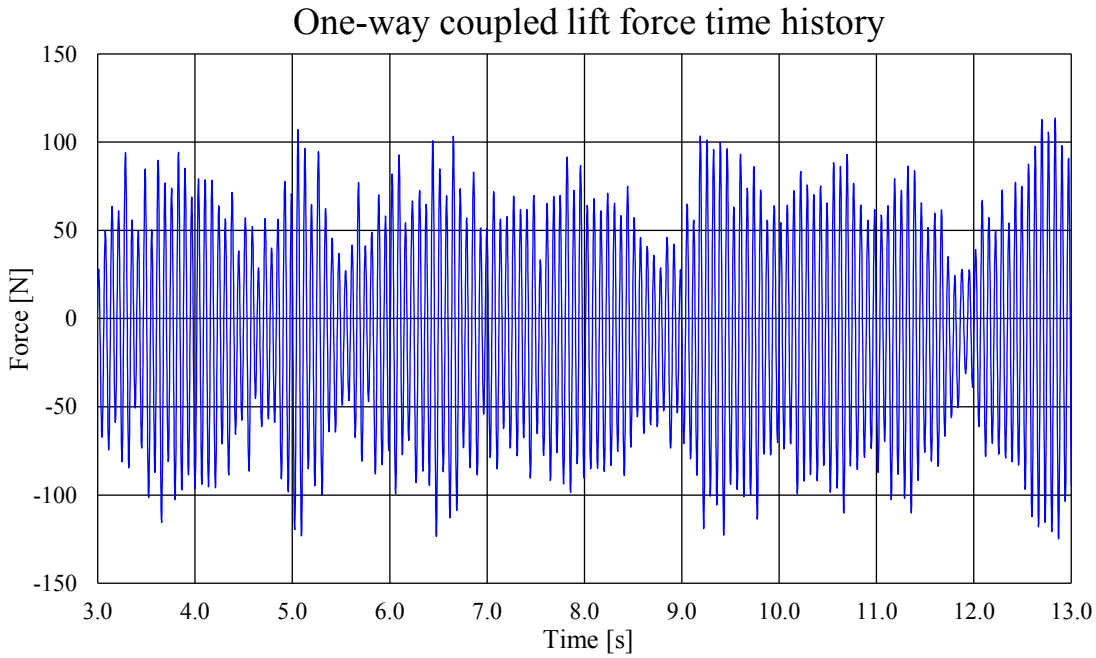

Figure 22. The total lift force due to pressure on the portal frame simulated with the one-way coupled FSI model.

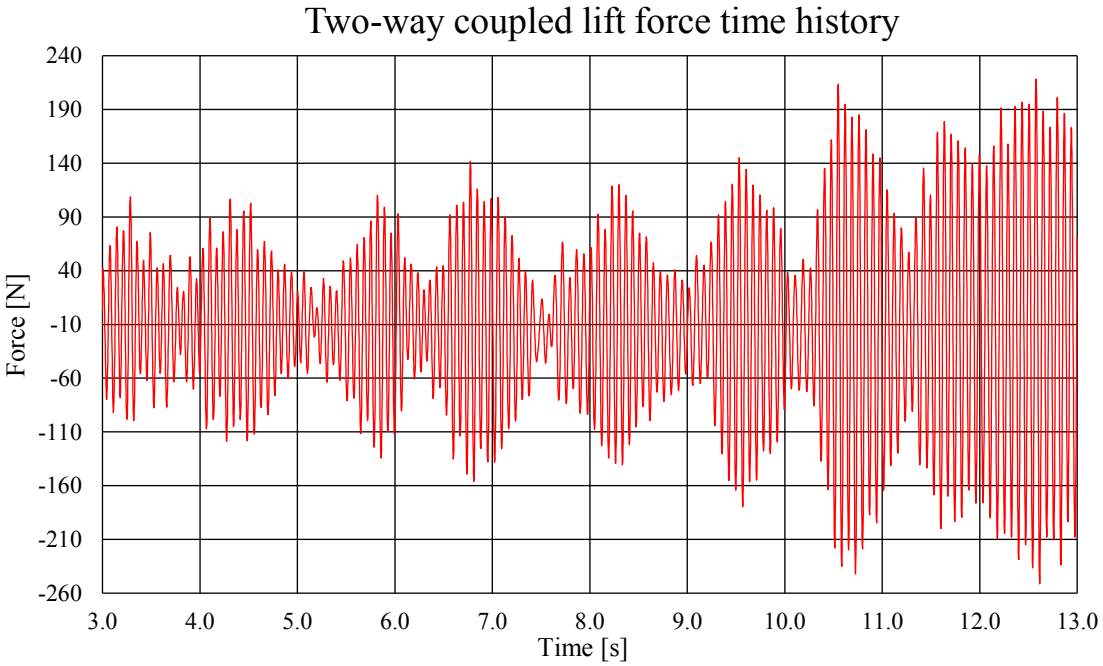

Figure 23. The total lift force due to pressure on the portal frame simulated with the two-way coupled FSI model.

The total drag force time histories are presented in Figure 24 for Models III and IV. The maximum drag force in the one-way coupled simulation is 799.1 N and it occurs at 8.854 s. In the two-way coupled simulation the maximum drag force of 857.5 N occurs at 12.986 s. The drag force oscillates within a constant peak value range in the one-way coupled simulation. However, in Model IV the amplitude range grows pronouncedly toward the end of the simulation.

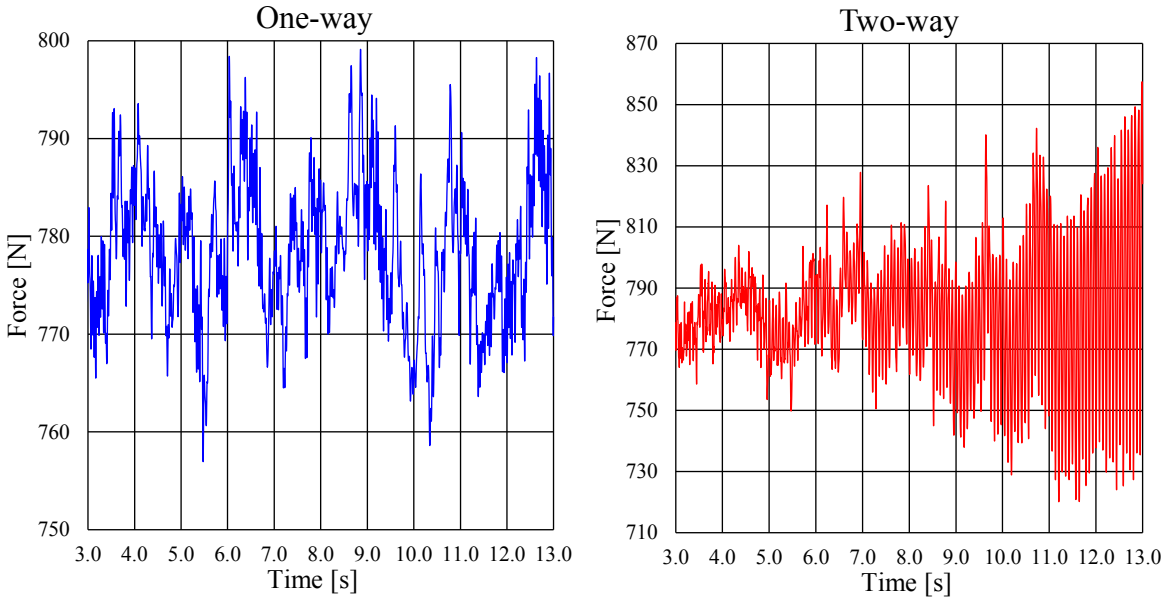

Figure 24. Total drag force on the portal frame structure.

The power spectral densities of the lift and drag force time histories are presented in Figure 25 and Figure 26, respectively. The lift force PSD has a single narrow-banded peak at 14.5 Hz in Model III, whereas in Model IV the PSD has two narrow peaks at 13.8 Hz and 14.5 Hz. The magnitude of the 13.8 Hz peak is considerably higher than that of the second peak at 14.5 Hz which is close to equal in magnitude to the peak of Model III. The PSD of the drag force does not exhibit a clear narrow-banded response in the one-way coupled results. The two-way coupled PSD spectrum has a single narrow-banded peak at 13.8 Hz but also includes the small, low frequency components which are present in the Model III.

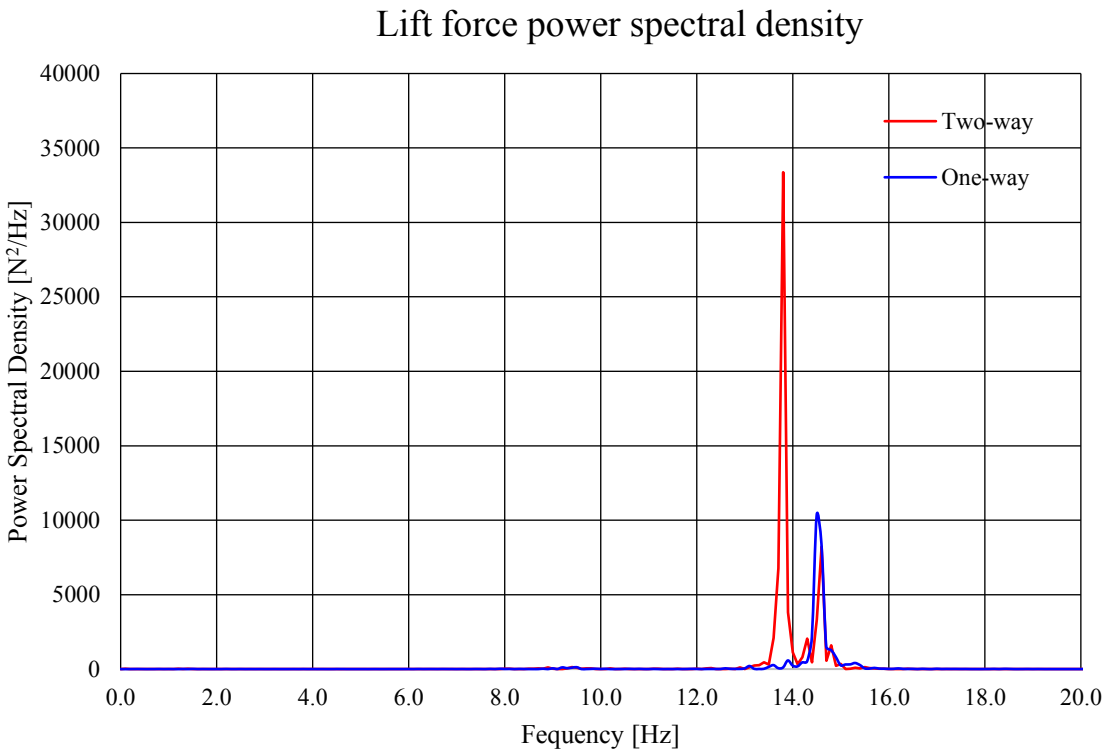

Figure 25. Power spectral density of the total lift force on the portal frame in the coupled FSI simulations.

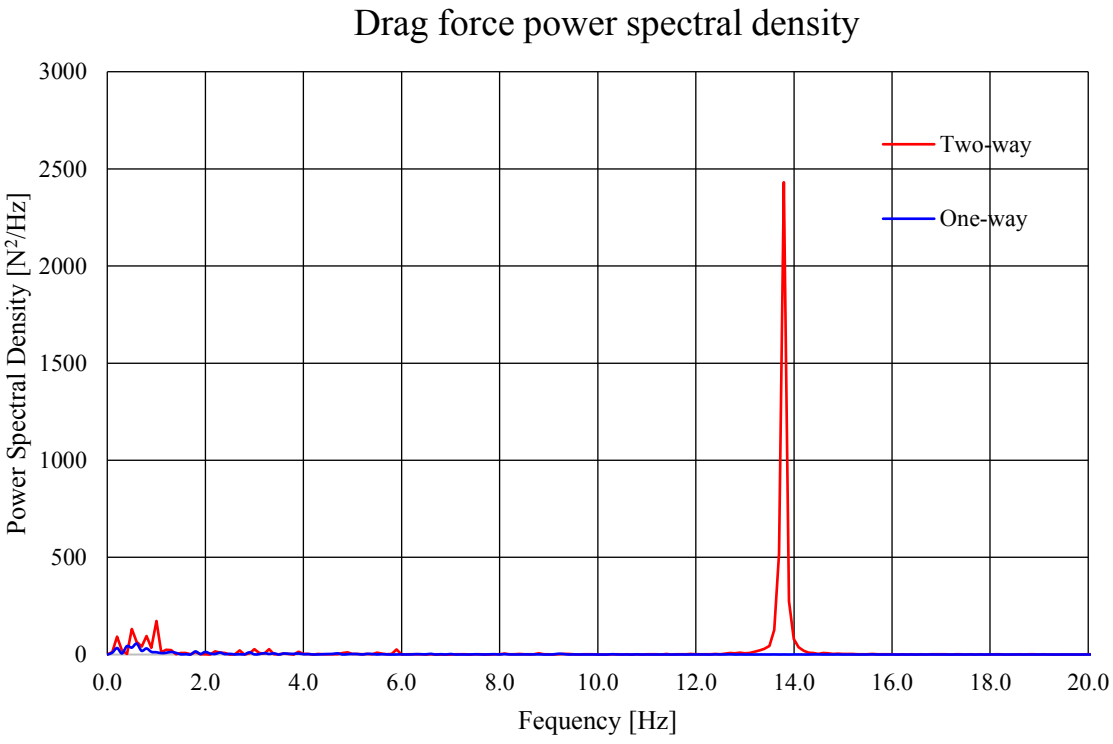

Figure 26. Power spectral density of the total drag force on the portal frame in the coupled FSI simulations.

5.3 Displacements

The deformation behavior of the portal frame may be described by monitoring the displacement behavior of selected points. The midspan point on the cylinder section top surface, referred to as the center point, was chosen to describe the deformations of the cylinder as this is the location where the maximum displacements were expected. Similarly, the maximum displacements in the pillars were expected at the upper end of the pillar. Therefore, another monitoring point was placed there. Displacements were monitored in the CF and IL directions of the respective parts. Ideally, the entire displacement history of all the finite element vertices would have been saved at each time step to capture the full deformation behavior accurately. However, this approach would have been both too memory intensive and computationally demanding that only two point monitors were used instead.

The center point displacement is divided into the in-line and cross-flow components, i.e., global y- and z-directions in the simulation domain shown in Figure 14. Displacement time histories are presented for Models II, III and IV. For Model I, the static values are presented. Pillar end point displacement values are also divided into CF and IL components. Pillar IL direction corresponds to the y-direction displacement and CF to the x-direction displacement. Non-dimensionalized displacement values are presented for the cylinder center point and pillar end point in Tables 9 and 10, respectively. The displacement values have been non-dimensionalized with the diameter the respective part.

Table 9. Cylinder center point displacement results of different models.

Model	I	II	III	IV
CF_{rms}/D	-	0.0074	0.0103	0.0249
CF_{max}/D	-0.0047	0.0094	0.0130	0.0638
CF_{min}/D	-0.0060	-0.0202	-0.0256	-0.0774
IL_{rms}/D	-	0.0025	0.0031	0.0065
IL_{max}/D	-0.0013	0.0039	0.0064	0.0174
IL_{min}/D	-0.0007	-0.0065	-0.0085	-0.0198

Table 10. Pillar end point displacement results of different models.

Model	I	II	III	IV
CF_{rms}/D	-	0.0	0.009	0.0016
CF_{max}/D	0.0	0.0	0.0027	0.0061
CF_{min}/D	0.0	0.0	-0.0028	-0.0046
IL_{rms}/D	-	0.0019	0.0017	0.0017
IL_{max}/D	-0.0011	0.0029	0.0014	0.0018
IL_{min}/D	-0.0015	-0.0049	-0.0038	-0.0043

Cylinder center point CF displacement is plotted in Figure 27 for all models. The maximum displacement in each of the models occurs in the downward direction. In the quasi-dynamic simulation the maximum displacement of -6.07 mm is experienced at 10.804 s equivalent to 12.804 s in the FSI simulations. The maximum displacement of Model III is -7.69 mm and it occurs at 11.05 s. In Model IV the peak displacement of -23.22 mm is reached at 12.984

s. All displacement plots exhibit a sinusoidally oscillating behavior with a growing amplitude range. The two-way coupled plot exhibits exponential growth and does not show convergence of the amplitude range as present in the one-way coupled plot.

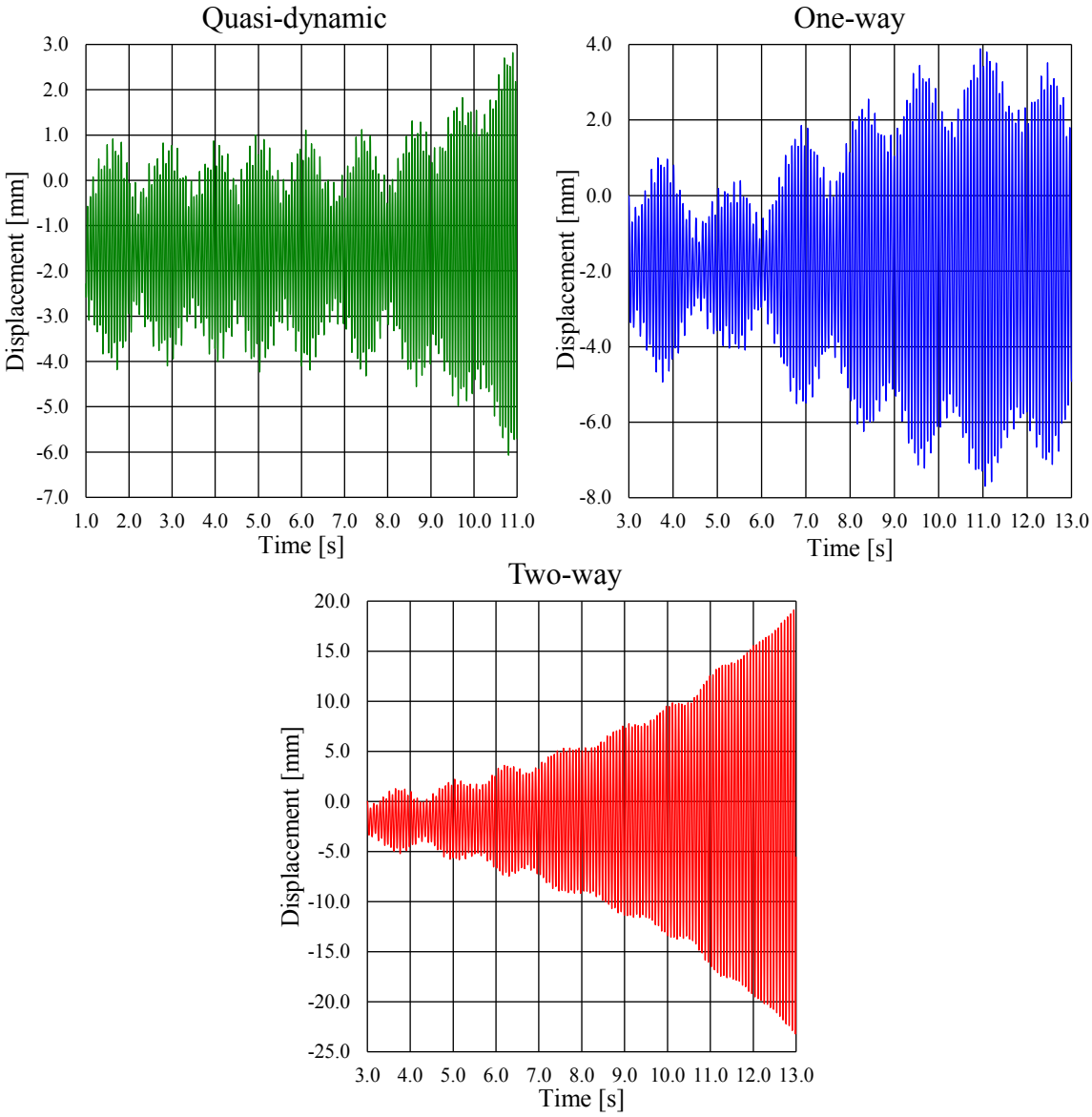

Figure 27. Cylinder center point CF displacement.

The IL displacement is presented for all models in Figure 28. The maximum IL displacements occurs in the opposite direction to the flow. For Model II, the maximum of -1.96 mm is reached at 10.968 s which is equivalent to 12.968 s in the FSI simulations. The maximum of Model III is -2.54 mm at 10.868 s. In Model IV the displacement peak of -5.95 mm occurs at 12.948 s. The IL displacement follows a similar trend as the CF displacement where the two-way coupling does not show convergence to a steady amplitude range.

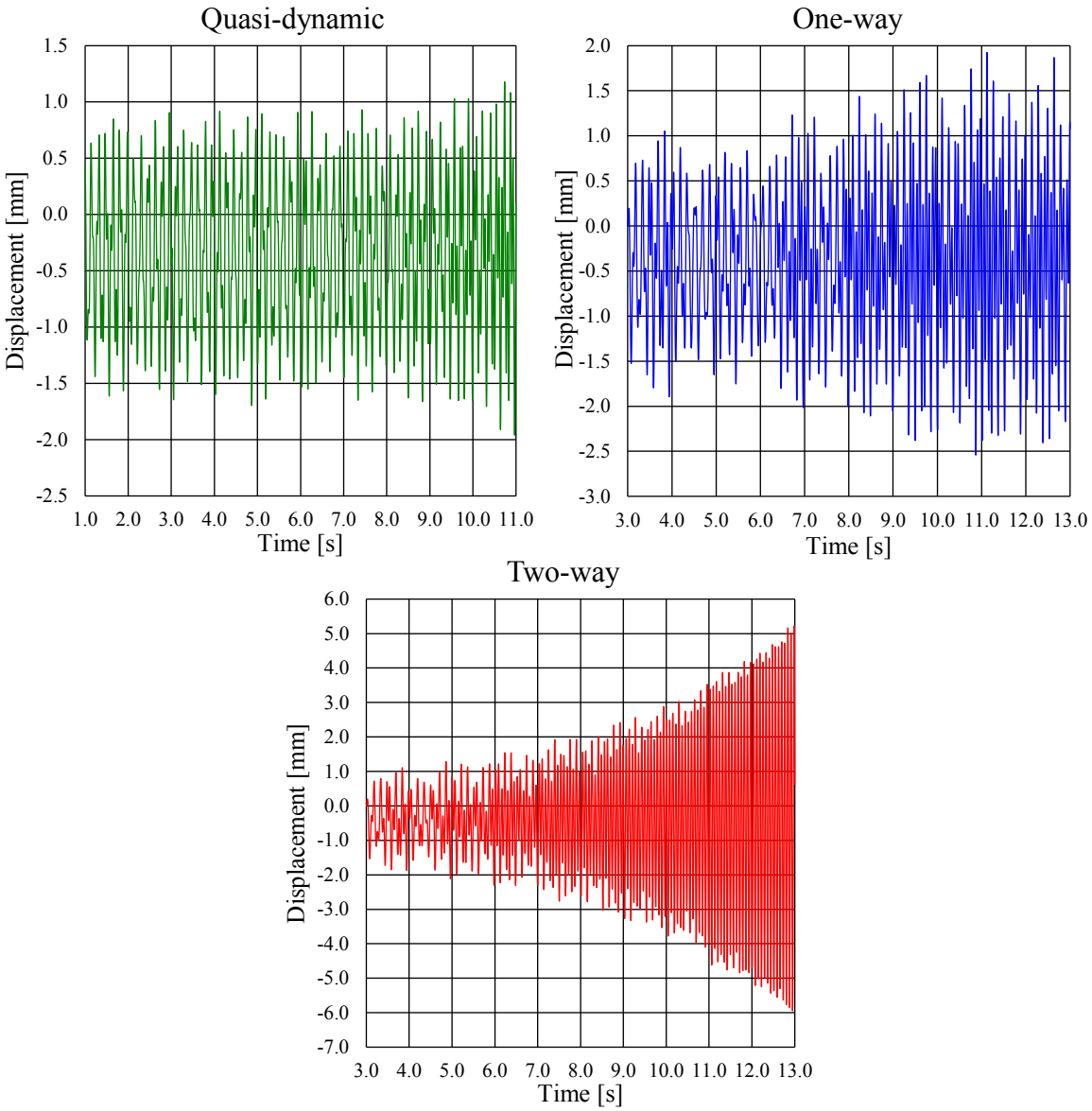

Figure 28. Cylinder center point IL displacement.

The frequency components of the portal frame's deformation behavior have been identified from the displacement time histories using the power spectral density of the transient data history. The cylinder CF and IL displacement power spectral densities are plotted for all models in Figure 29 and Figure 30, respectively. The PSD of the CF displacement has a single peak narrow-banded response where the peak is located at 13.8 Hz for Models III and IV and at 15.4 Hz for Model II. The peak in Model IV is considerably amplified compared to the other two simulations. The frequency response of the cylinder IL displacement has a twin-peaked form. In the Model III and IV results, the peaks are located at 6.8 Hz and 13.8 Hz whereas in Model II at 6.1 Hz and 15.4 Hz. Again, the peak amplitudes are larger in the two-way coupled simulation compared to one-way coupling.

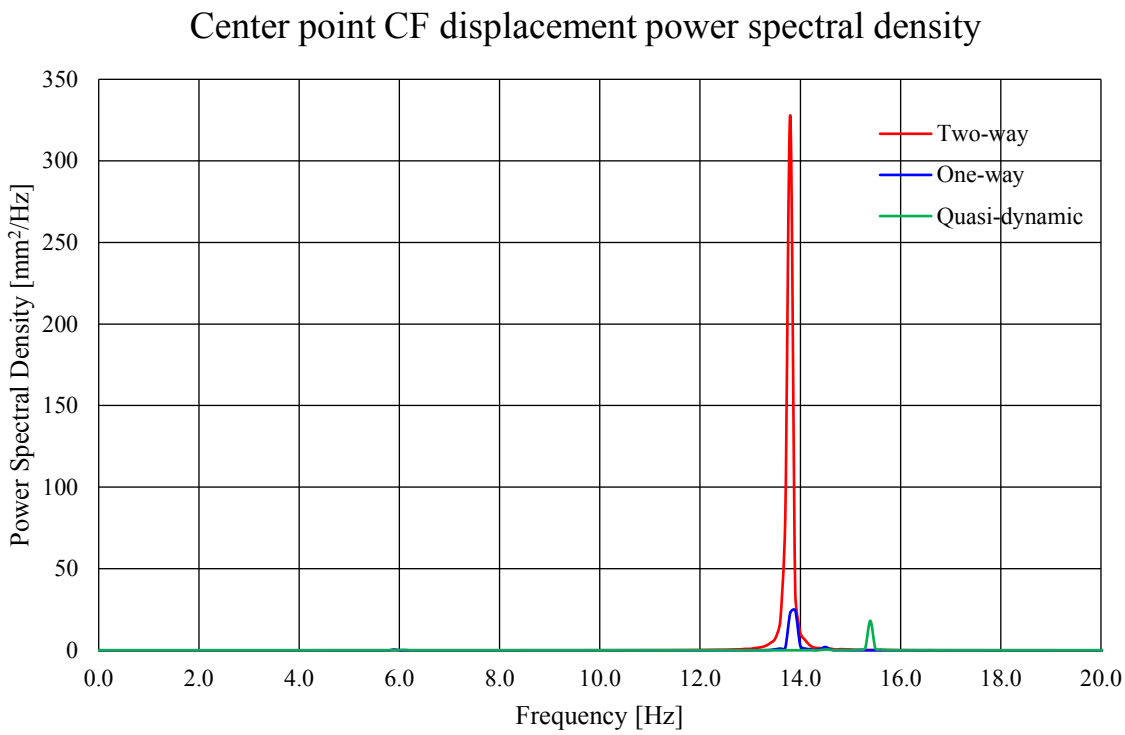

Figure 29. Power spectral density of center point CF displacement.

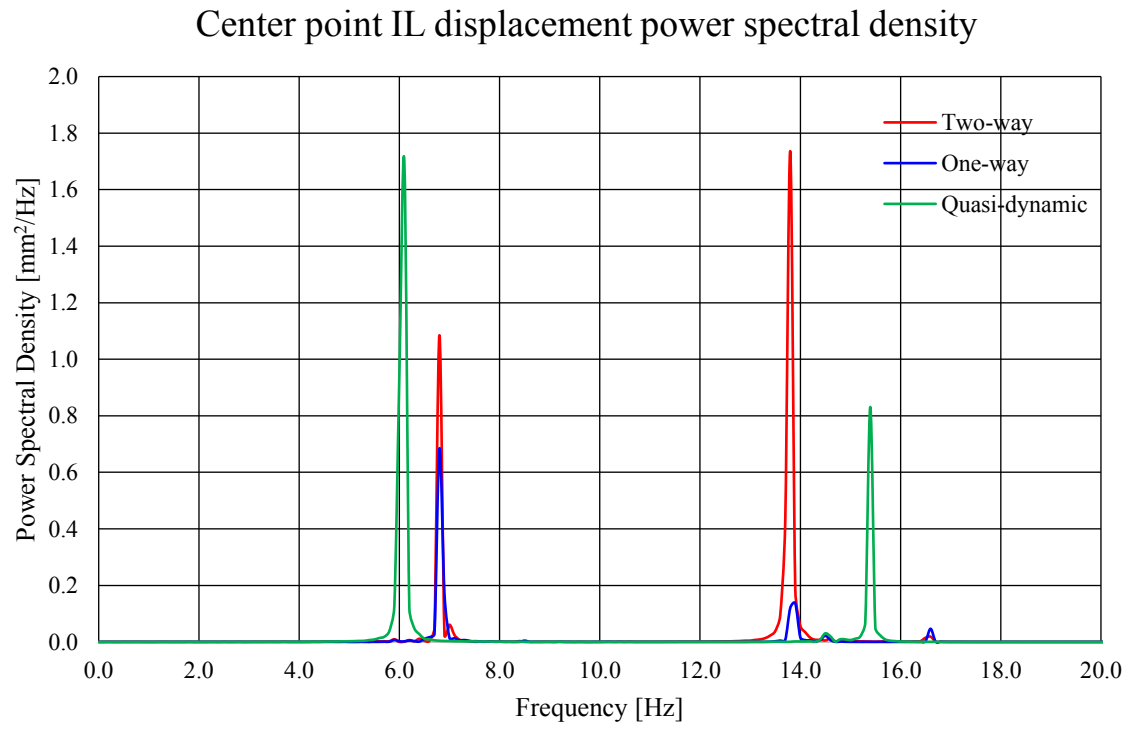

Figure 30. Power spectral density of center point IL displacement.

The pillar end point CF displacement time histories are presented in Figure 31 for Models III and IV. CF results from Model II have been omitted as the values are effectively zero. This is due to the x-directional forces being neglected in the quasi-dynamic analysis. In the Model III the absolute maximum displacement is -1.14 mm at 12.28 s whereas for Model IV the maximum is 2.44 mm at 12.874 s. The form of the two displacement plots is relatively similar, however, the two-way coupling exhibits a higher growing amplitude range.

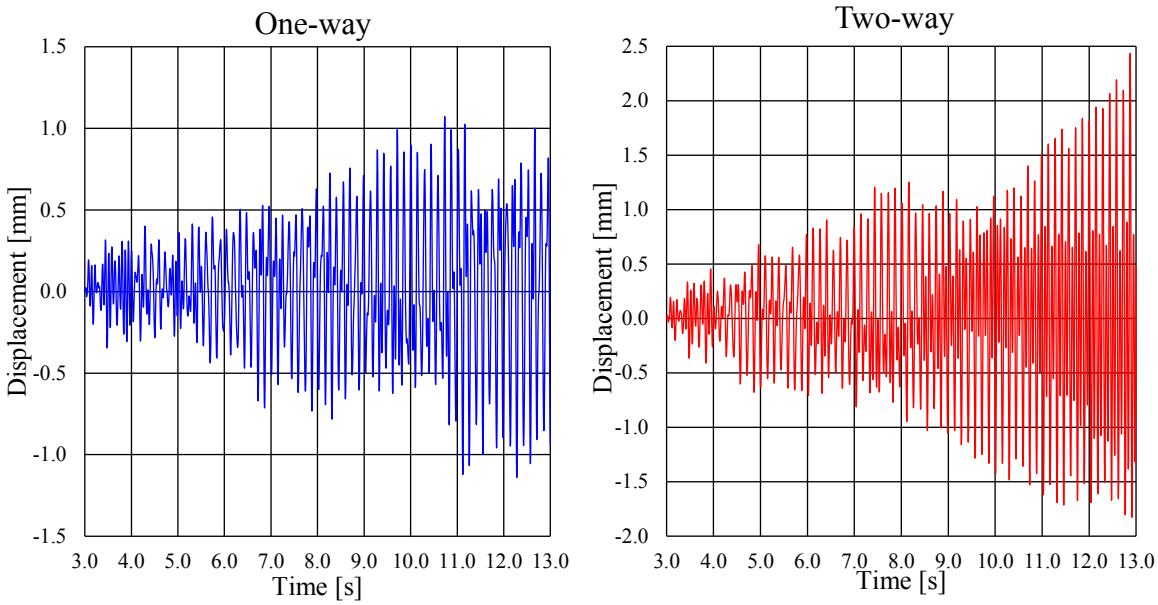

Figure 31. Pillar end point CF displacement.

The pillar IL displacements are illustrated for all the models in Figure 32. The IL displacement in Model II reaches the peak value of -1.96 mm at 10.968 s which corresponds to 12.968 s in the FSI simulations. In Model III the maximum is -1.54 mm which occurs at 12.39 s. The maximum for Model IV is -1.73 mm at 11.568 s. The IL displacement plots of Models II and III are in a constant amplitude range. Model IV displacement amplitude range starts increasing mildly toward the end of the simulation time.

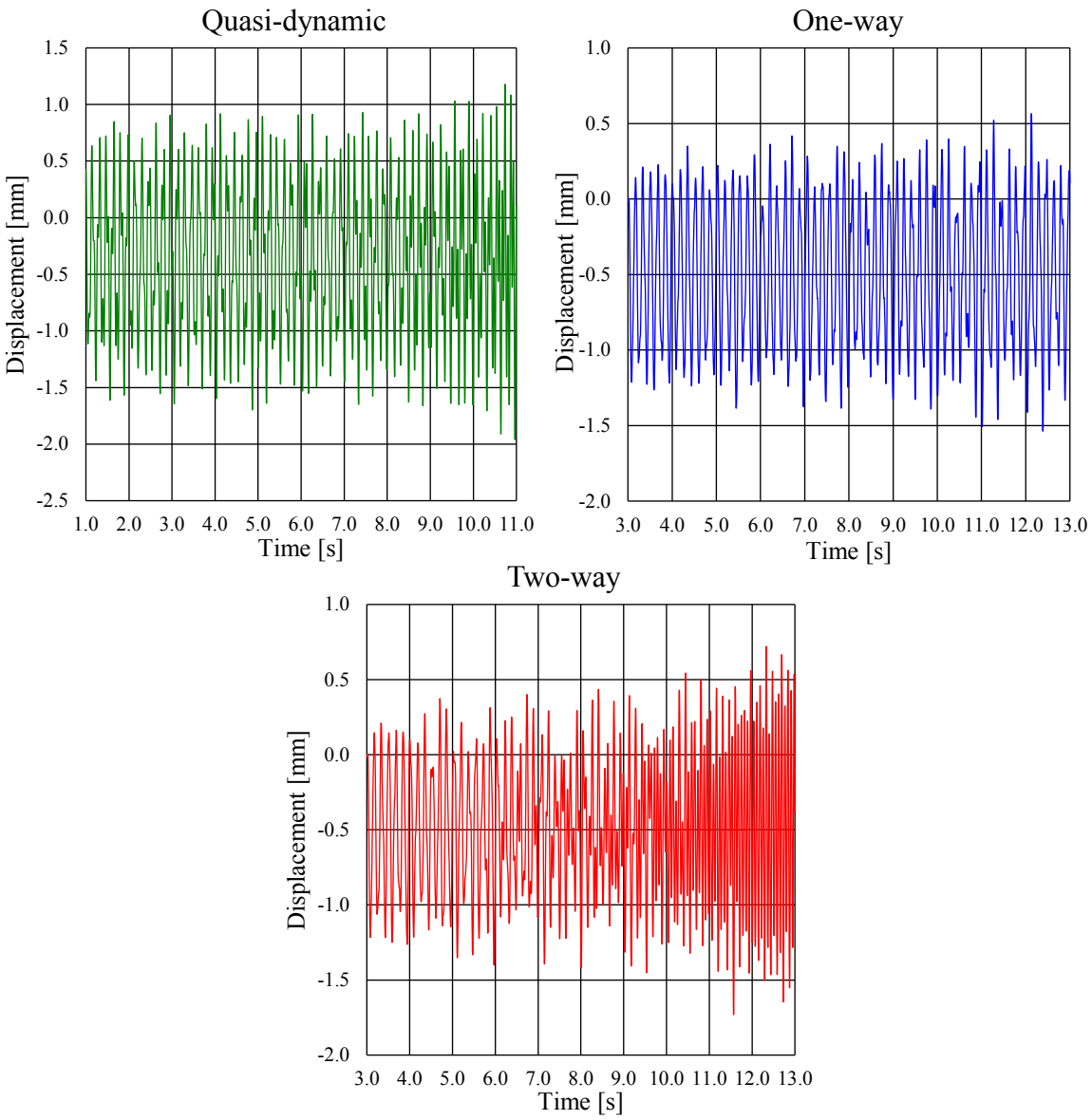

Figure 32. Pillar end point IL displacement.

The power spectral densities of the pillar CF and IL displacements are presented in Figures 33 and 34, respectively. The CF displacement PSD has a twin-peaked spectrum. The peaks are located at 6.8 Hz and 13.8 Hz. The peaks a considerably higher in the two-way coupled response. Additionally, the largest peak is shifted from 6.8 to 13.8 Hz going from Model III to Model IV. The PSD spectrum of the pillar IL displacement of the quasi-dynamic model exhibits two peaks at 6.1 Hz and 15.4 Hz. The one-way coupled PSD has a single major peak at 5.9 Hz. The two-way coupled result plot shows again two peaks which are located at 5.9 Hz and 13.8 Hz.

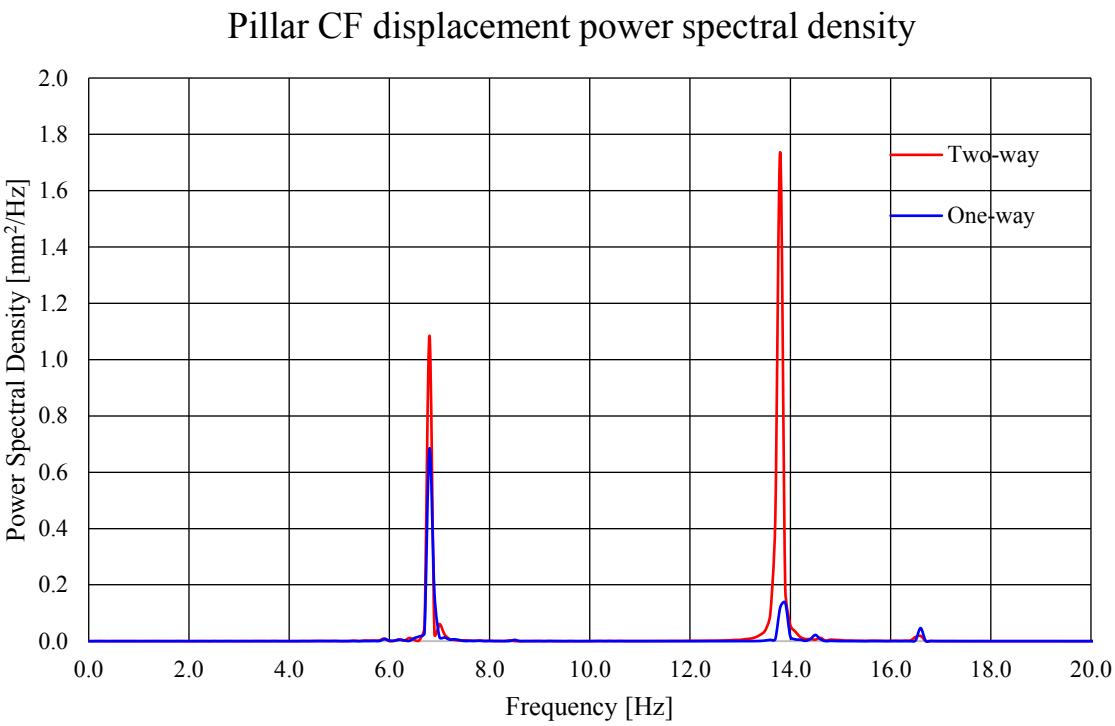

Figure 33. Pillar end point CF displacement power spectral density.

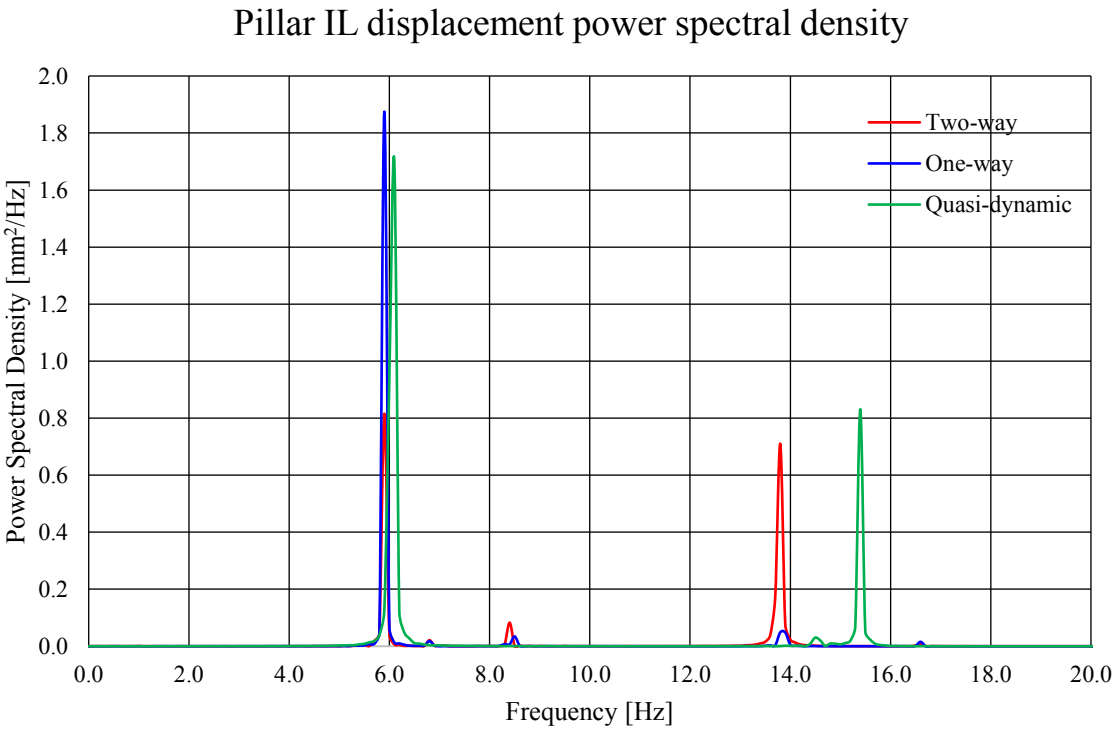

Figure 34. Pillar end point IL displacement power spectral density.

5.4 Stresses

To study the stresses in the portal frame structure, two characteristic locations have been examined. The first studied region is based on the structural engineering evaluation of the portal frame. It is the area around the maximum stress location. The second stress evaluation area is the cylinder midspan region. It is studied since it is the location of the maximum displacements in the portal frame and it has no local connections which would not be correctly modelled with the finite element beam model. Therefore, it serves as a good baseline for comparing the results of the different finite element approaches, i.e., beam and solid element models.

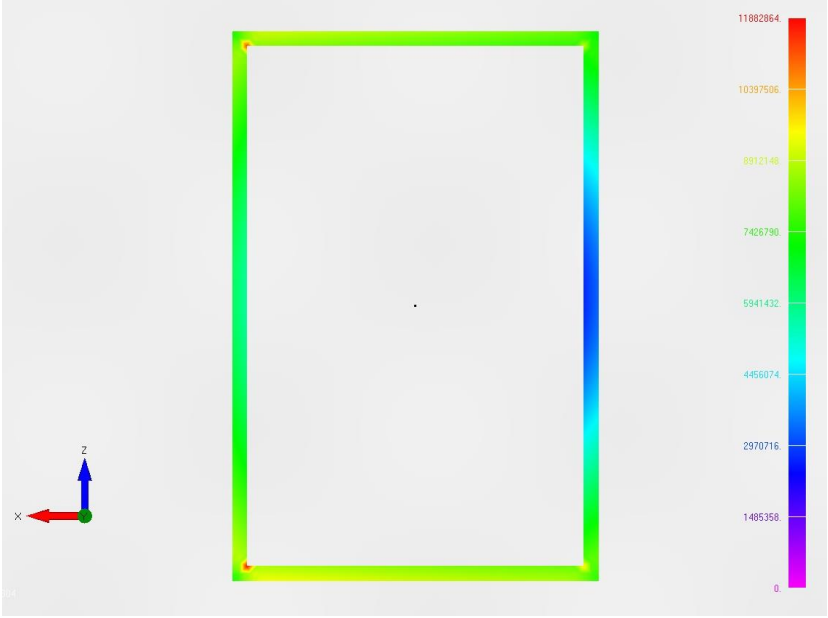

Figure 35. The maximum von Mises stress location in the quasi-dynamic beam model at the box beam's end cross section plane connected to the pillar section. Stress values are in Pa.

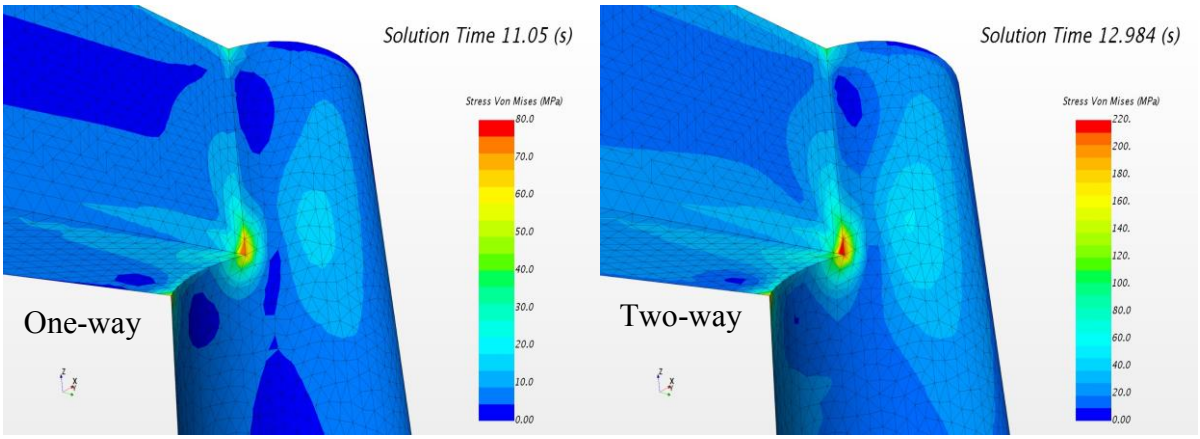

Figure 36. The location of the maximum von Mises stress in the coupled FSI simulations.

The maximum von Mises stresses in each of the analysis models are located at the connection of the horizontal box beam and the vertical pillar. The maximum stress distributions in the coupled FSI simulations are presented in Figure 36. The results of the quasi-dynamic model are shown in Figure 35. The maximum von Mises stress in Model II is approximately 12 MPa and it is located at the inner corner of the pillar-box beam connection. In Models III

and IV the maximum is located at the outer corner of the same connection. The maximum value in one-way coupled simulation is approximately 78 MPa. In the two-way coupled simulation the maximum von Mises stress reaches a value of approximately 220 MPa. The portal frame experiences the maximum stresses at the time instance of the simulated maximum cylinder CF displacement. Due to the opening in the pillar surface within the connection, the accuracy of the beam model near the maximum stress location at the pillar and box beam connection is not sufficient for local stress evaluation. Thus, Figure 35 is not directly comparable with the FSI results.

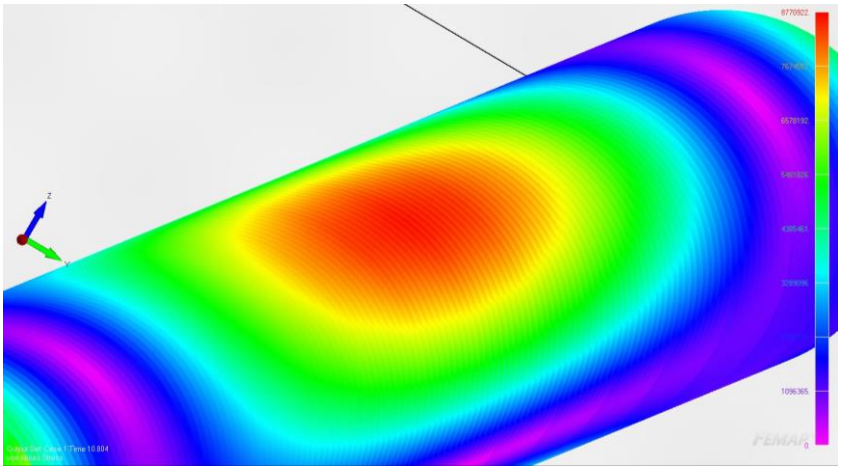

Figure 37. The maximum von Mises stress at the top of the cylinder midspan section in the quasi-dynamic beam model. Stress values shown at discrete cross-sections in Pa.

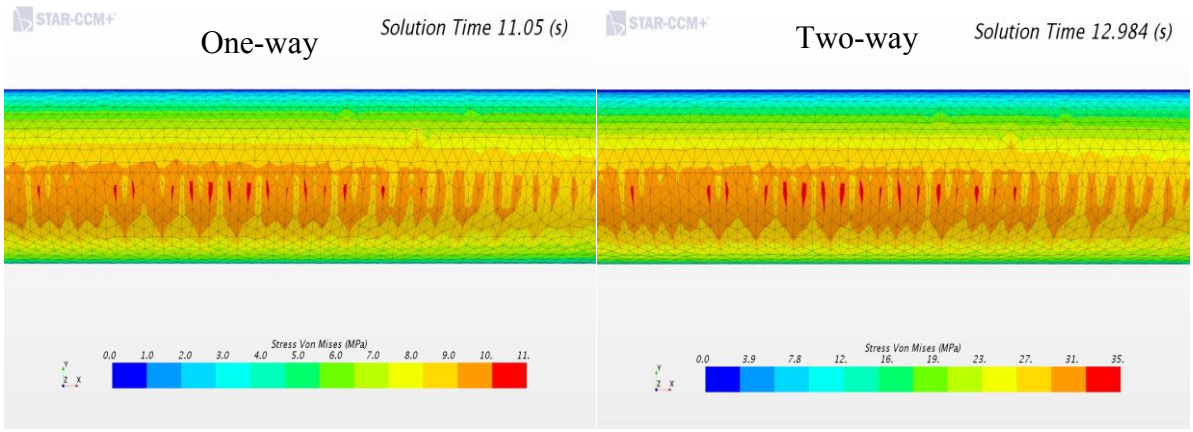

Figure 38. Maximum von Mises stress at the top surface of the cylinder midspan region.

The von Mises stresses in the top surface of the cylinder midspan region are shown in Figure 37 for Model II and in Figure 38 for Models III and IV. The overall stress distribution around the area is similar when comparing the beam and solid element models. The maximum values are localized at the cylinder top and bottom surfaces, as expected based on simple beam theory. The maximum values differ in magnitude. Model II indicates a maximum von Mises stress of 9 MPa. In Model III there is a highly localized maximum of up to 11 MPa. Similarly in Model IV the same elements experience the maximum stresses of 35 MPa. The surrounding element stress values are around 10 MPa and 31 MPa in Models III and IV, respectively. The maximum stresses in the cylinder section occur again at the instance of the maximum cylinder CF displacement.

6 Discussion

The numerical vortex shedding simulated in the portal frame wake exhibits similar vortex geometry as presented in multiple scientific publications, e.g., [1, 3, 16, 17] when observed on single cross-sections. Additionally, the numerical vortex shedding frequency in the cylinder wake estimated based on the lift force frequency response matches the analytical estimate with a difference of 5.1 %. The numerical vortex shedding occurs at the frequency of 14.5 Hz whereas the analytical model estimates a frequency of 13.8 Hz. Considering the uncertainty related to the Strouhal number estimation and the differing geometry from a single cylinder, the difference is within acceptable limits. Thus, the simulated wake field may be considered to represent the physical phenomenon at a level sufficient for the present scope.

Review of the vortex-induced dynamic wind loading in Table 8 reveals that the lift force response differs considerably between one- and two-way coupled simulations. The rms value of the force amplitude increases by 58 % when two-way coupling is used. Similarly, the absolute maximum and minimum values increase by 92 % and 101 %, respectively. The higher amplitude range of Model IV is clearly visible when Figures 22 and 23 are compared. Additionally, the oscillating behavior of the two-way coupled lift force is considerably more pronounced. The difference in the frequency response is also evident, as visible in Figure 25. The lift force has a single peak response at 14.5 Hz when the one-way coupled approach is studied. This is considered the original numerical vortex shedding frequency. However, for two-way coupling the frequency response has a second and considerably higher peak at 13.8 Hz, which corresponds to the portal frame's 4^{th} structural eigenmode. Based on this, it is evident that in the two-way coupled simulation the structural vibration governs the lift force response. Therefore, the structural motion leads to lock-in of the vortex-shedding frequency from 14.5 Hz to 13.8 Hz and furthermore to the increased amplitude range and peak values. One-way coupling is clearly unable to capture the lock-in phenomenon since the dynamic effect of the structure is not transferred onto the fluid domain. This is a significant finding which clearly shows the difference between the two modelling approaches.

Based on Table 8, the percentage differences between the drag force responses of the two FSI models are not considerable. The rms amplitudes are virtually identical and the differences in the absolute peak values are less than 10 %. However, comparing the plotted drag force in Figure 24, the difference between the modelling approaches becomes apparent. The drag force simulated with Model III varies slowly around a steady average value. The drag force simulated with Model IV on the other hand grows in amplitude range without a clear convergence being reached by the end of the simulation time. The oscillating behavior is also more dominant. Considering the PSD plot in Figure 26, the difference to one-way coupling is dramatic. The wide-banded frequency response below 2.0 Hz is somewhat amplified from one-way coupling but the response may now be considered narrow-banded since the drag force has a single dominant peak at 13.8 Hz. This corresponds to the 4^{th} structural eigenmode. It is therefore evident that the fluid-structure interaction has a significant influence on the drag force which the one-way coupling is unable to capture.

As discussed above, the level of modelled fluid-structure interaction affects the aerodynamic force responses. For the dynamic wind loading on the portal frame structure, this coupling effect is significant and cannot be identified without considering the effects of structural

deformations on the fluid domain, i.e., two-way coupling. The dynamic vibrations of the portal frame amplify the force responses and the lock-in of the vortex shedding is clearly visible from the frequency responses of the force components. It should be noted that the lift force has a considerably higher energy input to the structural vibrations as may be observed from the magnitude scales of the PSD plots in Figures 25 and 26. The reasoning for this is discovered from Table 3 where the 4th eigenmode response is shown to have the most significant displacements at the cylinder section's CF direction. As this section starts vibrating at 13.8 Hz, the vortex-shedding in the cylinder wake locks-in at the same frequency. The interaction causes a resonant response which amplifies the displacement response of the portal frame. This further increases the force amplitudes due to the increase of the aerodynamic pressure on the portal frame surface. As the lift force acts in the CF direction, the response amplification is higher than for the IL drag force. The level of modelling clearly affects the dynamic wind loading experienced by the portal frame to an extent that cannot be neglected.

The non-dimensionalized displacement results, presented in Tables 9 and 10, clearly show that the quasi-static Model I significantly underestimates all displacement magnitudes. This confirms that the dynamic effects have a significant influence on the structural response and therefore the VIV case cannot be estimated with a simple maximum peak load quasi-static analysis. The results of the quasi-static analysis are therefore excluded from further discussion which only considers the transient models II, III and IV.

Similar trend as in the dynamic wind loading may be observed for the structural deformations, i.e., the coupling effect changes the response characteristics. The largest displacements in the portal frame are observed at the cylinder center point, as expected prior to the simulations. The cylinder CF displacement exhibits a sinusoidally oscillating behavior in each transient simulation as shown in Figure 27. The CF displacement of Model III shows an amplitude range that after some time begins to grow but converges to a steady range. In Model II the displacement amplitude starts increasing in a similar manner. However, steady amplitude range is not reached by the end of the simulation time. This is likely due to the higher stiffness of the beam model which reduces the amplitude range as well as increases the structure's natural frequencies (see Appendix 1). Thus, the onset of larger amplitude vibration is delayed. The cylinder CF results of the two-way coupled simulation do not exhibit a converging amplitude range response. Instead, the amplitude continues to increase exponentially until the end of the simulation time. This leads to an increase of 202 % in the maximum displacement amplitude going from Model III to Model IV.

Based on the PSD of the cylinder CF displacement in Figure 29, it is evident that the cylinder vibrates at the natural frequency of the portal frame's 4th eigenmode. The vibration mode has additionally been confirmed visually from post-processed deformation graphics. The difference in the vibration frequency between Model II and Models III and IV is due to the higher structural stiffness of the beam model. Therefore, the beam model's 4th natural frequency is 15.5 Hz as presented in the Appendix 1. The difference of 0.1 Hz between the modal analysis and the PSD response of Model II is likely due to the difference in analysis software used to calculate the results. The PSD spectra were calculated using STAR-CCM+ while NX Nastran was used for the modal analysis. Considering this, Models II and III behave similarly, though the energy content in the response of Model II is lower. This indicates that the force contributions neglected in the quasi-dynamic modelling contribute to the CF displacement. Some effect is also due to the higher stiffness of the beam model. The two-way coupled simulation predicts a significantly higher vibrational energy content for

the CF displacement compared to Models II and III. The PSD peak is approximately 12.4 times higher in the two-way coupled simulation than experienced in the one-way coupled simulation. Based on the PSD response spectrum in Figure 29 and the exponentially growing amplitude range response, the portal frame experiences resonant vibration when simulated with the two-way coupled FSI model. This effect is captured neither by the one-way coupled FSI nor the quasi-dynamic analysis.

The IL displacement of the cylinder section may be considered to have a steady range response when simulated with the quasi-dynamic model. The response predicted by Model III follows a similar trend as the CF displacement. As visible in Figure 28 the amplitude range begins to increase but converges to a steady range within the simulation time. However, the IL displacement simulated with Model IV exhibits an exponentially increasing amplitude range without convergence to a steady range. The peak amplitude is increased by 134 % comparing two-way to one-way coupling.

The twin-peaked frequency response of the IL displacement in Figure 30 is narrow-banded. For the FSI simulations, the two peaks are located at 6.8 Hz and 13.8 Hz which correspond to the structural eigenmodes two and four. In the quasi-dynamic analysis these peaks are located at 6.1 Hz and 15.4 Hz which are the eigenmodes one and four of the beam model. The mode shift of the lowest mode from number one to number two is explained by the vortex-shedding in the pillar wake. Evidently, the pillar CF direction has a considerable influence on the cylinder IL displacement. This is naturally not present in the quasi-dynamic analysis as the force contributions in the x-direction have been neglected. Going from Model III to IV the frequency response changes in a similar trend to the CF direction where the frequency peak at 13.8 Hz is considerably increased. This and the exponentially growing amplitude are due to the resonant vibration at the portal frame's 4^{th} natural frequency.

Looking at the pillar end point displacements, similar observations can be made as for the cylinder part. However, the CF displacement at the pillar end point is only relevant for Models III and IV as there are no forces modelled in the pillar cross-flow direction in the quasi-dynamic analysis. Both Models III and IV predict a growing amplitude response for the CF displacement as presented in Figure 31. Again, the magnitude of the Model IV response is considerably higher, having both absolute maximum and minimum values around double to Model III results. The frequency responses in Figure 33 are virtually identical to the cylinder IL responses in Figure 30.

The pillar IL displacements plotted in Figure 32 for Models II and III exhibit a constant amplitude range response. The response of the two-way coupled FSI simulation indicates a growing amplitude range and shift to a higher frequency, as visible from approximately 9.5 s forward. Exceptionally to the other displacement results, the amplitude range simulated with the quasi-dynamic model is higher than that computed with the other two transient models. Possible reasoning for this is that as the drag forces are assumed constant in the quasi-dynamic analysis there are no interacting drag force peaks acting on the portal frame's components which could lower the response. Based on Figure 34, the frequency shift experienced in Model IV is from the 1^{st} structural eigenfrequency at 5.9 Hz to the 4^{th} eigenfrequency at 13.8 Hz which consequently lowers the first peak value. This confirms the conclusion made above that the primary vibration mode of the portal frame is the structural eigenmode number four. It is likely that the frequency of the IL displacement would have a single major peak at 13.8 Hz if the Model IV simulation time would be continued sufficiently

longer. Due to the lower level of fluid-structure interaction captured in Models II and III, the main response peak remains at the 1st structural eigenfrequency.

The evaluation of the portal frame's dynamic response is completed by reviewing the combined stress state during the wind-induced vibration. The maximum von Mises stresses are located in the connection of the box beam and the pillar in each transient simulation. For Models III and IV, the maximum stress is very localized at the lower connection corner and specifically on the outer side of the frame. In Model II the maximum stress is located at the opposite side of the box beam, i.e., in the low inner corner. It should be noted that due to the limitations of the beam element model, the local connection is not modelled accurately with beam elements. Therefore, the maximum stress of approximately 12 MPa is not comparable with the stress values of Models III and IV. The maximum von Mises stress value changes considerably between the results of Model III and Model IV. The maximum von Mises stress in Model III is approximately 78 MPa whereas the maximum value in Model IV reaches a value of approximately 220 MPa. However, as visible in Figure 36, the overall stress distribution is similar in the connecting region when the stress magnitude is neglected. All models experience the maximum at the same time instance as the maximum CF displacement occurs in the cylinder center point. This is expected since the structural stresses are a function of the displacements, as discussed in Section 3.2.1.

The cylinder midspan section is more suitable for comparing the stress results between Models II, III and IV, as it is accurately modelled also with the beam elements. The stress distribution predicted by the quasi-dynamic model in Figure 37 is similar to that in the FSI simulation results. The maximum stress occurs at the instance of the maximum downward CF displacement in each case. Models II and III predict almost identical maximum von Mises stress values of approximately 9 MPa and 11 MPa, respectively. The maximum values in Model III are also highly localized on specific elements and the surrounding stress field has values around 10 MPa. In this respect, the structural responses of Models II and III are similar. As expected based on the significantly higher displacement magnitudes, the von Mises stress magnitudes in Model IV are considerably higher. The local maximum is approximately 35 MPa.

The stress results indicate that the modelling decision has considerable effect on the structural analysis, which is mostly based on the stress values rather than the displacements. Purely based on the one-way or the quasi-dynamic analysis the portal frame structure would, despite possibly very high displacement magnitudes, be accepted as the yield limit has not been exceeded. However, the two-way coupled structural response is significantly different and based on the results the acceptable stress limit has been exceeded. Evidently, simplified quasi-dynamic or one-way coupled FSI simulations would lead to false engineering decisions.

The reliability of the obtained results has been improved by the quantity of different numerical models. Each of the models represents a different level of simplification which allows to make a comprehensive comparison between the results. Additionally, the lack of model test or empirical results is compensated by the range of numerical simulations. In general, the numerical approaches applied in the FSI simulations can be considered the state of the art. The partitioned one-way coupled FSI approach used in Model III is the industry standard method for wind-induced vibration analysis. The partitioned FSI algorithm with strong two-way coupling in Model IV represents the current academic state of the art. This

method is believed to be the most accurate in numerically capturing the physical phenomena that is available within the practical resources.

The uncertainties within the CFD part are mostly related to the mesh configuration, as presented in the mesh dependency study. Although, the mesh was constructed following the best practices suggested in [22] and based on the author's past experience there are possible inaccuracies (vortex capturing, numerical dissipation and dispersion) related to the numerical flow field. These, however, do not significantly affect the conducted result comparison. The numerical flow was modelled with the same mesh and discretization in each of the models. Additionally, the forces in the quasi-static and quasi-dynamic analyses were taken from the one-way coupled simulation. Therefore, the utilized combination of models can objectively determine the differences between the approaches which has been the primary objective of this thesis.

The finite element models were created following the industry standard practices. In general, the accuracy of the FEA models can be considered sufficient. In the solid element FEA model two wedge element layers in the thickness direction of each member seems to be sufficient. The results did not exhibit signs of significant numerical stiffness. Although additional layers might completely remove the possibility of added numerical stiffness, this would also increase the model size considerably. Mesh refinements were not conducted in the connecting regions of the 3D FEA model. This would be required for fully realistic local stress analysis.

The maximum stress value reached in Model IV exceeds the yield strength for typical marine grade aluminum [50] and would cause plastic deformation in this region. Therefore, the limit of linear elastic FEA has been reached. However, stresses over the yield strength increase the load carrying capacity of ductile materials [48] and the maximum stress is extremely localized at the connection, occurring practically within one element. Therefore, the plastic deformation would be constrained in a localized area and would not compromise the structural integrity. The linear elastic model may thus be considered valid for the current scope.

7 Conclusions

The design of large deck amusement structures on modern cruise ships has become an increasingly significant engineering task. The complexity of both the structures and the operational environment may render conventional design methods obsolete. Therefore, the current state of the art utilizes numerical one-way coupled fluid-structure interaction analysis to study the dynamic structural response in wind. However, as computational resources are becoming more readily available, there is interest to study the more demanding two-way coupled FSI method.

This thesis aimed to study the differences between one-way coupled and two-way coupled FSI simulations in analyzing VIV of modern cruise ships' deck amusement structures subjected to wind loading. For this purpose a large deck amusement structure was idealized as an aluminum portal frame. To create a comprehensive numerical benchmark case, four different models were analyzed. These included a simple quasi-static model, a quasi-dynamic model which utilized simplified loads from the CFD calculations, a one-way coupled FSI model and a two-way coupled FSI model utilizing a strong coupling algorithm. Partitioned approach to FSI simulation was adopted as it is the industry standard and readily available in commercial use. Computational fluid dynamics were simulated applying RANS and FVM discretization. SST k-ω turbulence model was used. The structural response was modelled utilizing linear elastic FEA. The numerical methods were chosen based on a review of the state of the art scientific literature and the current industry standard. The choice was limited by the available computational resources which ruled out the use of LES or combined RANS-LES schemes. FSI simulations were conducted using commercial CFD software STAR-CCM+. Simplified quasi-static and quasi-dynamic models were modelled with beam elements and post-processed using the commercial FEA software Femap. The integrated solver NX Nastran was used to compute responses of the beam models.

The results of this thesis show that the dynamic wind loading changed considerably between the one- and two-way coupled FSI simulations. There was a significant increase in the lift force magnitude when comparing two-way to one-way coupled simulation. Additionally, the lift force frequency shifted to the portal frame's natural frequency in the two-way coupled simulation which corresponded to lock-in of the vortex shedding frequency. The drag force magnitudes did not change significantly. However, the dynamic behavior of the drag force was altered. Thus, the overall dynamic wind loading increased going from one- to two-way coupling. Consequently, the vibrational behavior of the portal frame structure changed considerably from steady amplitude range vibration of the quasi-dynamic and one-way coupled models to resonant vibration of the two-way coupled model. The resonant vibration occurred at the lock-in frequency. Ultimately, this led to significantly higher displacements and structural stresses beyond the yield point in the case of the two-way coupled FSI simulation.

This thesis indicates that the level of modelled fluid-structure interaction is critical in the context of wind-induced vibration of slender beam structures, typical for modern cruise ships' deck amusements and water parks. If the interaction of the structure and the surrounding fluid domain is strongly coupled, the response cannot be modelled with either one-way coupled FSI or simplified quasi-dynamic analysis. This must be evaluated prior to the start of the analysis as overly simplified methods may lead to the underestimation the structural response and consequently false engineering decisions.

Possible future development areas in the numerical modelling approaches applied in the current study include, e.g., using a smaller time step and the use of different finite element types. A time step of less than $1/100^{th}$ of the highest considered structural eigenmode's oscillation period would be sufficient to achieve full temporal accuracy [22, 47]. Such an approach would require more computational resources. Plate type finite elements would be the ideal element type to be used in conjunction with the FSI analysis. This would allow for considerable computational savings without sacrificing the accuracy of the structural model. Additionally, using plate elements significantly reduces the pre-processing workload both in the geometry modelling as well as in the meshing phase. Such an approach is readily available using the co-simulation capabilities of STAR-CCM+ as utilized in [27] but it was limited in the present study by the available software.

Future consideration of the topic could utilize the current case set up as a benchmark for determining the limit at which one-way coupling seizes to be sufficient for accurate analysis. This would provide valuable information for engineering decisions made on the level of FSI modelling. Additionally, as the onset of VIV is fast it may considerably contribute to the stress cycles experienced by typical deck amusement structures. Therefore, the significance of wind-induced vibration on the fatigue life of these structures could be addressed. To establish a fully validated benchmark of the current case study scenario, wind tunnel model tests should be conducted. Experimental results would complete the extensive numerical simulation results. This combination would provide sound reasoning for any conclusions made about the differences in the modelling techniques.

Bibliography

[1]. Blevins, R. D. Flow-Induced Vibration. 2nd ed. New York, USA: Van Nostrand Reinhold, 1990. ISBN 0-442-20651-8.

[2]. Holmes, J. D. Wind Loading of Structures. London, United Kingdom: Spon Press, 2001. ISBN 0-203-30164-1.

[3]. Guilmineau, E. & Queutey, P. Numerical Simulation of Vortex-Induced Vibration of a Circular Cylinder with Low Mass-Damping in a Turbulent Flow. Journal of Fluids and Structures. Vol. 19:4. 2004. pp. 449-466. DOI: 10.1016/j.jfluidstructs.2004.02.004. ISSN 0889-9746.

[4]. DNV GL. DNVGL-RP-C205. Recommended Practice – Environmental Conditions and Environmental Loads. 2017.

[5]. Naudascher, E. & Rockwell, D. Flow-Induced Vibrations: An Engineering Guide. Mineola, New York, USA: Dover Publications, 2005. ISBN 0-486-44282-9.

[6]. Matin Nikoo, H., Bi, K. & Hao, H. Effectiveness of using Pipe-in-Pipe (PIP) Concept to Reduce Vortex-Induced Vibrations (VIV): Three-Dimensional Two-Way FSI Analysis. Ocean Engineering. Vol. 148. 2018. pp. 263-276. DOI: 10.1016/j.oceaneng.2017.11.040. ISSN 0029-8018.

[7]. Ferziger, J. H. & Perić, M. Computational Methods for Fluid Dynamics. 3rd rev. ed. Berlin, Germany: Springer, 2002. ISBN 3-540-42074-6.

[8]. Lienhard, J. H. Synopsis of Lift, Drag and Vortex Frequency Data for Rigid Circular Cylinders. Washington State University, College of Engineering, Research Division Bulletin. Vol. 300. 1966.

[9]. Sarpkaya, T. A Critical Review of the Intrinsic Nature of Vortex-Induced Vibrations. Journal of Fluids and Structures. Vol. 19:4. 2004. pp. 389-447. DOI: 10.1016/j.jfluidstructs.2004.02.005. ISSN 0889-9746.

[10]. Thorsen, M. J., Sævik, S. & Larsen, C. M. Time Domain Simulation of Vortex-Induced Vibrations in Stationary and Oscillating Flows. Journal of Fluids and Structures. Vol. 61. 2016. pp. 1-19. DOI: 10.1016/j.jfluidstructs.2015.11.006. ISSN 0889-9746.

[11]. Thorsen, M. J., Sævik, S. & Larsen, C. M. Fatigue Damage from Time Domain Simulation of Combined in-Line and Cross-Flow Vortex-Induced Vibrations. Marine Structures. Vol. 41. 2015. pp. 200-222. DOI: 10.1016/j.marstruc.2015.02.005. ISSN 0951-8339.

[12]. Ulveseter, J. V., Thorsen, M. J., Sævik, S. & Larsen, C. M. Time Domain Simulation of Riser VIV in Current and Irregular Waves. Marine Structures. Vol. 60. 2018. pp. 241-260. DOI: 10.1016/j.marstruc.2018.04.001. ISSN 0951-8339.

[13]. Griffith, D. T., Ho, C. K., Hunter, P. S., Sment, J., Moya, A. C. & Menicucci, A. R. Modal analysis of a heliostat for concentrating solar power. In: Allemang, R., De Clerck, J., Niezrecki, C. & Blough, J. R. (eds.) Topics in Modal Analysis I, Volume 5. Conference Proceedings of the Society for Experimental Mechanics Series. New York, USA: Springer, 2012. pp. 415-423. DOI: 10.1007/978-1-4614-2425-3_39.

[14]. Khan, N. B., Khan, M. I., Ibrahim, Z., Hayat, T. & Javed, M. F. VIV Study of an Elastically Mounted Cylinder having Low Mass-Damping Ratio using RANS Model. International Journal of Heat and Mass Transfer. Vol. 121. 2018. pp. 309-314. DOI: 10.1016/j.ijheatmasstransfer.2017.12.109. ISSN 0017-9310.

[15]. Li, W., Li, J. & Liu, S. Numerical simulation of vortex-induced vibration of a circular cylinder at low mass and damping with different turbulent models. In: OCEANS 2014 - TAIPEI. Taipei, Taiwan: IEEE, 2014. pp. 1-7. DOI: 10.1109/OCEANS-TAIPEI.2014.6964346.

[16]. Wang, H., Zhai, Q. & Chen, K. Vortex-Induced Vibrations of an Elliptic Cylinder with both Transverse and Rotational Degrees of Freedom. Journal of Fluids and Structures. Vol. 84. 2019. pp. 36-55. DOI: 10.1016/j.jfluidstructs.2018.10.004.

[17]. Wang, E. & Xiao, Q. Numerical Simulation of Vortex-Induced Vibration of a Vertical Riser in Uniform and Linearly Sheared Currents. Ocean Engineering. Vol. 121. 2016. pp. 492-515. DOI: 10.1016/j.oceaneng.2016.06.002. ISSN 0029-8018.

[18]. Zhao, M., Cheng, L., An, H. & Lu, L. Three-Dimensional Numerical Simulation of Vortex-Induced Vibration of an Elastically Mounted Rigid Circular Cylinder in Steady Current. Journal of Fluids and Structures. Vol. 50. 2014. pp. 292-311. DOI: 10.1016/j.jfluidstructs.2014.05.016. ISSN 0889-9746.

[19]. Xu, Y., Øiseth, O. & Moan, T. Time Domain Simulations of Wind- and Wave-Induced Load Effects on a Three-Span Suspension Bridge with Two Floating Pylons. Marine Structures. Vol. 58. 2018. pp. 434-452. DOI: 10.1016/j.marstruc.2017.11.012. ISSN 0951-8339.

[20]. Benra, F. -., Dohmen, H. J., Pei, J., Schuster, S. & Wan, B. A Comparison of One-Way and Two-Way Coupling Methods for Numerical Analysis of Fluid-Structure Interactions. Journal of Applied Mathematics. Vol. 2011. 2011. DOI: 10.1155/2011/853560.

[21]. Ryzhakov, P. B., Rossi, R., Idelsohn, S. R. & Oñate, E. A Monolithic Lagrangian Approach for Fluid-Structure Interaction Problems. Computational Mechanics. Vol. 46:6. 2010. pp. 883-899. DOI: 10.1007/s00466-010-0522-0.

[22]. Siemens PLM Software. Simcenter STAR-CCM+ Documentation. V. 2019.1. 2019.

[23]. Pei, J., Dohmen, H. J., Yuan, S. Q. & Benra, F. -. Investigation of Unsteady Flow-Induced Impeller Oscillations of a Single-Blade Pump Under Off-Design Conditions. Journal of Fluids and Structures. Vol. 35. 2012. pp. 89-104. ISSN 0889-9746.

[24]. Matusiak, J. Laivan Kelluvuus Ja Vakavuus. 4th Revised ed. Espoo, Finland: Otatieto, 2000. ISBN 951-672-293-8.

[25]. Mitra, S., Wang, C. Z., Hai, L. V., Reddy, J. N. & Khoo, B. C. A 3D Fully Coupled Analysis of Nonlinear Sloshing and Ship Motion. Ocean Engineering. Vol. 39. 2012. pp. 1-13. DOI: 10.1016/j.oceaneng.2011.09.015.

[26]. Hirdaris, S. E., White, N. J., Angoshtari, N., Johnson, M. C., Lee, Y. & Bakkers, N. Wave Loads and Flexible Fluid-Structure Interactions: Current Developments and Future Directions. Ships and Offshore Structures. Vol. 5:4. 2010. pp. 307-325. DOI: 10.1080/17445301003626263.

[27]. Lakshmynarayanana, P. A. & Temarel, P. Application of CFD and FEA Coupling to Predict Dynamic Behaviour of a Flexible Barge in Regular Head Waves. Marine Structures. Vol. 65. 2019. pp. 308-325. DOI: 10.1016/j.marstruc.2019.02.006. ISSN 0951-8339.

[28]. Lee, A. H., Campbell, R. L., Craven, B. A. & Hambric, S. A. Fluid-Structure Interaction Simulation of Vortex-Induced Vibration of a Flexible Hydrofoil. Journal of Vibration and Acoustics, Transactions of the ASME. Vol. 139:4. 2017. DOI: 10.1115/1.4036453.

[29]. Qian-bei, Y., Liu, G. R., Ju-bao, L., Liu, G. Z., Min, L. & Ri-zhi, D. Analyses of Fluid-Solid Coupling Dynamics of Elastic Tubes Vibrating in Cross Flows. European Journal of Mechanics - A/Solids. Vol. 73. 2019. pp. 248-259. DOI: 10.1016/j.euromechsol.2018.09.004. ISSN 0997-7538.

[30]. Zikanov, O. Essential Computational Fluid Dynamics. Hoboken, New Jersey, USA: John Wiley & Sons, 2010. ISBN 978-0-470-42329-5.

[31]. Sun, D., Owen, J. S. & Wright, N. G. Application of the k-ω Turbulence Model for a Wind-Induced Vibration Study of 2D Bluff Bodies. Journal of Wind Engineering and Industrial Aerodynamics. Vol. 97:2. 2009. pp. 77-87. DOI: 10.1016/j.jweia.2008.08.002.

[32]. Larsson, L., Raven, H. C. & Paulling, J. R. Ship Resistance and Flow. Jersey City, N.J.: Society of Naval Architects and Marine Engineers, 2010. ISBN 978-1-61344-138-1.

[33]. Menter, F. R. Two-Equation Eddy-Viscosity Turbulence Models for Engineering Applications. AIAA Journal. Vol. 32:8. 1994. pp. 1598-1605. DOI: 10.2514/3.12149.

[34]. Wilcox, D. C. Turbulence Modeling for CFD. 3rd ed. La Cañada, California, USA: DCW Industries, 2006. ISBN 978-1-928729-08-2.

[35]. Argyropoulos, C. D. & Markatos, N. C. Recent Advances on the Numerical Modelling of Turbulent Flows. Applied Mathematical Modelling. Vol. 39:2. 2015. pp. 693-732. DOI: 10.1016/j.apm.2014.07.001. ISSN 0307-904X.

[36]. Li, Y., Paik, K., Xing, T. & Carrica, P. M. Dynamic Overset CFD Simulations of Wind Turbine Aerodynamics. Renewable Energy. Vol. 37:1. 2012. pp. 285-298. DOI: 10.1016/j.renene.2011.06.029. ISSN 0960-1481.

[37]. Saydam, A. Z. & Taylan, M. Evaluation of Wind Loads on Ships by CFD Analysis. Ocean Engineering. Vol. 158. 2018. pp. 54-63. DOI: 10.1016/j.oceaneng.2018.03.071. ISSN 0029-8018.

[38]. Szabo, B. & Babuska, I. Introduction to Finite Element Analysis: Formulation, Verification and Validation. West Sussex, United Kingdom: John Wiley & Sons, 2011. ISBN 978-0-470-97728-6.

[39]. Petyt, M. Introduction to Finite Element Vibration Analysis. 2nd ed. Cambridge, New York, USA: Cambridge University Press, 2010. ISBN 9780511914751.

[40]. Zienkiewicz, O. C. & Taylor, R. L. The Finite Element Method : Its Basis and Fundamentals. 6th ed. Oxford, Burlington, Massachusetts, USA: Elsevier Butterworth-Heinemann, 2005. ISBN 9780080531670.

[41]. Zienkiewicz, O. C., Taylor, R. L. & Fox, D. D. The Finite Element Method for Solid & Structural Mechanics. 7th ed. Amsterdam, The Netherlands: Elsevier/Butterworth-Heinemann, 2014. ISBN 9780080951362.

[42]. Zienkiewicz, O. C., Taylor, R. L., Zhu, J. Z. & Taylor, R. L. The Finite Element Method: Its Basis and Fundamentals. 7th ed. Amsterdam, The Netherlands: Elsevier Butterworth-Heinemann, 2013. ISBN 978-1-85617-633-0.

[43]. Siemens. NX Nastran Basic Dynamic Analysis User's Guide. 2016.

[44]. MUltifrontal Massively Parallel Solver. (MUMPS 5.1.2) Users' Guide. 2017.

[45]. DNV GL. DNVGL-CG-0127. Class Guideline – Finite Element Analysis. 2016.

[46]. DNV GL. Rules for Classification - Ships, Part 6 Additional Class Notation, Chapter 1 Structural Strength and Integrity. 2018.

[47]. Richter, T. & Wick, T. On Time Discretizations of Fluid-Structure Interactions. In: Carraro, T., Geiger, M., Körkel, S. & Rannacher, R. (eds.) Multiple Shooting and Time Domain Decomposition Methods. Cham, Switzerland: Springer International Publishing, 2015. pp. 377-400. ISSN 9783-319233215. DOI: 10.1007/978-3-319-23321-5_15.

[48]. Young, W. C. & Budynas, R. G. Roark's Formulas for Stress and Strain. 7th ed. New York, USA: McGraw-Hill, 2002. ISBN 0-07-072542-X.

[49]. Dubief, Y. & Delcayre, F. On Coherent-Vortex Identification in Turbulence. Journal of Turbulence. Vol. 1. 2000. pp. N11. DOI: 10.1088/1468-5248/1/1/011.

[50]. DNV GL. Rules for Classification - Ships, Part 2 Materials and Welding, Chapter 2 Metallic Materials. 2018.

Appendices

Appendix 1. Results of the beam model's modal analysis. 1 page.

Appendix 1. Results of the beam model's modal analysis

The results of the beam model's dry modal analysis are presented in Table A1. All the observed eigenmodes are antisymmetric.

Table A1.

Mode no.	Natural frequency [Hz]	Reduced velocity	Mode shape
1	6.1	9.90	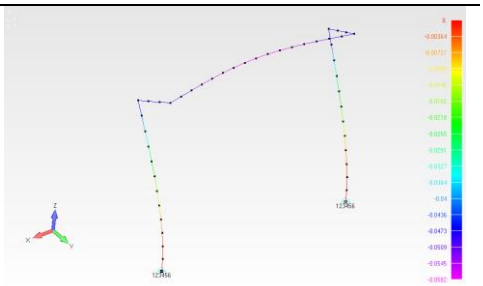
2	7.0	8.57	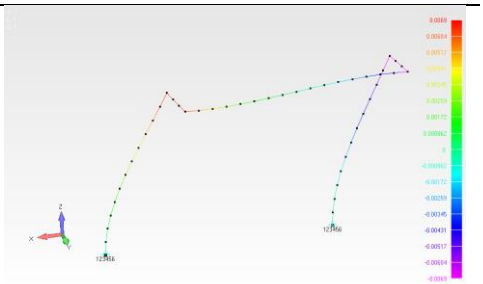
3	8.9	6.71	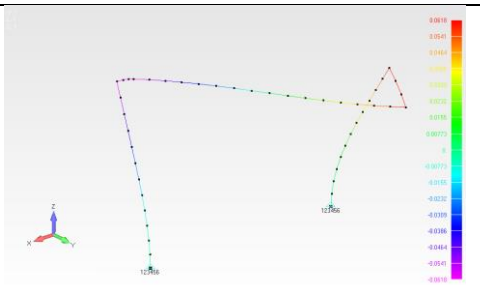
4	15.5	3.87	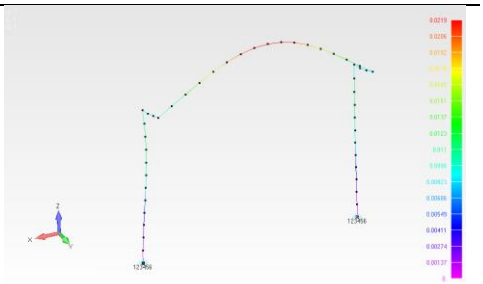
5	18.2	3.30